Adjoint-state method for seismic AVO inversion and time-lapse monitoring

by

Nisar Ahmed

Thesis submitted in fulfillment of
the requirements for degree of
PHILOSOPHIAE DOCTOR
(PhD)

Faculty of Science and Technology
Department of Energy Resources
2023

University of Stavanger
N-4036 Stavanger
NORWAY
www.uis.no

ISBN: 978-82-8439-181-6
ISSN: 1890-1387
PhD thesis UiS No. 714

"For consistent innovation and creativity, the mind and heart need to be in harmony"

Khalid Amin Khan

Acknowledgements

It is a pleasure to acknowledge many people who made this dissertation possible.

First and foremost, I sincerely thank my supervisor, Wiktor Waldemar Weibull, for allowing me to be a part of this project. Without his support and guidance, it was impossible to finish this project in time. His patience and wisdom have given me the freedom to accomplish this work in my own way. I deeply acknowledge and thank my co-supervisor Tuhin Bhakta for his advice and invaluable guidance throughout my time at the University of Stavanger. I also like to thank him for providing me with 2D simulated data of the CO_2 injection field and being available for discussion whenever I requested him.

I feel privileged to have worked and collaborated with Dario Grana and grateful to him for his contribution to various aspects of my research, his guidance through numerous meetings and chats, and his patience in thoroughly reviewing my manuscripts every time. I am also deeply indebted to him for reviewing my Ph.D. dissertation and for his valuable suggestions to improve its quality. I would also like to thank Tapan Mukerji, Beatriz Quintal, Gary Mavko, Patrick Connolly, and Raoof Gholami for providing excellent support and having chats and good discussions on various aspects of my work including seismic attenuation mechanisms, inversion workflow, and subsurface effective pressure measurements. I am indebted to Arild Buland for allowing me to take his course 'Seismic Amplitude Analysis and Inversion' from wherein I learned the essential concepts of the seismic inverse theory. I am also thankful to Irfan Ehsan for providing me with support to check the similarity index of my research papers and dissertation every time. Many thanks to all reviewers of my published research papers for their valuable time and comments. I sincerely applaud you.

I am also grateful to the Department of Energy Resources (IER) administration for providing me with an excellent working environment and support during my stay at UiS. I want to thank the numerous officemates and Ph.D./post-doc fellows at UiS for getting to know and working with them, and for having valuable discussions. I'm extremely grateful to Ph.D. fellow Maria Azam for always having a nice research chat regarding partial differential equations and other mathematical concepts. I would also like to thank all my friends in Stavanger, who were with me during the last three years and supported me in my ups and downs.

I express my special thanks to the National IOR Centre of Norway led by the University of Stavanger for the financial support of my Ph.D. project. I would also like to acknowledge Lundin Energy Norway and their partners Wintershall Dea and OMW in the Edvard Grieg license for providing the seismic data and well logs for this project. I also like to acknowledge the Digimon project which is an ACT2 project (no 299622) supported by the ACT international initiative for 2D synthetic data of CO_2 monitoring. The computations and simulations were carried out with resources given by UNINETT Sigma2 - the National Infrastructure for High-Performance Computing and

Data Storage in Norway. I must also give credit to Cleve Moler for inventing MATLAB.

Finally, I'm beyond grateful to all my family members; my parents and siblings, my wife and our kids, Musa, Hania, and Muhammad for their valuable support, encouragement, motivation, and prayers, and most of all for being another and more important dimension to life than geophysics.

Stavanger, February 2022

Nisar Ahmed

Abstract

This dissertation presents seismic amplitude versus offset (AVO) inversion methods to estimate water saturation and effective pressure quantitatively in elastic and viscoelastic media. Quantitative knowledge of the saturation and pore pressure properties from pre- or post-production seismic measurements for reservoir static or dynamic modeling has been an area of interest for the geophysical community for decades. However, the focus on the existing inversion methodologies and explicit expressions to estimate saturation-pressure variables or changes in these properties due to production or fluid injection has been based on elastic AVO models. These conventional methods do not consider the seismic wave attenuation effects on the reflection amplitudes and therefore can result in biased prediction.

Numerous theoretical rock physics models and laboratory experiments have demonstrated the sensitivity of various petrophysical and seismic properties of partially fluid-filled porous media to seismic attenuation. This makes seismic wave attenuation a valuable time-lapse attribute to reliably measure the saturation (S_w) and effective pressure (P_e) properties. Therefore, in this work, I have developed two AVO inversion processes i.e., the conventional AVO inversion method for elastic media and the frequency-dependent amplitude versus offset (FAVO) inversion technique for the viscoelastic media. This dissertation first presents the inversion strategies to invert the pre-stack seismic data for the seismic velocities and density by using the conventional AVO equation and for the seismic velocities, density, and Q-factors by using the frequency-dependent AVO method. These inversion methods are then extended to estimate the dynamic reservoir changes e.g., saturation and pressure variables, and can be applied to predict the saturation and pressure variables at any stage e.g., before and during production, or fluid injection, or to estimate the changes in saturation (ΔS_w) and pressure (ΔP_e). The first part of the dissertation describes the theory and formulation of the elastic AVO inversion method while in the second half, I have described the viscoelastic inversion workflow. FAVO technique accounts for the dependence of reflection amplitudes on incident angles as well as seismic frequencies and P and S waves attenuation in addition to seismic velocities and density. The fluid saturation and pressure in the elastic and inelastic mediums are linked to the reflection amplitude through seismic velocities, density, and quality factors (Q).

The inversion process is based on the gradient-descent method in which the least-square differentiable data misfit equation is minimized by using a non-linear limited-memory BFGS method. The gradients of the misfit function with respect to unknown model variables are derived by using the adjoint-state method and the multivariable chain rule of derivative. The adjoint-state method provides an efficient and accurate way to calculate the misfit gradients. Numerous rock physics models e.g., the Gassmann substitution equation with uniform and patchy fluid distribution patterns, modified MacBeth's relations of dry rock moduli with effective pressure, and constant Q models

for the P and S wave attenuation are applied to relate the saturation and effective pressure variables with elastic and an-elastic properties and then forward reflectivity operator. These inversion methods have been defined as constrained problems wherein the constraints are applied e.g., bound constraints, constraints in the Lagrangian solution, and Tikhonov regularization. These inversion methods are quite general and can be extended for other rock physics models through parameterizations.

The applications of the elastic AVO and the FAVO methods are tested on various 1D synthetic datasets simulated under different oil production (4D) scenarios. The inversion methods are further applied to a 2D realistic reservoir model extracted from the 3D Smeaheia Field, a potential storage site for the CO_2 injection. The inversion schemes successfully estimate not only the static saturation and effective pressure variables or changes in these properties due to oil production or CO_2 injection but also provide a very good prediction of seismic velocities, density, and seismic attenuation (quantified as the inverse quality factor). The partially CO_2-saturated reservoir exhibits higher P wave attenuation, therefore, the addition of time-lapse P wave attenuation due to viscous friction between CO_2-water patches helps to reduce the errors in the inverted CO_2/water saturation variables as compared to the elastic 4D AVO inversion.

This research work has a wide range of applications from the oil industry to carbon capture and storage (CCS) monitoring tools aiming to provide control and safety during the injection. The uncertainty in the inversion results is quantified as a function of the variability of the prior models obtained by using Monte Carlo simulation.

List of Publication

Paper 1

Ahmed, Nisar, Weibull, Wiktor Waldemar, Grana, Dario. 'Constrained non-linear AVO inversion based on the adjoint-state optimization.' In: *Computers & Geosciences*, **168:11**, pp.105214, (2022). https://doi.org/10.1016/j.cageo.2022.105214

Paper 2

Ahmed, Nisar, Weibull, Wiktor Waldemar, Grana, Dario, Bhakta, Tuhin 'Constrained non-linear AVO inversion for dynamic reservoir changes estimation from time-lapse seismic data.' In: *Geophysics*, **89:1**, pp. 1-65, (2024). https://doi.org/10.1190/geo2022-0750.1

Paper 3

Ahmed, Nisar, Weibull, Wiktor Waldemar, Quintal, Beatriz, Grana, Dario, Bhakta, Tuhin 'Frequency-dependent AVO inversion applied to physically-based models for seismic attenuation.' In: *Geophysical Journal International*, **233:1**, pp.234–252, (2023). https://doi.org/10.1093/gji/ggac461

Paper 4

Ahmed, Nisar, Weibull, Wiktor Waldemar, Bhakta, Tuhin, Grana, Dario, Mukerji, Tapan 'Time-lapse frequency-dependent AVO inversion method.' In: *Geophysics or other relevant journals*, **Paper to be submitted in 2023/24**.

Extended abstract

Ahmed, Nisar, Weibull, Wiktor Waldemar 'Gradient descent optimization method for AVO inversion in viscoelastic media.' In: *83rd EAGE Annual Conference & Exhibition*, volume **1**, pp. 1–5, (05 – 08 June 2022). https://doi.org/10.3997/2214-4609.202210467

Conference presentations

Ahmed, Nisar, Weibull, Wiktor Waldemar, Grana, Dario. 'Adjoint-state method based strategy for non-linear seismic AVO inversion.' In: *EGU - General Assembly*, **EGU22-209**, (23 – 27 May 2022). https://doi.org/10.5194/egusphere-egu22-209

Ahmed, Nisar, Weibull, Wiktor Waldemar, Grana, Dario, Bhakta, Tuhin 'Constrained non-linear 4D AVO inversion method for saturation-pressure changes estimation.' In: *6th International Workshop on Rock Physics*, **6IWRP: A Coruña, 2022**, (13 – 17 June 2022). pp.131, http://hdl.handle.net/2183/30566

Ahmed, Nisar, Weibull, Wiktor Waldemar, Bhakta, Tuhin, Grana, Dario, Mukerji, Tapan 'Time-lapse seismic AVO inversion method by using Gradient descent optimization.' In: *21st Annual Conference of the International Association for Mathematical Geosciences*, **IAMG2022: Nancy, 2022**, (August 29 – September 03, 2022). pp.88, https://www.iamgconferences. org/iamg2022/ShortAbstractsIAMG2022.pdf

Contents

List of Figures

List of Tables

Chapter 1

Introduction

"Interest invokes the continuum to proceed"

KAK

1.1 Introduction

Numerous techniques have been used in geosciences for investigating subsurface properties and among them, the seismic techniques are classified as the most successful and widely used methods. After the first successful deployment of the seismic method to locate the Orchard salt dome in 1924 Musgrave (1967), seismic theory and data have been an integral part of hydrocarbon exploration and field development. For many decades, seismic methods were used to designate and map the subsurface structures to identify potential hydrocarbon traps. However, gradually with the improvement in seismic data quality and computation technology, it becomes possible to use the variations of seismic amplitude with incident angles/offset (AVO) as a Direct Hydrocarbon Indicator (DHI) and to use it to differentiate the hydrocarbon-filled sediments from the background geology or brine-filled rock (Castagna et al. 1998; Hilterman 1990; Ostrander 1984). Over the last two decades, the time-lapse (4D) pre-stack seismic data turned out to be a useful tool in investigating reservoir complexities, the effect of fluid saturation and pressure variations separately, etc. (Bhakta and Landrø 2014; Côrte et al. 2023; Landrø 2001; Lang and Grana 2019; Trani et al. 2011).

In the conventional AVO methods, the reflection amplitudes at the geological boundary of two elastic layers depend only on the incident angles, elastic wave velocities, and density (Buland and Omre 2003b; Luo et al. 2020b; Tang et al. 2021). On the other hand, at the interface of a viscoelastic medium, the reflection amplitude is related to seismic attenuation (quantified as the inverse quality factor) of the layers and seismic frequency in addition to the elastic parameters and incident angles (Chen et al. 2018; Innanen 2011; Li and Liu 2019). Numerous attempts (Bhakta and Landrø 2014; Bhakta et al. 2022; Côrte et al. 2023; Dupuy et al. 2021a; Dupuy et al. 2021b; Forberg et al. 2021; Grana et al. 2022; Grana and Mukerji 2015; Landrø 2001; Lang and Grana 2019; Meadows 2001; Trani et al. 2011; Veire et al. 2006) have been made to estimate the static or dynamic fluid saturation and pressure properties from the pre-stack seismic data in the elastic medium. These methods do not incorporate the effect of time-lapse seismic attenuation. Recently some research (for example, Blanchard and Delommot 2015; Dinh and Van der Baan 2019; Morgan et al. 2012; Qi et al. 2016) has been made to estimate fluid saturation changes in the viscoelastic media from the time-lapse seismic data by applying viscoelastic AVO theory. However, their work has various limitations e.g., ignoring shear wave attenuation due to rock-frame heterogeneities and not taking into consideration the effect of attenuation due to changes in pore pressure. This encourages us to investigate the viscoelastic AVO theory more precisely and for understanding reservoir dynamic changes.

This dissertation is a theoretical and applied contribution towards a better estimation of saturation and pore pressure changes estimation by applying elastic and viscoelastic (frequency-dependent) amplitude-versus-offset inversion methods and incorporating viscous friction between the viscous fluids and between the fluids and solid grain walls. In addition to the estimation of the reservoir dynamic parameters (e.g., saturation and pressure) by using seismic inverse modeling, this dissertation also contributes to predicting the seismic wave velocities and quality factors, and bulk density. This first chapter gives a summary and brief introduction to the dissertation. I begin with the seismic time-lapse analysis, the theoretical background of the subject, a brief literature

review, and a conceptual description of seismic attenuation mechanisms. In the end, the organization of the dissertation and summary of individual papers is briefly described.

1.2 Seismic time-lapse analysis

At this moment, it is worthwhile to describe the fundamental physical mechanisms that are relatively associated with hydrocarbon production or fluid injection or environmental changes caused by variations in the reservoir rock properties or in its pressure conditions. Primarily and the most noticeable effect is the effect caused due to fluid replacement in the porous and permeable sediments i.e. when water replaces the pore spaces of produced oil, the pore pressure drops, and as a result, dissolved gas appears in the solution below the bubble point (Johnston 2013). Fluid replacement within the reservoir changes the elastic moduli and bulk density of the saturated rock and consequently may alter the P wave propagation velocities substantially in reservoir sediments undergoing hydrocarbon production or fluid injection. However, fluid substitution has a notably lower effect on the S wave propagation velocity. Variations in the seismic velocities and density contrast at the reservoir and seal rock interface change the reflection coefficient series and resultantly translate into interpretable seismic AVO signatures (Du et al. 2019; Wandler et al. 2007). Similarly, fluid migration within the reservoir results in seismic velocity variations which proceed with noticeable time-shifts of recorded seismic events. If the elastic parameters e.g., matrix and rock skeleton moduli, fluids moduli, and petrophysical properties like porosity, pre- and post-production saturation levels, etc. are known, the effect of change in saturation and pressure on seismic velocities can be modeled by using Gassmann's equation (Gassmann 1951; Mavko et al. 2020) and MacBeth's modified relationships between dry-rock moduli and effective pressure (Grana 2016; MacBeth 2004). Bulk density and P wave velocity increase in case water replaces either oil or gas and then lowers because of gas/CO_2 substituting water or oil. Seismic P velocity variations due to fluid substitution are possibly meaningful and relative changes may reach hundreds of meters per second (Maharramov et al. 2016).

Hydrocarbon production or fluid injection into a reservoir can result in stress variations. Therefore, pressure changes (e.g., changes in effective pressure due to pore pressure variations) are another essential mechanism responsible for the time-lapse effects (Holt et al. 2005; Landrø 2001). In general, seismic velocities and density are higher within compacting reservoir sediments. For example, dropping pore pressure results in an increase in effective pressure and both acoustic and shear velocities will typically increase. Conversely, reservoir rock that is under fluid injection normally shows a decrease in seismic velocities due to an increase in pore pressure (Zoback 2010). However, almost every researcher (Bhakta and Landrø 2014; Forberg et al. 2021; Grana and Mukerji 2015; Landrø 2001; Lang and Grana 2019; Trani et al. 2011) has assumed pre- and post-production reservoir density independent of the pore pressure changes. In addition to the changing fluids saturation and pressure, there are numerous other time-lapse processes e.g., thermal and chemical processes, porosity variations in case of subsidence, etc. may result in changes in seismic velocities. However, the scope of this dissertation is to focus on the prediction of the effects of saturation and pressure changes from pre-stack seismic data.

In the published scientific literature, a variety of methods based on seismic AVO theory integrated with laboratory measurements and rock physics models (e.g., Gassmann uniform and patchy fluid distribution models, Hertz–Mindlin method, MacBeth's compliance model, etc. (Batzle and Wang 1992; Gassmann 1951; Grana 2016; Hill 1963; MacBeth 2004; Mavko et al. 2020; Mindlin 1949)) have been presented for reservoir dynamic changes estimation. These methods primarily vary in the models subject to relate the reservoir dynamic parameter domain to the seismic reflectivity domain, for example, some of the methods use a direct link between two domains, and the alternative use an intermediary elastic parameter domain between reservoir properties and seismic response. The methods use the direct links between two domains relying on first- or/and second-order empirical regression models to relate the rock and pore fluid physics. In the famous method proposed by Landrø (2001), explicit expressions for saturation-pressure changes are derived by directly linking the AVO intercept and gradient with reservoir dynamic changes and by assuming the linear and quadratic expansions between elastic properties and reservoir parameters. Developments and extensions in the applications of Landrø's approach have been made by including numerous non-linear relationships between time-lapse AVO and reservoir properties changes (Angelov et al. 2004; Bhakta 2018; Lang and Grana 2019; Meadows 2001). Similarly, analogous expressions of Landrø's method are also presented for the time-shift and seismic impedance attributes and higher (than 2) P to S wave velocities ratios (Bhakta and Landrø 2014; Grude et al. 2013; Kvam and Landrø 2005; Trani et al. 2011; Veire et al. 2006). Alvarez and MacBeth (2014) developed an approximation for more intuitive understanding which allows mapped time-shift and 4D seismic amplitude to be associated directly with the weighted linear sum of saturation and pore pressure variations. MacBeth et al. (2006) published a data-driven method similar to Landrø's linearized model wherein the model properties are calibrated by using production data instead of laboratory measurements.

An alternative methodology that uses the elastic property domain as an intermediary between the seismic response and reservoir static or dynamic properties has also been presented by several researchers. This procedure usually needs a well-founded and valid petro-elastic model (PEM) to compute the elastic variables and a synthetic seismic forward model. This workflow allows for using of theoretical rock physics models to calculate the seismic velocities and density from the basic petrophysical properties such as fluid saturation, porosity, pressure, mineralogy, etc. These techniques may include non-linear equations relying on theoretical physics in preference to data observations and measurements. The relation between seismic reflectivity and elastic parameters can be defined via any seismic forward modeling method or renowned wavelet convolution model. These methods comprise on two-step inversion process that first translates the seismic amplitudes to acoustic impedances and then further invert to the saturation-pressure changes (Correia et al. 2014; Dadashpour et al. 2008; Davolio et al. 2012; Davolio et al. 2013; Emerick 2014; Grana and Mukerji 2015; Meadows and Cole 2013; Ribeiro and MacBeth 2006).

Bayesian inversion processes are nowadays more commonly applied to solve geophysical inverse problems (Buland and Omre 2003b; Grana et al. 2021; Mosegaard and Tarantola 1995; Sen and Stoffa 1996). In the particular context of time-lapse seismic AVO inversion to reservoir dynamic changes estimation, a variety of inversion formulations in the Bayesian framework have been proposed (Emerick 2014; Floricich

et al. 2012; Grana and Mukerji 2015; Landa et al. 2015; Lang and Grana 2019; Wong et al. 2015). To address the problem of non-linearities because of gas saturation and pressure response, Côrte et al. (2023) applied a Markov Chain Monte Carlo method to evaluate the uncertainties in the inverted saturation-pressure variables and sample the Bayesian posterior distribution. The advantages of these statistically based inversion techniques are that the uncertainties can be assessed analytically. However, the computational cost and feasibility of applying for large geophysical datasets are usually not practical due to the spatial correlation of the model properties. Contrastingly, the adjoint-based non-linear optimization methods are computationally fast and provide an inverse solution with good convergence. Nevertheless, the implementation of the adjoint method for non-linear optimization with analytical solutions of the first-order gradient of the objective function for time-lapse seismic AVO inversion to estimate the saturation-pressure changes has not been yet proposed.

Similarly, when seismic energy propagates through the subsurface geological strata or partially fluid fill reservoir rock, both P and S seismic waves are dissipated due to several mechanisms (Blanchard 2011; Müller et al. 2010; Pride et al. 2004; Quintal et al. 2011). However, the effect of time-lapse seismic attenuation (Blanchard and Delommot 2015; Weinzierl and Wiese 2021) on seismic amplitude due to changes in fluid saturation (especially gas) and pressure has been ignored in the previously discussed work. Therefore, time-lapse attenuation, if taken into consideration as a monitoring tool for saturation-pressure changes estimation during hydrocarbon production or CO_2 geological storage can provide a more realistic way to find these dynamic variables (Dinh and Van der Baan 2019). This leads to extending the research domain for further investigation of reservoir dynamic changes measurement by including the viscoelastic properties of a medium. A comprehensive discussion on seismic attenuation theory has been included in the next section to understand seismic attenuation, its types, and the various mechanisms responsible for it.

1.3 Seismic attenuation theory

Seismic attenuation refers to the loss of coherent wave-front with distance when seismic energy propagates through the subsurface geological strata. The attenuation is quantified as the inverse quality factor. Numerous physical mechanisms that can result in seismic wave attenuation are generally split into two processes: extrinsic and intrinsic attenuation. Extrinsic attenuation is when the total seismic energy of the wavefield is conserved (e.g., geometric spreading and scattering), while intrinsic or inelastic attenuation occurs due to the conversion of elastic energy into heat, due to particle friction like solid-solid friction in the grain contacts or micro-cracks or viscous friction between the viscous fluid and the solid grain walls or crack walls). Intrinsic attenuation of body waves caused by viscous friction between the viscous fluid in the pore space and the solid grain walls is of great interest to exploration geophysics (Müller et al. 2010). The scientific presumption is that the knowledge of fluid-related attenuation in the oil and gas reservoirs combined with improved estimation of seismic wave attenuation from the surface seismic data may help to estimate hydraulic properties and reservoir characterization.

It is widely recognized that the existence of fluids within the rock pore space leads to

seismic attenuation and velocity dispersion by the predominant phenomenon referred to as wave-induced fluid flow (WIFF). Wave-induced fluid flow takes place as the seismic wave passage generates pressure gradients within the porous medium associated with internal friction. WIFF's description in partially saturated porous sediments considers three different length scales - macroscopic, mesoscopic, and microscopic (Toms et al. 2006) and are shown in Figure 1.1. Macroscopic or global flow occurs when the pressure gradient due to WIFF is over the wavelength of a seismic compressional wave and is quantified theoretically by Biot's theory (Biot 1956; Biot 1962; Bourbié et al. 1992; Pride 2005). Biot's theory explains the magnitude of observed attenuation for the global flow mechanisms above 100 kHz seismic frequencies. Alternatively, on the other end of the heterogeneity scale, due to pore shapes and orientation differences, different compliances of the adjoining pores may result in local spatial gradients between these pores. For example, granular rocks are commonly assumed to have quite compliant pores in the contact areas between adjoining pores and stiffer pores occurring in between these grains. The passage of a compressional wave in a rock deforms the grain contact area to a far larger extent compared with the intergranular pores, leading to local pressure gradients, relative fluid motion, and viscous attenuation. This phenomenon of pore-scale WIFF is also called local or squirt flow and is responsible for seismic wave attenuation at ultrasonic frequencies (Johnston et al. 1979; Pride et al. 2004; Winkler 1985).

Wave-induced fluid flow can also happen on a scale way smaller compared with the wavelength but significantly higher than normal pore size due to spatial variations in rock compliance. This scale of heterogeneities is known as mesoscopic flow (Figure 1.1). The passage of the P wave leads to compression of the porous framework on the time scales applied by the seismic wave speed. When a compression or a dilation of seismic energy passes through a rock that has saturation fluid and rock properties heterogeneities, it creates spatial gradients in the pore pressure. The heterogeneities present on the length scale larger than the pore scale but lower than the wavelength cause the development of gradients in the pore pressure on the mesoscale which leads to seismic energy dissipation in a broad range of frequencies. It is considered that mesoscopic flow is a substantial phenomenon of partial fluid-related attenuation in the seismic data frequency range of a few Hz to 1000 Hz (Pride et al. 2004; Tisato and Quintal 2013; Toms et al. 2006) and therefore is the focus to include in the current inversion method and this dissertation.

The level of heterogeneities in the reservoir rock, for example, the difference between the elastic properties of varying parts of rocks and fluid patches, etc. are the significant source of seismic wave attenuation. The two most noticeable frameworks that have gained considerable attention in past years are patchy fluid-saturated reservoirs and fractured rocks. In case of two non-mixing pore fluids with significantly varying moduli (for instance brine and gas) are present in the form of patches at the mesoscale results in substantial wave attenuation and velocity dispersion (Caspari et al. 2019; Murphy III 1982; Quintal et al. 2011; White et al. 1975). Wave-induced pore pressure equilibration can be attained only if the seismic wave has an adequately low frequency such that the characteristic diffusion length (the virtual boundary between uniform and patchy saturation regimes) is in large contrast to the largest spatial scale of fluid mixing. However, at higher frequencies, the pressure gradient between neighboring liquid and gas-saturated phases will not have enough time to re-equilibrate causing an increased

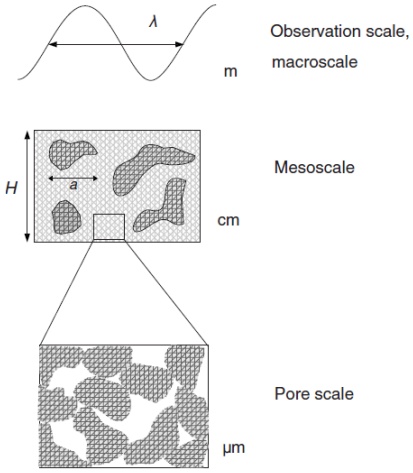

Figure 1.1: Different scales of heterogeneities and WIFF occur in seismic frequencies range which is known as the mesoscopic scale (from Müller et al. 2010).

seismic velocity and bulk modulus. This leads to the concept that the existence of two fluids (partially saturated rocks) in the pore spaces is the source of additional elastic wave attenuation-dispersion that is specifically associated with the relaxation fluid's pore pressure. In a partially saturated porous media, the dependence of frequency on attenuation-dispersion is controlled by various factors such as fluid distribution patterns, size and shape of fluid patches, pore connectivity and elastic moduli of the rock-forming minerals, and properties of fluid phases, etc. (Carcione and Picotti 2006; Mavko et al. 2020; Müller et al. 2010). Figure 1.2 shows the 2D model of the P wave attenuation due to wave-induced fluid flow (WIFF) in the baseline and monitor cases (left-side panel). The corresponding attenuation models are computed by using the constant Q rock physics model (Mavko et al. 2020) and are shown in the right-side panel. The magnitude of attenuation approaches zero when there is a single fluid present, therefore, in the baseline model which is fully water-saturated, the respective attenuation is zero or close to zero value. The attenuation has maximum values in the partial fluid saturated zones (water/CO_2), especially in the low CO_2 zones (e.g., $S_{CO_2} > 0.9$).

In this work, one of the goals is to translate these observed seismic wave attenuation changes due to WIFF at mesoscale into physical changes within the rock itself and then used to map ideally any changes in the pressure and saturation.

1.4 Aims and objectives of dissertation

This dissertation deals with the problem of seismic reservoir characterization and improved oil recovery. The primary focus is on the development of an appropriate theoretical background and workflow, including the frequency dependence on the time-lapse (4D) seismic AVO inversion and analysis to estimate viscoelastic properties, pressure, and fluid saturation changes. The objective is to include the time-lapse seismic

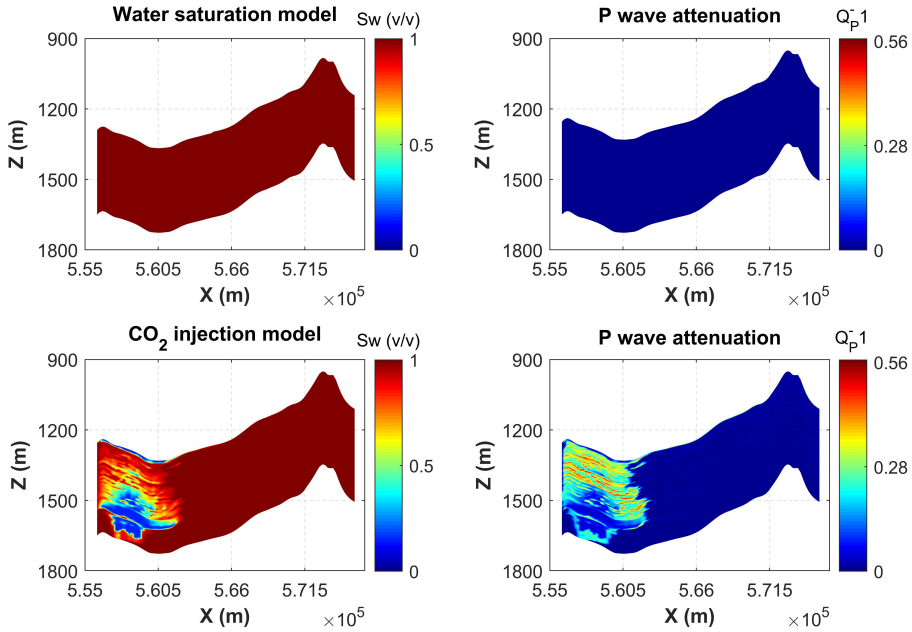

Figure 1.2: P wave attenuation model due to wave-induced fluid flow (WIFF) in the baseline and monitor cases. The baseline model represents the full water saturation case and the CO_2 has been injected in the monitor model.

attenuation measurements in the 4D AVO inversion workflow while mapping saturation-pressure variables or changes in these properties. In addition to the frequency-dependent method, the AVO inversion method is developed without considering the dependence of reflection amplitudes on seismic frequencies (elastic AVO) and to estimate the elastic properties and saturation-pressure variables. This project is comprised of several phases as described below:

- In the first step, a theoretical foundation has been developed for without frequency and frequency-dependent seismic AVO inversion (elastic AVO and FAVO) methods to estimate the seismic velocities, density, and seismic quality factors. This is because of the reservoir dynamic properties are linked with seismic reflectivity through elastic and an-elastic properties. Then, the extension of these inversions (elastic AVO and FAVO) schemes to map the fluid saturation and pore pressure changes in the elastic and viscoelastic mediums was carried out. The AVO inversion methods are applied to the different parameterizations of the model by using the chain rule of differentiation and by incorporating feasible and adequate rock-physics relations.

- The next phase includes performing of feasibility analysis with 1D synthetic data to predict the seismic properties of the elastic and viscoelastic medium. Then, apply the inversion methods to the synthetic data simulated under various time-

lapse scenarios to predict the oil/water saturation and pressure properties and the changes in saturation-pressure variables due to either production or fluid injection.

- Implementation of the 4D inversion methods to 4D seismic data and compare the results to those obtained using conventional AVO and FAVO analysis and inversion. For example, the 4D inversion methods are tested on the 2D model obtained after CO_2 injection in the Smeaheia field.

1.5 Organization of dissertation

The estimation of reservoir saturation level and effective pressure by using conventional and frequency-dependent AVO inversion methods is the primary focus of this dissertation. These reservoir properties are linked with seismic reflectivity through elastic and an-elastic properties in the elastic and viscoelastic media. Therefore, the main part of the dissertation consists of four independent research papers including their own abstracts or summaries, introductions, theory and methods (inversion workflows), applications to data, and appendixes. Two of the four papers are already published and two are under consideration in widely known scientific journals in geophysics. In addition, a short chapter summarizing the main conclusions is placed at the end. In the appendix, I have discussed the computation cost of the adjoint-state-based gradients and the convergence of the optimization method. The organization of the chapters and the relationship between these chapters are described as follows:

The paper in **Chapter 2**, Constrained non-linear AVO inversion based on the adjoint-state optimization, presents a non-linear seismic AVO inversion method to estimate the seismic velocities and bulk density from pre-stack seismic data. The inversion process is formulated by using the gradient descent optimization method wherein the first-order gradient of the objective function is implemented by using the adjoint-state method. The error function is minimized by making use of the second-order non-linear limited-memory BFGS algorithm. The applications of the method were tested on 1D and 2D synthetic datasets obtained from the Edvard Grieg Field, Norwegian North Sea, and simulated by using both convolutional modeling and finite difference methods. The concept behind the methodology of this paper is mainly contributed by the first two authors. The first author is the principal contributor in the writing of the initial draft, its layout, and visual presentations of results. My co-authors revised the text and contributed to technical discussions and suggestions. Wiktor Weibull also helped in the derivation of the adjoint-based gradients and codding. This paper is published in the November 2022 issue of Computers & Geosciences.

In the paper in **Chapter 3**, Constrained non-linear AVO inversion for reservoir dynamic changes estimation from time-lapse seismic data, we extend the inversion method described in Chapter 2 to estimate the static saturation and pressure properties or changes in these properties due to production or fluid injection from pre-stack seismic data. In this inversion workflow, the forward model comprises of linearized AVO equation and rock physics models e.g., Gassmann's equation (1951) and MacBeth's modified models (MacBeth, 2004; Grana, 2016) are used to relate the saturation and pressure variables with elastic properties and then seismic response. Furthermore, the chain rule of the derivative is used to derive the gradient of the objective function with

respect to water saturation and effective pressure. The bound constraints based on prior geological and reservoir engineering knowledge are applied to limit the solution space of model variables e.g., saturation can only vary between 0 – 1. The applications of the inversion scheme are first illustrated on 1D synthetic data simulated under various 4D scenarios and then applied to a 2D model representing the CO_2 injection field. The main idea of this inverse workflow is conceptualized with the collaboration of my co-authors. However, major contributions i.e., manuscript layout and writing, visual presentation of results, and implementation of code are made by the first author. My co-authors also contributed to text reviewing and editing, technical suggestions, and discussions, and by helping to solve the problems experienced during coding. This paper is currently under review in Geophysics and the results of this paper were also presented at the 6th International Workshop on Rock Physics, held in A Coruña, Spain.

In the paper in **Chapter 4**, Frequency-dependent AVO inversion applied to physically based models for seismic attenuation, we present a new inversion method to estimate the elastic and an-elastic properties in the viscoelastic media. The inversion strategy is based on a similar approach described in Chapter 2. However, in the forward model of this paper, the reflection amplitude is dependent on seismic frequencies and P and S wave quality factors in addition to incident angles, P and S wave velocities, and density. Therefore, the frequency-dependent AVO inversion method helps to estimate the seismic wave quality factors which potentially provides knowledge about rock and fluid properties. The inversion scheme is general and therefore we have applied it to retrieve the quality factors (also referred to as the inverse of seismic attenuation) based on various physically based attenuation models e.g., empirical relations (Waters and Waters 1981), constant Q model (Dvorkin and Mavko 2006; Mavko et al. 2020) and frequency-dependent White model (Quintal et al. 2009; White et al. 1975). The applications are illustrated on 1D and 2D synthetic datasets. Moreover, we also examine the crosstalk study between the inverted properties classes (e.g., V_P - Q_P, V_S - Q_S, $V_P - V_S$, $Q_P - Q_S$) arises due to coupling effects of simultaneous inversion of multi-parameters. The main contribution i.e., manuscript structure and writing, graphic presentation, and implementation of code is made by the first author. My co-authors also contributed to text reviewing and editing, technical suggestions, and discussions, and by helping to solve the problems experienced during coding. Some of the results of this paper were presented at the 83rd EAGE Annual Conference & Exhibition, held in Madrid, Spain. This paper is published in the April 2023 issue of Geophysical Journal International.

In the paper in **Chapter 5**, Time-lapse frequency-dependent AVO inversion method, we derive a novel frequency-dependent AVO inversion workflow to estimate water saturation and effective stress or changes in saturation-pressure variables either due to production or fluid injection. The proposed method is based on the minimization algorithm e.g., the gradient descent method which iteratively moves in the descent direction to find the minima of the least-squares error function. We use the analytical gradient solution derived in Chapter 4 e.g., the partial derivatives of the Lagrangian with respect to V_P, V_S, ρ, Q_P, and Q_S. Then, we implemented the chain rule of derivative and rock physics theory to obtain the analytical gradient solution of the error function with respect to saturation and pressure variables. Two rock physics models i.e., Gassmann-Hill patchy fluid saturation and constant Q models are used to relate the saturation and pressure variables with seismic elastic and an-elastic properties. The newly derived

method is applied to various 1D synthetic applications simulated under various 4D scenarios with and without noise levels. The first author conceptualized the idea and centrally contributed to writing, implementing the data, and coding. My co-author's participation includes reviewing and editing text and equations, technical discussion, recommendations regarding the formulation of the manuscript, and solving coding-related issues. Some parts of the results of this paper have been presented at the 21st annual conference of IAMG2022 in Nancy, France. This paper will be submitted to Geophysics or other relevant journals in the future.

Thereafter, in a short **Chapter 6**, I first outlined the most important results and outcomes of this dissertation. I then summarize the assumptions and limitations of the method with some possible future research directions.

In the end, in appendices, I illustrated the benefits i.e., computational cost and accuracy of the gradient computed by using the adjoint-state method (analytical derivation) over the finite difference approximation. I also included the convergence of the non-linear minimization method i.e., L-BFGS around the minimum point.

Chapter 2

Constrained non-linear AVO inversion based on the adjoint-state optimization

By:
Ahmed, Nisar[1]
Weibull, Wiktor Waldemar[1]
Grana, Dario[2]

[1]Department of Energy Resources, 4021 Stavanger, University of Stavanger, Norway
[2]Department of Geology and Geophysics, School of Energy Resources, University of Wyoming, Laramie, Wyoming 82071, United States

Printed in:
Computers & Geosciences, 168:11, pp 105214, (2022)
https://doi.org/10.1016/j.cageo.2022.105214.

2.1 Summary

Pre-stack AVO inversion of seismic data is a modeling tool for estimating subsurface elastic properties. Our focus is on the model-based inversion method where then unknown variables are estimated by minimizing the misfit to the observed data. Standard approaches for non-linear AVO inversion are based on gradient descent optimization algorithms that require the calculation of the gradient equations of the objective function. To improve the accuracy and efficiency of these methods, we developed a technique that uses an implementation of the adjoint-state-based gradient computation. The inversion algorithm relies on three basic modeling components consisting of a convolution-based forward model using a linearized approximation of the Zoeppritz equation, the definition of the objective function, and the adjoint-computed gradient. To achieve an accurate solution, we choose a second-order optimization algorithm known as the limited memory - BFGS (L-BFGS) that implicitly approximates the inverse Hessian matrix. This approach is more efficient than traditional optimization methods. The main novelty of the proposed approach is the derivation of the adjoint-state equations for the gradient of the objective function. The application of the proposed method is demonstrated using 1D and 2D synthetic datasets based on data from the Edvard Grieg oil field. The seismic data for these applications is generated by using both convolutional modeling and finite difference methods. The results of the proposed method are accurate and the computational approach is efficient. The results show that the algorithm reliably retrieves the elastic variables, P- and S-wave velocities, and density for both convolutional and finite difference models.

2.2 Introduction

In a seismic inversion, the objective is to reconstruct unknown model variables in the subsurface, for example, elastic velocities, from a set of seismic measurements, including seismic amplitudes and travel time measured at the surface (Aki and Richards 1980). The inversion results are retrieved from seismic reflection data by solving the non-unique and ill-posed inverse problem and they provide a quantitative model of predicted physical properties varying laterally and vertically (Buland and Omre 2003b). Seismic data inversion schemes can be split into two main classes, post-stack (or acoustic) impedance, and pre-stack (or elastic) inversions. Post-stack inversion aims to predict acoustic impedance from stacked seismic data and it is often used in stratigraphic interpretation (Ghosh 2000) but it does not give any information about the shear wave velocity (Maurya et al. 2018; Morozov and Ma 2009). On the other hand, pre-stack inversion is based on the concept of amplitude variations with offset/angle (AVO/A) and aims to predict a set of elastic attributes such as seismic velocities, impedances, and density (Downton 2005). AVO inversion results are typically correlated with petrophysical attributes like porosity, saturation of fluids, and reservoir litho-facies. These properties play a significant role in lithology prediction, geofluids identification, and quantitative reservoir characterization (Chiappa and Mazzotti 2009; Grana 2020; Luo et al. 2019; Zhao et al. 2014b). In addition, AVO inversion can also be used in time-lapse seismic monitoring studies to predict the changes in pressure, saturation,

and porosity, as an example, for CO_2 sequestration in depleted reservoirs (Dupuy et al. 2021b; Lang and Grana 2019).

A seismic reflection event at the recording point is described generally by the convolution of the seismic source and the reflectivity series based on the wave equations (Mallick 2007), Zoeppritz equations (Kurt 2007; Liu et al. 2016; Skopintseva et al. 2011) or linearized approximations (Aki and Richards 1980; Buland and El Ouair 2006; Buland and Omre 2003b; Downton and Ursenbach 2006; Rabben and Ursin 2011; Xiao et al. 2020). The inversion can be performed according to deterministic or probabilistic inversion methods. For example, based on Aki and Richards linearized approximation, Hu et al. (2011) presents a joint AVO inversion technique in the Bayesian framework to extract seismic velocities and density parameters, Sengupta et al. (2021) perform Bayesian inversion directly in the depth domain by using linearized Aki and Richards equation, and Liu et al. (2021) present a joint PP and PS inversion method based on the calculation of a Jacobian matrix of the Zoeppritz approximation. In addition to gradient-based optimization, the Monte Carlo inversion method (Jin and Madariaga 1994) and Bayesian linearized AVO inversion technique based on Gaussian distributions (Buland and Omre 2003b; Tarantola 1987) have also been utilized to solve the inverse problems and quantify the uncertainty of the predicted model. Feng-Qi et al. (2013) present a Bayesian linearized pre-stack inversion based on a trivariate Cauchy distribution. Ensemble-based methods such as ensemble Kalman filter and ensemble smoother (Evensen et al. 2009) have been successfully applied to inverse and data assimilation problems, especially for history matching of borehole and geophysical data. For example, Luo et al. (2015) developed an iterative ensemble smoother based on a regularized Levenberg-Marquardt (RLM) algorithm for reservoir data assimilation, and Luo et al. (2017) applied the iterative ensemble smoother to 4D-seismic history-matching. Kolbjørnsen et al. (2020) develop a Bayesian inversion for litho-geofluids prediction and Grana (2020) extends the Bayesian litho-geofluids approach to multiple prior models. Bayesian methods can also be integrated with stochastic sampling. For example, Azevedo et al. (2020) uses the stochastic perturbation optimization approach for the inversion of seismic data for rock properties and facies. In the Bayesian method, prior information about the subsurface model is included in the inversion in the form of probability distributions (Gouveia and Scales 1997). However, the prior information is often difficult to define and the prior uncertainty generally impacts the model predictions.

In deterministic methods, the goal is to predict a best-fit model that is consistent with the observed data, according to the objective or cost function that defines the dissimilarity between the true data and the predicted model. The inversion is performed by searching for the optimal model that minimizes the objective function. Numerous iterative algorithms such as the Levenberg-Marquardt (LM) algorithm (Levenberg 1944; Marquardt 1963), Occam's inversion (Constable et al. 1987), genetic algorithm (Mallick 1995), conjugate gradient method (Golub and Van Loan 2013), simulated annealing method (Ma 2001) and particle swarm optimization (Shaw and Srivastava 2007) have been introduced for solving the least-squares optimization problem. These methods have been used in seismic AVO inversion problems. For example, Luo et al. (2020a) and Luo et al. (2020b) adopt the Fréchet derivatives to compute the derivatives of the propagator matrix with respect to variables and used the L-BFGS approach for the optimization of the objective function.

2. Constrained non-linear AVO inversion based on the adjoint-state optimization

In this work, we present a constrained non-linear AVO inversion scheme based on the Aki and Richards linearized approximation, and the inversion algorithm is based on the minimization of an objective function. We adopt a gradient descent optimization algorithm depending on the calculation of the gradients of the L2-norm objective function with respect to the elastic properties, P- and S-wave velocities, and density. The adjoint-state numerical technique (Plessix 2006) is used for computing the gradients of the objective function efficiently by employing zero-lag cross-correlation between forward and reverse propagated data residual. The adjoint state solves a linear system and computes the gradient of the objective function. The advantage of this method is that the computational cost of computing the gradient is in practice independent of the number of model variables (N). Hence, the number of forwarding models required to compute the gradients through the adjoint-state method is independent of the number of unknown model variables. This makes adjoint-state faster and more efficient than other methods, such as finite difference and Fréchet derivatives (Plessix 2006). Adjoint methods have been recently used in several geophysical inversion problems including seismic full waveform inversion (Assis and Schleicher 2021; Biondi et al. 2021; Hu et al. 2021; Le et al. 2020; Pan et al. 2020; Ravasi and Vasconcelos 2021; Zheglova and Malcolm 2019; Zhu et al. 2021). Furthermore, the gradient equations obtained via the adjoint-state technique are exact within the numerical precision (Epelle and Gerogiorgis 2020). In this work, to minimize the L2-norm objective function, we use the L-BFGS method (Broyden 1970; Fletcher 1970; Goldfarb 1970; Liu and Nocedal 1989; Nocedal 1980; Shanno 1970), a widely used version of the quasi-Newton iteration method that does not explicitly calculate the Hessian operator, which reduces the computing time and memory storage, unlike other classical iterative methods such as Newton-Raphson or Gauss-Newton methods (Tarantola 2005). Indeed, the L-BFGS method exclusively stores model information from a limited number of previous l iterations (usually $l \leq 10$) and provides much faster computational time and improved convergence rates for geophysical inverse problems (Brossier et al. 2010). The main novelty of the proposed approach is the calculation of the gradient of the objective function with respect to the elastic properties using the adjoint-state method. The analytical derivatives computed by the adjoint state lead to advantages in computational and numerical performance. To stabilize our AVO inversion results, especially in the case of noisy data, we apply a Tikhonov regularization method (Aster et al. 2018). The Tikhonov regularization weights improve the stability of the solution and the accuracy of the optimal model.

We tested the proposed approach using synthetic well logs and seismic data generated for the Edvard Grieg oil field, in the North Sea, with different noise levels. We also adopt the staggered-grid finite difference (FD) method (Virieux 1986) to simulate the seismic response. The FD approach contains wave propagation effects such as seismic refraction, reflection, multiple reflections, and offset-dependent geometrical spreading. To reconcile the results of the convolutional approximation, we define an amplitude scaling factor that compensates for the effects of offset-dependent geometrical spreading and provides a good match between the two seismic modeling approaches.

In the following, we first discuss the seismic forward modeling approaches including, the convolutional model and the finite difference method. Then, we describe the mathematical formulation for the proposed non-linear inversion algorithm based on the adjoint-state technique. Next, we illustrate the implementation of the inversion

algorithm to a synthetic multilayered dataset, with and without seismic noise, obtained from well logs assuming no multiples nor other wave propagation effects. Then, a 2D synthetic data example with complex structural features such as inclined strata and faults, is presented. Finally, we apply the approach to a synthetic dataset based on the velocity-stress finite difference (FD) model, including wave propagation effects.

2.3 Method

2.3.1 Seismic modeling

In AVO studies, seismic amplitudes are approximated by a convolutional model. In continuous form, the convolutional model is written as:

$$d(t,\theta) = \int W(\tau,\,\theta) R_{PP}(t-\tau,\,\theta) d(\tau) \tag{2.1}$$

where d, R_{PP}, and W are the seismic data, reflectivity, and wavelet respectively. In equation 2.1, t is the two-way travel time (TWT), and θ is the incident angle. This approximation does not consider multiples and wave propagation effects like offset-dependent geometrical spreading, attenuation, or absorption effects. The Ricker wavelet (Ricker 1953) is commonly used for the convolutional model:

$$W(t) = \left(1 - \frac{1}{2}\omega_\circ^2 t^2\right) \exp\left(-\frac{1}{4}\omega_\circ^2 t^2\right) \tag{2.2}$$

whereas $\omega_\circ$ is the dominant frequency. The reflectivity function R_{PP} represents the reflection coefficients of P-to-P waves as a function of t and θ and is often modeled using Aki and Richards equation (Aki and Richards 1980), which is a linear approximation of the non-linear Zoeppritz equation (Zoeppritz 1919) for weak elastic contrasts across the geological layers. For incident angles less than the acquisition critical angle, the Aki and Richards equation provides an accurate approximation of the reflection coefficients for small elastic contrasts. In theory, the proposed methodology could be extended to the Zoeppritz equation, however, the analytical evaluation of the mathematical formulation of the gradient is more challenging to derive. The discrete version of Aki and Richards approximation for R_{PP} is:

$$\begin{aligned} R_{PP_{[i]}}(\theta) = &\frac{1}{2}\left(1+\tan^2\theta\right)\frac{\Delta\alpha[i]}{\alpha[i]} - 4\left(\frac{\beta[i]}{\alpha[i]}\right)^2 \frac{\Delta\beta[i]}{\beta[i]}\sin^2\theta \\ &+\frac{1}{2}\left[1 - 4\left(\frac{\beta[i]}{\alpha[i]}\right)^2 \sin^2\theta\right]\frac{\Delta\rho[i]}{\rho[i]} \end{aligned} \tag{2.3}$$

where $\Delta\alpha$, $\Delta\beta$, and $\Delta\rho$ are the variations P- and S-wave velocities and density across the reflecting interface i whereas α, β and ρ are the corresponding average P- and S-wave velocities and density.

Alternatively, the seismic response can be modeled by solving the wave equation. The finite difference (FD) method is often adopted to approximate the partial derivatives of the wave equation and compute the propagation of seismic waves (Carcione et al.

1988). Several numerical schemes have been proposed. In this work, we adopt a high order (8^{th}) staggered-grid FD scheme (Virieux 1986) to numerically model in a discretized grid the P-SV elastic seismic energy propagating through a heterogeneous medium using the velocity-stress field. At the time 0, the wave propagating medium is considered to be in equilibrium; then. time-integrated particle velocity and stress are propagated. Absorbing boundary conditions (ABCs) are generally assumed for the mathematical simulation of seismic wave propagation, to avoid artificial boundary reflection (ABR). In our approach, we consider a perfectly matched layer (PML) to attenuate modeling boundary reflections. The numerical formulation for the velocity-stress FD method is given by Virieux (1986). In this work, we adopt this formulation to compute a synthetic dataset with a different operator than the convolutional model used for the inversion, to validate the proposed formulation.

2.3.2 AVO inversion

The forward modeling equation of seismic AVO inversion is written as $f(m) = d$, where m represents the unknown model variables. The objective of inverse modeling is to estimate the model variables m from the seismic AVO data d. In the proposed formulation, m represents the elastic model variables as $m = [V_P(t), V_S(t), \rho(t)]$, including P- and S-wave velocities and density.

To solve the inverse problem, we first define an objective function to model the misfit $J = d - f(m)$ between the real and predicted data, and then implement an optimization algorithm to minimize the objective function. Numerous options for the definition of the objective functions are available in the literature (Alessandrini et al. 2019; Faucher et al. 2019). We use the Euclidean norm ($L2$-norm), as it is widely used in inversion, especially for problems with a natural scattering of the error components. Mathematically, the $L2$-norm objective function is written as:

$$J(m) = \frac{1}{2} \parallel d(t, \theta) - f(m(t, \theta)) \parallel^2 \tag{2.4}$$

In our approach, the forward modeling operator is given by the convolutional model:

$$f(m) = W(t) * R_{PP}(t, \theta | m) + n(t, \theta) \tag{2.5}$$

here, the term n represents the random ambient noise and * indicates convolution.

The optimization requires the calculation of the partial derivatives of the gradient $\left(\frac{\partial J}{\partial V_P}, \frac{\partial J}{\partial V_S}, \frac{\partial J}{\partial \rho}\right)$ of the objective function J with respect to elastic properties (V_P, V_S, ρ).

We adopt the adjoint-state technique to calculate the gradient of the objective function. The adjoint-state solution of Aki and Richards equation (1980) and derivation of the gradient is given in Appendix A. The so-obtained partial derivatives with respect to (V_P, V_S, ρ) at a given interface i are:

$$\begin{aligned}\frac{\partial J}{\partial V_P[i]} &= \frac{1}{2}\left(1+\tan^2\theta\right)\left[-\frac{1}{\alpha[i]}-\frac{\Delta\alpha[i]}{2\alpha[i]^2}\right]\cdot\lambda[i] \\ &+\frac{1}{2}\left(1+\tan^2\theta\right)\left[\frac{1}{\alpha[i-1]}-\frac{\Delta\alpha[i-1]}{2\alpha[i-1]^2}\right]\cdot\lambda[i-1] \\ &+\left(\frac{2\beta[i-1]^2}{\alpha[i-1]^3}\right)\left[2\frac{\Delta\beta[i-1]}{\beta[i-1]}+\frac{\Delta\rho[i-1]}{\rho[i-1]}\right]\cdot\sin^2\theta\cdot\lambda[i-1] \\ &+\left(\frac{2\beta[i]^2}{\alpha[i]^3}\right)\left[2\frac{\Delta\beta[i]}{\beta[i]}+\frac{\Delta\rho[i]}{\rho[i]}\right]\cdot\sin^2\theta\cdot\lambda[i]\end{aligned} \tag{2.6}$$

$$\begin{aligned}\frac{\partial J}{\partial V_S[i]} &= \left[-\frac{2\Delta\beta[i-1]}{\alpha[i-1]^2}-\frac{4\beta[i-1]}{\alpha[i-1]^2}\right]\cdot\sin^2\theta\cdot\lambda[i-1] \\ &-\left[\frac{2\Delta\beta[i]}{\alpha[i]^2}-\frac{4\beta[i]}{\alpha[i]^2}\right]\cdot\sin^2\theta\cdot\lambda[i] \\ &-\left[\frac{2\beta[i-1]}{\alpha[i-1]^2}\cdot\frac{\Delta\rho[i-1]}{\rho[i-1]}\right]\cdot\sin^2\theta\cdot\lambda[i-1] \\ &-\left[\frac{2\beta[i]}{\alpha[i]^2}\cdot\frac{\Delta\rho[i]}{\rho[i]}\right]\cdot\sin^2\theta\cdot\lambda[i]\end{aligned} \tag{2.7}$$

and

$$\begin{aligned}\frac{\partial J}{\partial \rho[i]} &= +\frac{1}{2}\left[1-4\left(\frac{\beta[i-1]}{\alpha[i-1]}\right)^2\cdot\sin^2\theta\right]\left[\frac{1}{\rho[i-1]}-\frac{\Delta\rho[i-1]}{2\rho[i-1]^2}\right]\cdot\lambda[i-1] \\ &-\frac{1}{2}\left[1-4\left(\frac{\beta[i]}{\alpha[i]}\right)^2\cdot\sin^2\theta\right]\left[\frac{1}{\rho[i]}+\frac{\Delta\rho[i]}{2\rho[i]^2}\right]\cdot\lambda[i]\end{aligned} \tag{2.8}$$

We then apply a non-linear optimization algorithm, namely L-BFGS, to update the model variables by minimizing the objective function J according to the L-BFGS iteration equation 2.9. L-BFGS is a limited-memory quasi-Newton optimization method often used for solving large-scale non-linear optimization problems where the Hessian cannot be efficiently computed. The L-BFGS optimization method iteratively approximates the inverse Hessian using the curvature information from the previous iterations. The L-BFGS optimization method can be represented as:

$$m_{k+1} = m_k - \alpha_k H_k \nabla J, \qquad k = 0,1,2,3,..., \tag{2.9}$$

where k represents the iteration, α_k is the scalar step length at iteration k, ∇J is the gradient of the objective function respectively, and H_k describes the inverse Hessian approximation ($H_k \approx \nabla^2 J^{-1}$) at iteration k. The inverse Hessian H_k is approximated as:

$$H_{k+1} = V_k^T H_k V_k + \rho_k s_k s_k^T \tag{2.10}$$

where $V_k = I - \rho_k y_k s_k^T$, $s_k = m_{k+1} - m_k$, $y_k = \nabla J(m_{k+1}) - \nabla J(m_k)$, and $\rho_k = (y_k^T s_k)^{-1}$.

In the L-BFGS method, the Hessian approximation is more efficient than in the original BFGS method. At a given iteration k, suppose that the current solution is m and the vector pairs of the previous p iterations are $\{s_i, y_i\}$ for $i = k-p, ..., k-1$ with associated matrices V_i and scalars ρ_i. We choose an initial H_k° and compute H_k as:

$$\begin{aligned} H_k = &\left(V_{k-1}^T ... V_{k-p}^T\right) H_k^\circ \left(V_{k-p} ... V_{k-1}\right) \\ &+\rho_{k-p} \left(V_{k-1}^T ... V_{k-p+1}^T\right) s_{k-p} s_{k-p}^T \left(V_{k-p+1} ... V_{k-1}\right) \\ &+\rho_{k-p+1} \left(V_{k-1}^T ... V_{k-p+2}^T\right) s_{k-p+1} s_{k-p+1}^T \left(V_{k-p+2} ... V_{k-1}\right) \\ &+... \\ &+\rho_{k-1} s_{k-1} s_{k-1}^T \end{aligned} \tag{2.11}$$

We then define a recursive procedure to efficiently calculate the product $H_k \nabla J_k$, as shown in Algorithm 2.1.

Algorithm 2.1: Limited-memory BFGS two-loops recursion.

1. **Inputs:** $\nabla J_k, H_k$
2. $q \leftarrow \nabla J_k$
3. **for** $i = k-1, k-2, ..., k-p$ **do**
4. $\alpha_i \leftarrow \rho_i s_i^T q$;
5. $q \leftarrow q - \alpha_i y_i$;
6. **end (for)**
7. $r \leftarrow H_k^o q$
8. **for** $i = k-p, k-p+1, ..., k-1$ **do**
9. $\beta_i \leftarrow \rho_i y_i^T r$;
10. $r \leftarrow r + s_i(\alpha_i - \beta)$;
11. **end (for)**
12. **Stop** with result $H_k \nabla J_k = r$

2.4 Applications

We present numerous numerical examples of synthetic and field datasets used to validate the proposed inversion using the traditional convolutional model. We then extend the application to a synthetic dataset generated using the FD method. Two synthetic subsurface profiles, namely example 1 and example 2, are generated from well logs using the convolutional model. Then the inversion is extended to synthetic 2D data generated from an elastic model developed for the Edvard Grieg oil field in the North Sea.

In example 1, we use a multilayered convolution model to simulate the synthetic angle gathers from a set of synthetic well logs data. S-wave velocity and density are computed from P-wave velocity using Castagna's relation (Castagna et al. 1985) and Gardner's equation (Gardner et al. 1974) respectively. The true model variables and the initial guesses are shown in Fig. 2.1.

Synthetic AVO seismic gathers up to the maximum angle of incidence 30° are generated by convolving a 25 Hz Ricker seismic wavelet with PP reflectivity series

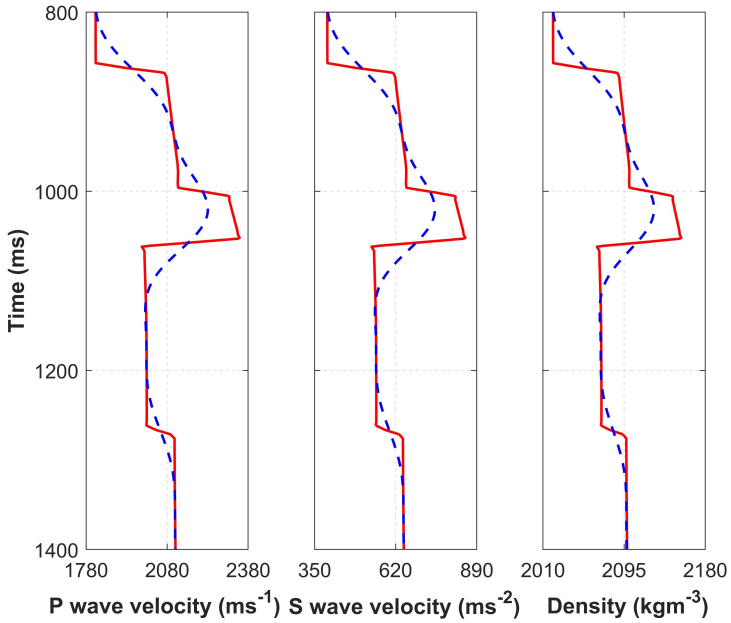

Figure 2.1: Example 1 - Model variables (solid red lines): the P and S wave velocities in (m/s) and the bulk density in $(kg \cdot m^{-3})$ and the corresponding initial guesses (dashed blue lines) at the well location in the TWT interval 800 - 1400 ms are plotted in the figure.

calculated with the linearized Aki and Richards equation. The pre-stack angle gather profiles without and with seismic random noise levels (S/N = 50) are shown in Fig. 2.2. Fig. 2.3 represents the inverted P wave velocity, S wave velocity, and density from noise-free AVO seismic gather. The inverted variables are in good agreement with the true model variables. Fig. 2.4 shows the corresponding seismic response of the true, initial, and inverted models as well as the percent error between true and predicted seismic gathers. The inversion results prove the accuracy of this inversion approach. The AVO inversion results with a signal-to-noise ratio (S/N) of 50 are shown in Fig. 2.5. The inversion results show a good agreement and are consistent with real models, despite some slight instability of the solution at quite a few points, especially for S-wave velocity. We speculate that the local instability of the solution might be due to the discrete nature of the model and the band-limited nature of the data. The local instability can be mitigated using a regularization method such as total variation regularization.

We then test the inversion using a synthetic seismic dataset generated from high-frequency acoustic and shear sonic logs and density data, measured in the Edvard Grieg oil field. These reference elastic properties V_P, V_S, and ρ along with initial models are shown in Fig. 2.6. The presented true well log measurements (Fig. 2.6) are upscaled to estimate the model variables at the seismic scale (i.e. seismic wavelet scale) from the

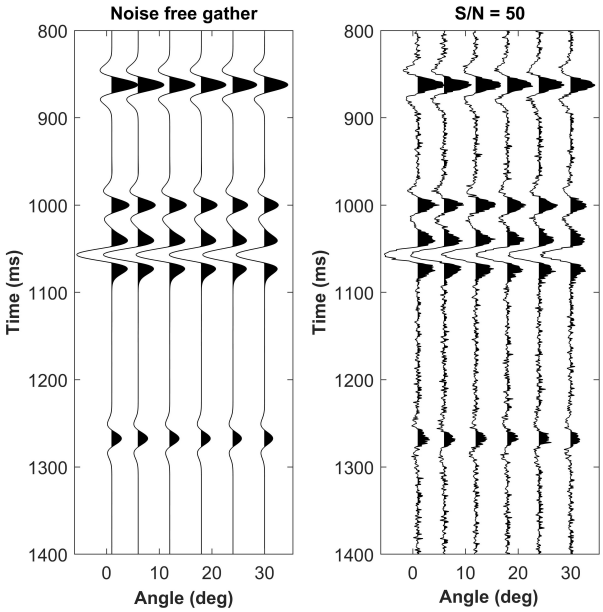

Figure 2.2: Example 1 - Pre-stack amplitude versus angle (AVA) gathers with different seismic noise levels (without and with S/N = 50) up to maximum incident angle 30°.

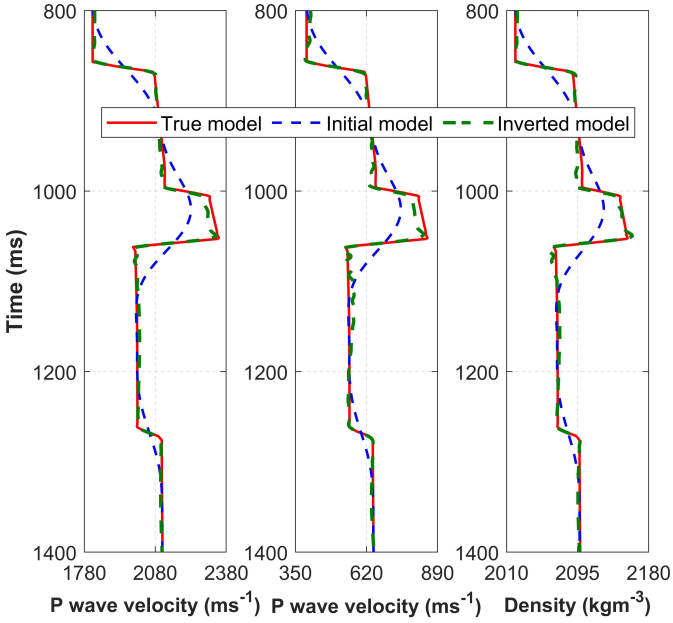

Figure 2.3: Example 1 - Inverted P- and S-wave velocities (V_P, V_S) and density (ρ) models obtained from noise-free AVO gathers.

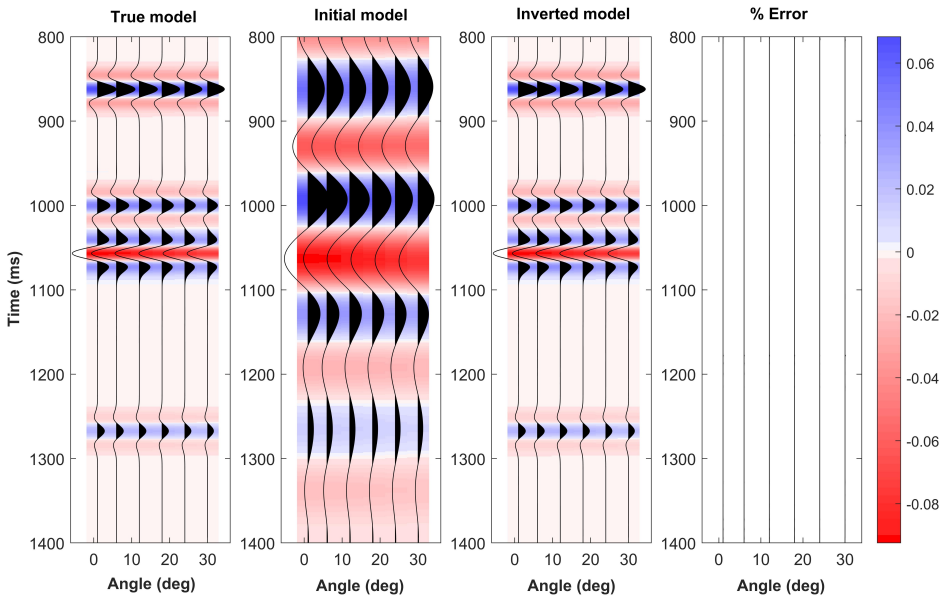

Figure 2.4: Example 1 - AVA seismic response (up to 30°) for baseline true model, initial model, and inverted model and estimated percent error.

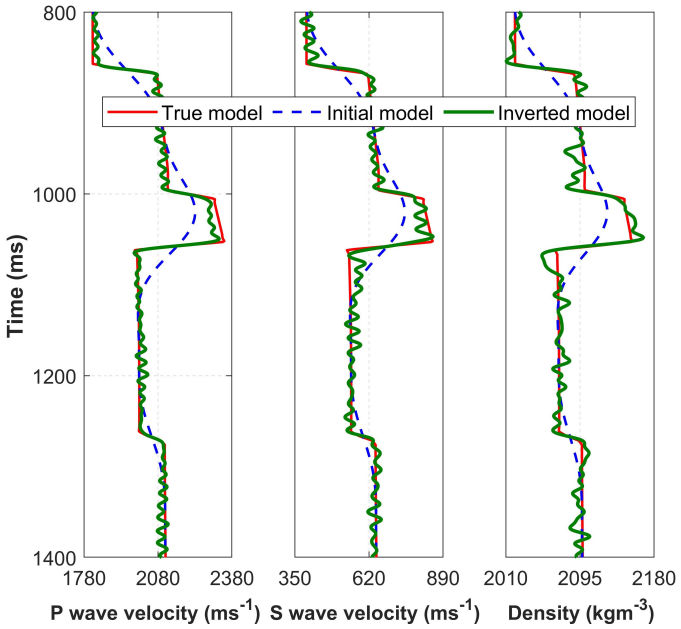

Figure 2.5: Example 1 - Inverted P- and S-wave velocities (V_P, V_S) and density (ρ) models obtained from noisy (S/N = 50) seismic AVO gather.

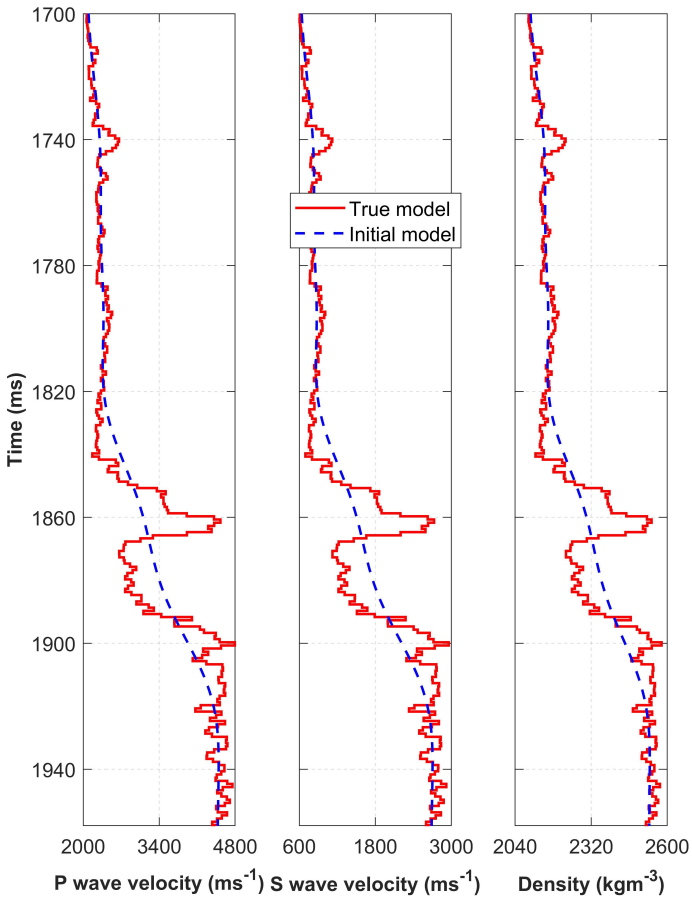

Figure 2.6: Example 2 - Model variables: P and S wave velocities in (m/s) and bulk density in $(kg \cdot m^{-3})$ along with corresponding initial models at the well location in the TWT interval 1700 - 1965 ms.

higher frequency properties (i.e. sonic log). The reservoir zone is located between 1867 - 1888 ms. The convolution-based seismic forward modeling is used to generate pre-stack seismic AVA gathers (Fig. 2.7) without noise and with S/N = 50. The range of angles of the incident for seismic waves is from $0 - 30^o$ with an interval of 5^o. Figs. 2.8 and 2.9 show the AVA inversion results without and with noise. In the noise-free case, the comparison between true and inverted models shows that the results are accurate (Fig. 2.8). Similarly, in the noise-added case, the results also show very good agreement with the true models (Fig. 2.9) and are consistent with the real models. However, the inverted results are presented in Figs. 2.8 and 2.9 are after applying small weight Tikhonov regularization to the density and the shear wave velocity.

We then apply the inversion approach to a synthetic dataset built using the Edvard

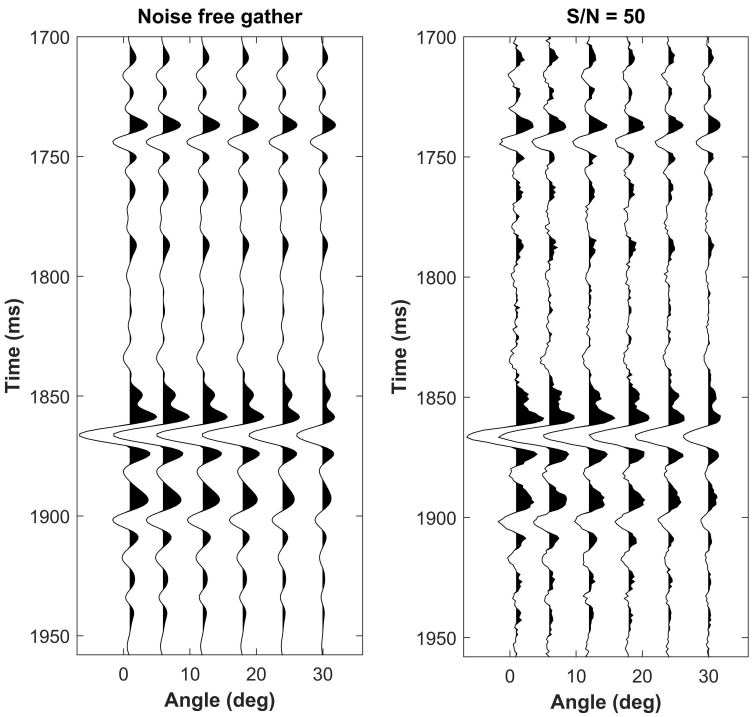

Figure 2.7: Example 2 - Pre-stack amplitude versus angle (AVA) gathers with different seismic noise levels (without and with S/N = 50) up to maximum incident angle 30°.

Grieg measured data along a section including horizontal and inclined stratigraphy and faulted geological layers. We adopt an elastic model obtained in previous studies (referred to as the true model in the following) to generate a synthetic seismic line. The seismic line comprises 38 common depth points (CDP) and the AVO inversion is applied trace by trace. The time window is from 500 - 2500 ms. Figs. 2.10 - 2.12 show the inversion results for P- and S-wave velocity and density, respectively. Each figure shows the comparison between the initial model, true model, and inverted results for all CDPs. For each model variable, we compute the percent error between true and predicted models. The inversion shows accurate results for P-wave velocity, whereas density values are slightly under-predicted in the bottom part of the interval, and S-wave velocity is mismatched in the reservoir region. Fig. 2.13 shows the full stack of the seismic dataset, obtained after stacking the AVO gathers generated at each trace location, and the seismic response of the inverted model, showing an overall agreement between data and predictions. In some of the inversion results, the correlation between the predicted elastic properties is overestimated, possibly due to the linearization in the inverse problem. This is a common effect in seismic and petrophysical inversion, due to the correlation of the seismic angles introduced in the processing which reduces the degrees of freedom of the solution and makes the problem underestimated.

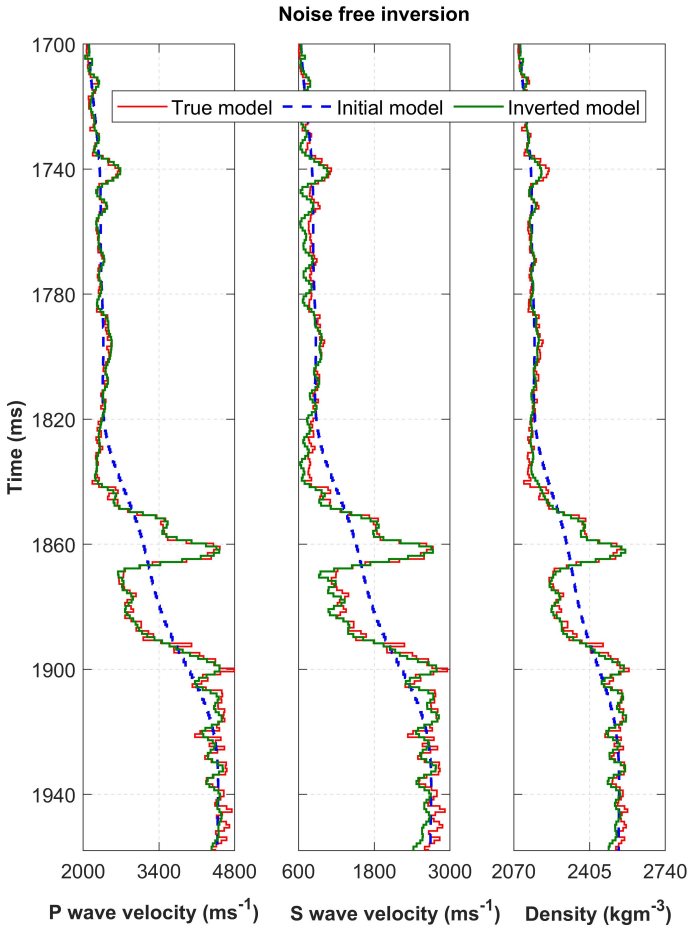

Figure 2.8: Example 2 - Inverted P- and S-wave velocities (V_P, V_S) and density (ρ) models obtained from noise-free AVO gathers.

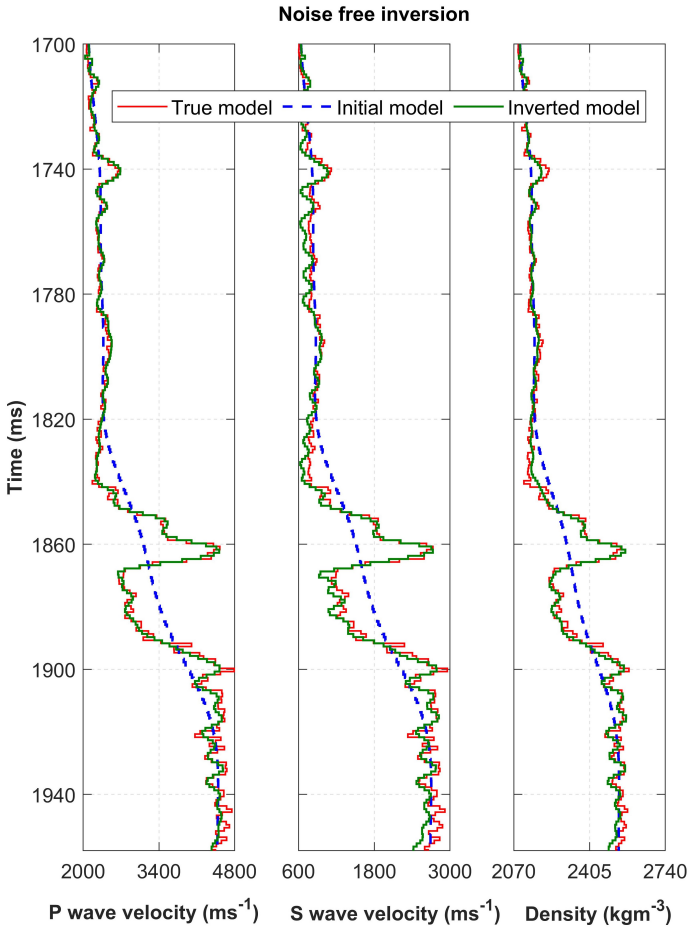

Figure 2.9: Example 2 - Inverted P- and S-wave velocities (V_P, V_S) and density (ρ) models obtained from noisy (S/N = 50) seismic AVO gather.

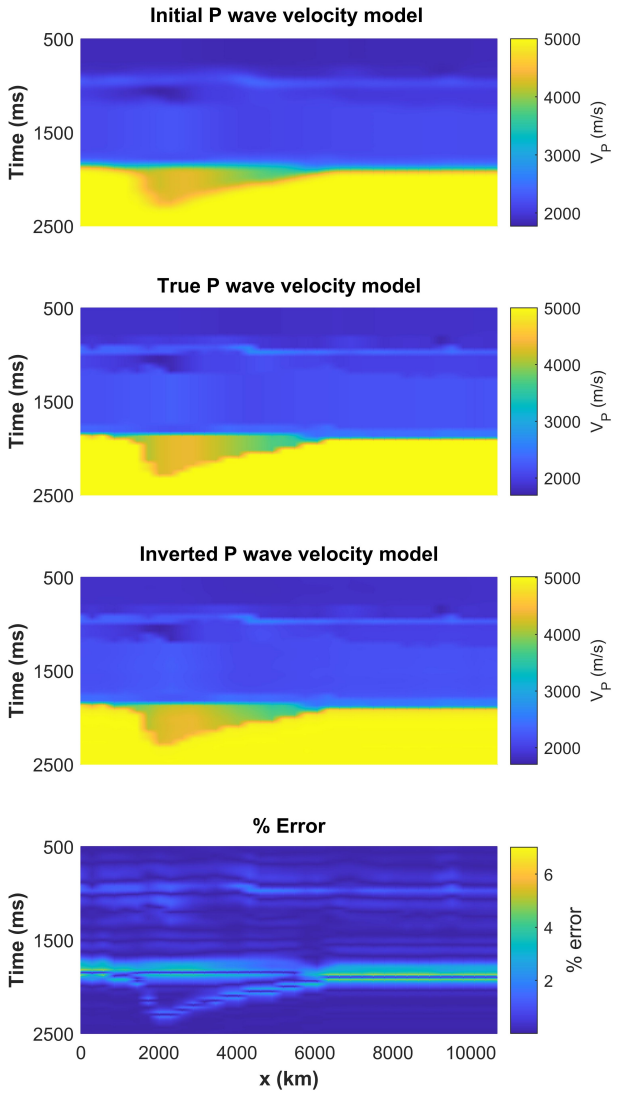

Figure 2.10: 2D profile of inverted P-wave velocity compared to the true and initial models. The percent errors between true and inverted models are also displayed.

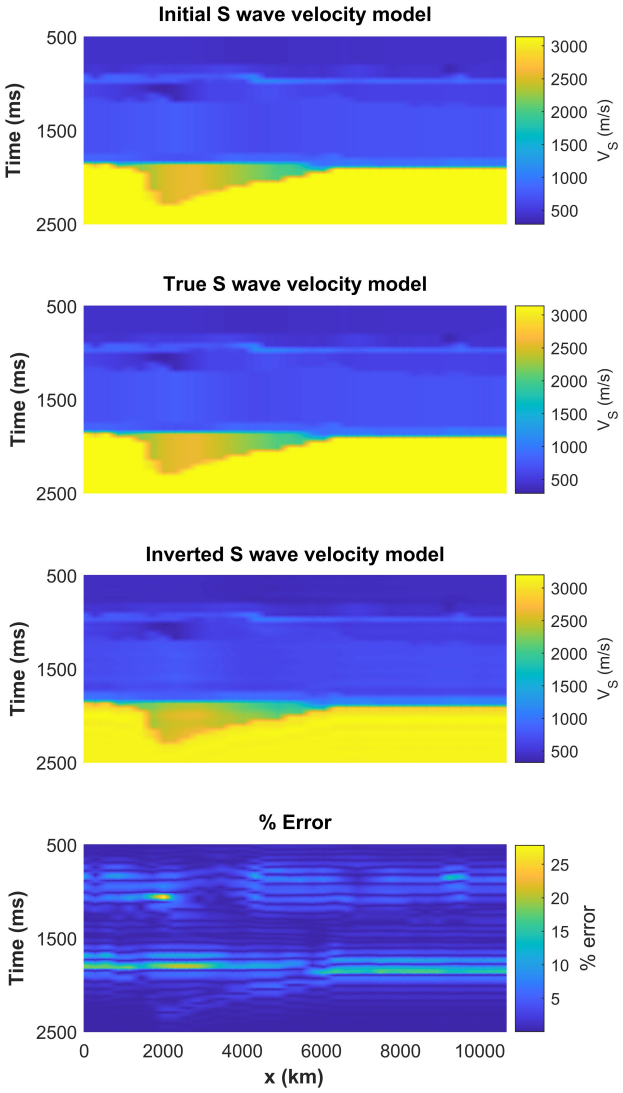

Figure 2.11: 2D profile of inverted S-wave velocity compared to the initial and true models. The percent errors are also displayed.

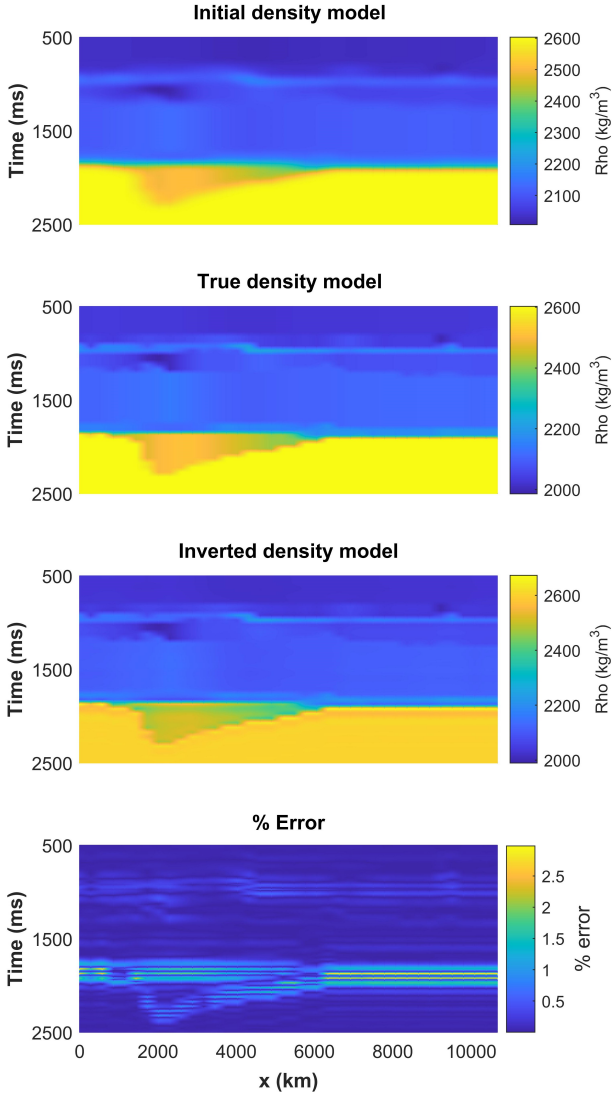

Figure 2.12: 2D profile of inverted density compared to the initial and true models. The percent errors between the true and predicted models are also displayed.

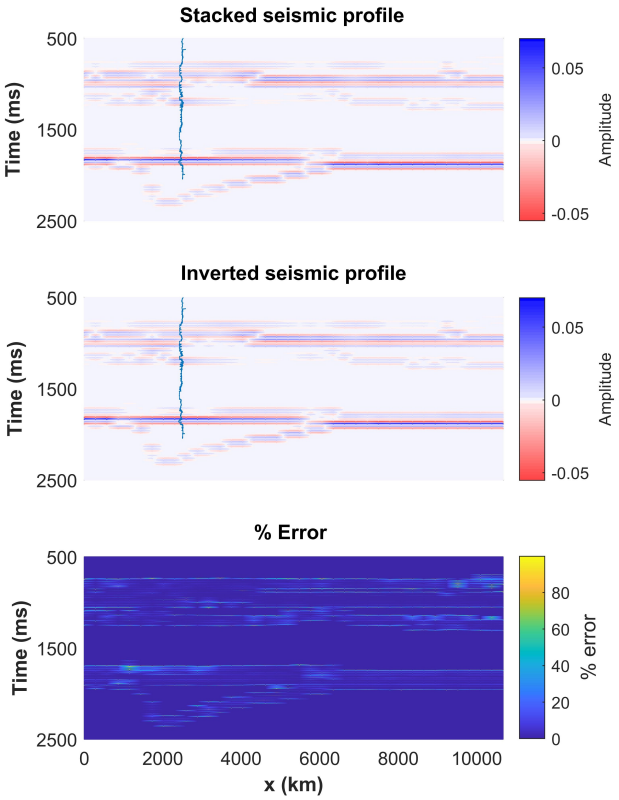

Figure 2.13: Full stack seismic section compared to the seismic response of the inverted seismic profile and percent errors between real and inverted seismic profiles.

We extend the inversion to a seismic dataset generated using the staggered-grid finite difference model of elastic waves. We first generate the synthetic seismic by computing the forward model for the entire section from the surface and extracting the reservoir layer between 1700 and 1888 ms. We perform normal moveout (NMO) correction offset-to-angle transformation and apply an amplitude scaling factor to remove the effects of offset-dependent geometrical spreading. The wavelet with a dominant frequency of 25 Hz is used for the FD model. We assumed a layered isotropic elastic medium with elastic properties given in Fig. 2.1 and simulated an OBC seismic survey. The number of receiver points is 1001 with a constant distance of 5 m, for a 5000 m maximum offset. The recording interval is 0.002 seconds. The synthetic seismograms generated by the finite difference simulations are shown in Fig. 2.14. The overburden layers extend to 1750 m, whereas the reservoir layer is between 1750 and 1940 m, such that the overburden reflections and associated interbedded multiples are subtracted from the model. The FD results at the top of the reservoir are shown in (Fig. 2.14c). As the staggered-grid finite difference modeling considers all the wave propagation effects, in order to implement a convolutional model-based inversion scheme for FD synthetic

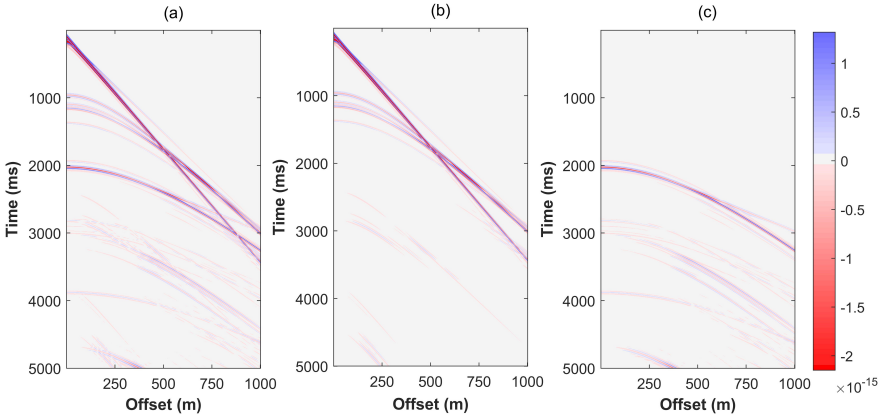

Figure 2.14: Seismic records obtained with staggered-grid finite difference methods: a) full model; b) overburden model; c) reservoir model obtained by subtracting the overburden from the full model.

angles gathers, we have defined an amplitude scaling factor that compensates the effects of geometrical spreading for FD seismic profiles and provides the best calibration between synthetics of both methods. The derivation of the amplitude scaling factor is described in Appendix B. The comparison between convolution and FD models at the reservoir zone level, after the application of the scaling factor, is shown in Fig. 2.15. We then run the inversion scheme assuming the FD model until incident angle 18°. The results of the proposed adjoint-state-based inversion applied to the staggered-grid FD model are shown in Figs. 2.16 and 2.17. Overall, the inverted P- and S-wave seismic velocities and density show good agreement with the true models, despite some discrepancies. Fig. 2.17 shows the synthetic angle gathers for the initial, true, and inverted models plotted trace by trace up to 18°, showing a good match.

2.5 Discussion

In the gradient descent-based optimization algorithms, it is necessary to compute the gradient equations of the least-square objective function with respect to unknown elastic variables. The efficiency of the algorithm relies on the accuracy and effectiveness of the computation of the gradient. To efficiently and accurately compute the gradient, we adopt the adjoint-state technique. The adjoint-state variables do not depend on the perturbations of the model variables. We apply the method under the non-linear constraints and derive the set of gradient equations for the objective function. The advantage of using the adjoint-state method is that it only requires solving one additional linear system, which makes the inversion more efficient than the Fréchet derivative approach (Plessix 2006). The optimization problem is then solved by using the L-BFGS optimizer of the non-linear quasi-Newton class based on the gradient computed with the adjoint-state method. The non-linear L-BFGS approximates the inverse Hessian matrix by using a few previous iterations ($l < 10$) and consequently reduces computational

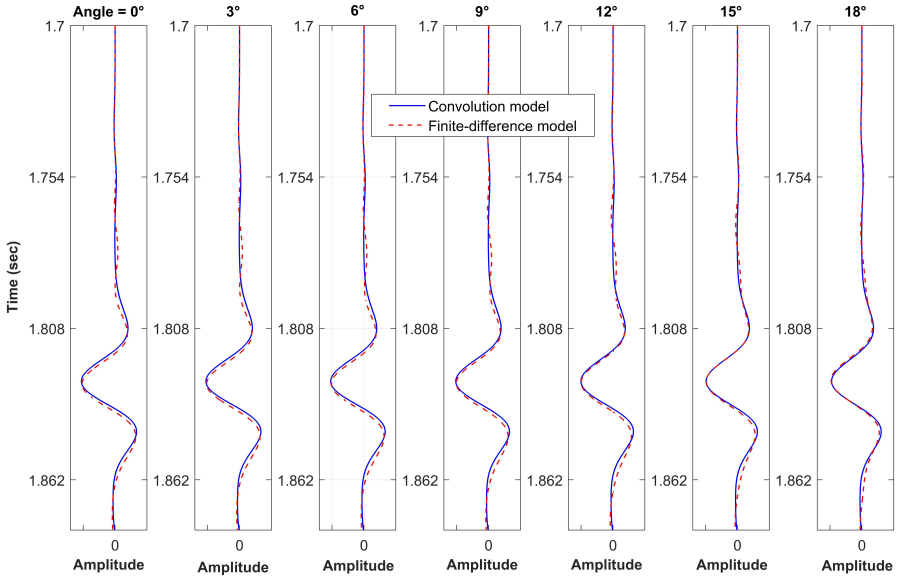

Figure 2.15: Comparison between synthetic data modeled by using convolution and finite difference models after correcting the offset-dependent geometrical spreading.

load and makes the algorithm more efficient than the traditional Newton-Raphson and Gauss-Newton methods. The proposed approach is tested on several examples based on two different forward models: the traditional convolutional approach and the FD method. The adjoint-state-based inversion method for the elastic properties can be theoretically applied to other properties e.g., seismic impedances, velocity ratio, or petrophysical parameters e.g., porosity, fluid saturation, clay volume, etc., by calculating the gradients with respect to the selected parameterization using the chain rule of derivative and by incorporating adequate rock-physics relations (as described in Chapter 3). The proposed inversion method can also be applied to other angle-dependent reflectivity operators such as Zoeppritz equations or their approximations (Fatti et al. 1994; Shuey 1985).

2.6 Conclusions

We presented a non-linear seismic AVO inversion method based on a deterministic approach for the minimization of the objective function. The objective function is based on the convolutional model where the reflectivity is obtained using linearized Aki and Richards approximation. The gradient of the objective function is calculated by using the adjoint-state technique. The adjoint state is computationally fast and more effective than traditional numerical methods. The minimization problem is iteratively solved by using L-BFGS, a non-linear optimization algorithm that approximates the inverse of Hessian and improves the convergence rate for inversion results. The applications of the proposed inversion scheme show accurate results for synthetic seismic data computed

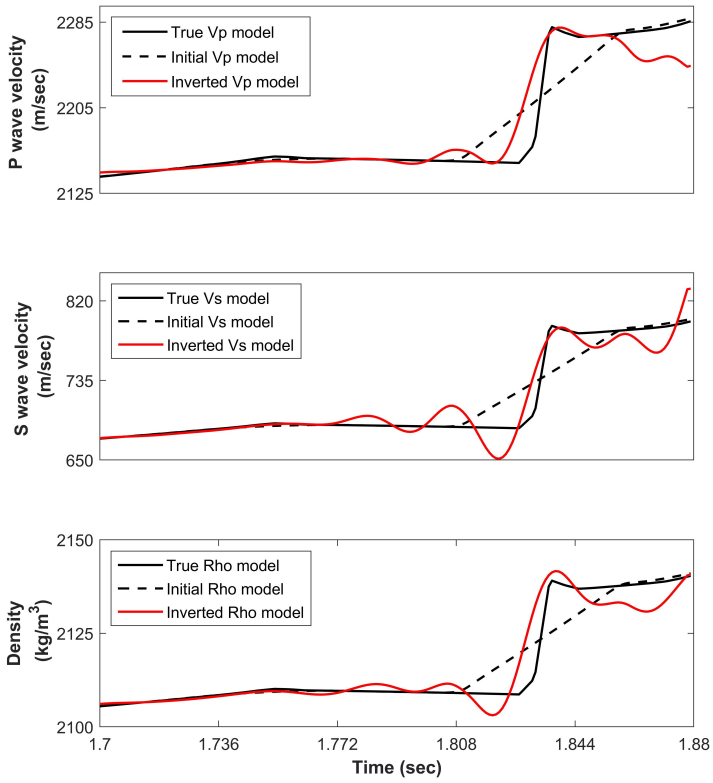

Figure 2.16: Inverted P- and S-wave velocities (V_P, V_S) and density (ρ) at the top of the reservoir (1.7 - 1.88 sec).

using the convolutional model as well as the staggered-grid finite difference method. The estimated synthetic angle gather which is computed from the inversion results matches the true data in both cases. The adjoint-state-based AVO inversion method can be applied to the different parameterizations of the model by using the chain rule of differentiation.

2.7 Acknowledgments

The authors would like to express gratitude to the National IOR Centre of Norway led by the University of Stavanger for the financial support of this project. The authors also acknowledge Lundin Energy Norway and their partners Wintershall Dea and OMW in the Edvard Grieg license for providing the seismic and well logs for this project. The authors are thankful to Patrick Connolly (Patrick Connolly Associates Ltd.) for reviewing and having some good discussions about the paper. Nisar Ahmed is thankful to Tien Hoang Nguyen (Research Fellow at IER, UiS) for a nice discussion about the Edvard Grieg oil field and for helping to extract the 2D velocity model. The

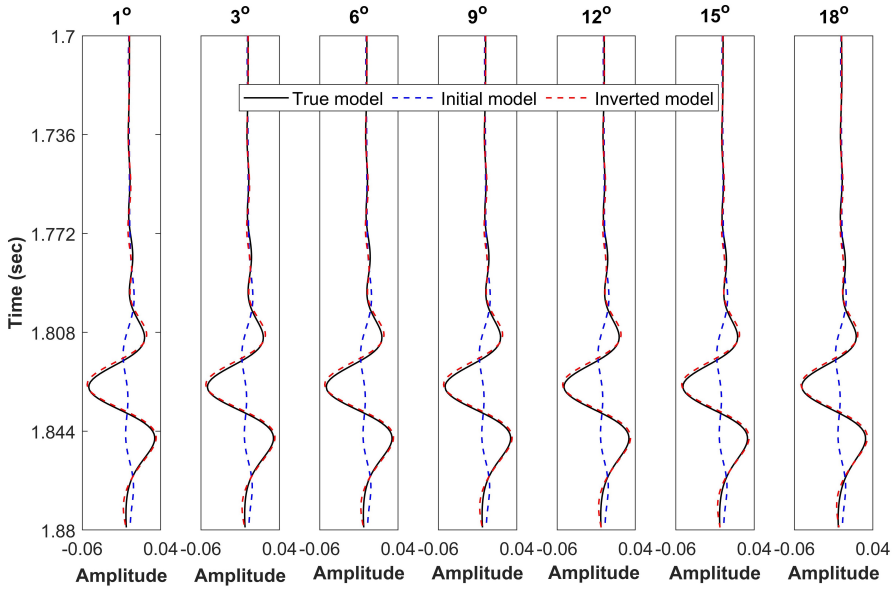

Figure 2.17: Pre-stack amplitude versus angle (AVA) gathers based on true model simulated by staggered-grid finite difference method, initial model, and inverted model obtained with a convolutional approach.

computations and simulations were performed on resources provided by UNINETT Sigma2 - the National Infrastructure for High-Performance Computing and Data Storage in Norway.

2.8 Code availability section

Name of the code/library: Non-linear AVO Inversion
Contact: ahmedseis23@gmail.com
Hardware requirements: Standard personal computer
Program language: MATLAB
Software required: MATLAB
The source codes are available for download at the link:
https://github.com/nahmed215/avoinversion.git

2.9 Appendix A: Adjoint-state based gradients

The gradient ∇ of an objective function J given in the least-square equation 2.4, includes the partial derivatives of the objective function with respect to the model variables $m = [V_P(t), V_S(t), \rho(t)]$:

$$\nabla J = \left[\frac{\partial J(t)}{\partial V_P}, \frac{\partial J(t)}{\partial V_S}, \frac{\partial J(t)}{\partial \rho} \right] \tag{2.12}$$

Based on equation 2.4, the partial derivative of J are given by:

$$\frac{\partial J}{\partial V_P} = -\Big[d - f(V_P, V_S, \rho) \Big] \cdot \frac{\partial f}{\partial V_P} \tag{2.13}$$

$$\frac{\partial J}{\partial V_S} = -\Big[d - f(V_P, V_S, \rho) \Big] \cdot \frac{\partial f}{\partial V_S} \tag{2.14}$$

$$\frac{\partial J}{\partial \rho} = -\Big[d - f(V_P, V_S, \rho) \Big] \cdot \frac{\partial f}{\partial \rho} \tag{2.15}$$

In practical applications, elastic properties are discretized. We adopt the notation $V_P[i], V_S[i]$ and $\rho[i]$, for the value of the velocity at a given interface i. In the discretized domain, the terms $\left(\frac{\partial f}{\partial V_P[i]}\right)$, $\left(\frac{\partial f}{\partial V_S[i]}\right)$ and $\left(\frac{\partial f}{\partial \rho[i]}\right)$ represent the Jacobian matrix and are given by:

$$\frac{\partial f}{\partial V_P[i]} = -W * \frac{\partial R_{PP}(\theta)}{\partial V_P[i]} \tag{2.16}$$

$$\frac{\partial f}{\partial V_S[i]} = -W * \frac{\partial R_{PP}(\theta)}{\partial V_S[i]} \tag{2.17}$$

$$\frac{\partial f}{\partial \rho[i]} = -W * \frac{\partial R_{PP}(\theta)}{\partial \rho[i]} \tag{2.18}$$

We compute the gradient equations for each model variable using the adjoint method. In the AVO inverse problem, the Lagrangian function $(\mathcal{L})$ with the adjoint state variable λ is given by:

$$\begin{aligned} \mathcal{L}(V_P, V_S, \rho, R_{PP}, \lambda) &= \sum_i \int_\theta d\theta \Big[d[i] - W[i] * R_{PP}[i] \Big]^2 \\ &+ \sum_i \int_\theta d\theta \Big[R_{PP}[i] - A[i] \cdot \frac{\Delta\alpha}{\alpha} - B[i] \cdot \frac{\Delta\beta}{\beta} - C[i] \cdot \frac{\Delta\rho}{\rho} \Big] \lambda_{[i]} \end{aligned} \tag{2.19}$$

here,

$$A[i] = \left[\frac{1}{2} \left(1 + \tan^2\theta \right) \right] \qquad B[i] = \left[-\frac{4\beta[i]^2}{\alpha[i]^2} \cdot \sin^2\theta \right] \qquad C[i] = \frac{1}{2} \left[1 - \frac{4\beta[i]^2}{\alpha[i]^2} \cdot \sin^2\theta \right]$$

while,

$$\alpha[i] = \frac{V_P[i+1] + V_P[i]}{2} \qquad \Delta\alpha[i] = V_P[i+1] - V_P[i]$$

$$\beta[i] = \frac{V_S[i+1] + V_S[i]}{2} \qquad \Delta\beta[i] = V_S[i+1] - V_S[i]$$
$$\rho[i] = \frac{\rho[i+1] + \rho[i]}{2} \qquad \Delta\rho[i] = \rho[i+1] - \rho[i]$$

The Lagrangian in Equation 2.19 can be rewritten as $\mathcal{L} = \mathbf{J} + C * \lambda$, where C represents the constraints. The constraint in the Lagrangian multiplier is automatically satisfied if we compute R_{PP} using Aki and Richards equations as:

$$\left[R_{PP}[i] - A[i] \cdot \frac{\Delta\alpha}{\alpha} - B[i] \cdot \frac{\Delta\beta}{\beta} - C[i] \cdot \frac{\Delta\rho}{\rho}\right] = 0 \tag{2.20}$$

The gradient of the objective function $\boldsymbol{J}$ is achieved through the solution of the following system:

$$\frac{\partial\mathcal{L}}{\partial R_{PP}} = 0, \tag{2.21}$$

$$\frac{\partial\mathcal{L}}{\partial\lambda} = 0, \tag{2.22}$$

$$\begin{aligned}
\frac{\partial\mathcal{L}}{\partial V_P[i]} = \int_\theta d\theta \Bigg\{ & \frac{A}{\alpha[i-1]} \cdot \lambda[i-1] - \frac{A}{\alpha[i]} \cdot \lambda[i] \\
& - \frac{A\Delta\alpha[i-1]}{2\alpha[i-1]^2} \cdot \lambda[i-1] - \frac{A\Delta\alpha[i]}{2\alpha[i]^2} \cdot \lambda[i] \\
& + \frac{4\beta[i-1]^2}{\alpha[i-1]^3} \cdot \sin^2\theta \cdot \frac{\Delta\beta[i-1]}{\beta[i-1]} \cdot \lambda[i-1] \\
& + \frac{4\beta[i]^2}{\alpha[i]^3} \cdot \sin^2\theta \cdot \frac{\Delta\beta[i]}{\beta[i]} \cdot \lambda[i] \\
& + \frac{2\beta[i-1]^2}{\alpha[i-1]^3} \cdot \sin^2\theta \cdot \frac{\Delta\rho[i-1]}{\rho[i-1]} \cdot \lambda[i-1] \\
& + \frac{2\beta[i]^2}{\alpha[i]^3} \cdot \sin^2\theta \cdot \frac{\Delta\rho[i]}{\rho[i]} \cdot \lambda[i] \Bigg\}
\end{aligned} \tag{2.23}$$

$$\begin{aligned}
\frac{\partial\mathcal{L}}{\partial V_S[i]} = \int_\theta d\theta \Bigg\{ & - \frac{2\Delta\beta[i-1]}{\alpha[i-1]^2} \cdot \sin^2\theta \cdot \lambda[i-1] \\
& - \frac{2\Delta\beta[i]}{\alpha[i]^2} \cdot \sin^2\theta \cdot \lambda[i] \\
& - \frac{4\beta[i-1]}{\alpha[i-1]^2} \cdot \sin^2\theta \cdot \lambda[i-1] \\
& + \frac{4\beta[i]}{\alpha[i]^2} \cdot \sin^2\theta \cdot \lambda[i] \\
& - \frac{2\beta[i-1]}{\alpha[i-1]^2} \cdot \sin^2\theta \cdot \frac{\Delta\rho[i-1]}{\rho[i-1]} \cdot \lambda[i-1] \\
& - \frac{2\beta[i]}{\alpha[i]^2} \cdot \sin^2\theta \cdot \frac{\Delta\rho[i]}{\rho[i]} \cdot \lambda[i] \Bigg\}
\end{aligned} \tag{2.24}$$

and

$$\frac{\partial \mathcal{L}}{\partial \rho[i]} = \int_{\theta} d\theta \left\{ C[i-1] \cdot \left(\frac{1}{\rho[i-1]} \right) \cdot \lambda[i-1] - C[i] \cdot \left(\frac{1}{\rho[i]} \right) \cdot \lambda[i] \right. \\ \left. -C[i-1] \cdot \left(\frac{\Delta\rho[i-1]}{\rho[i-1]^2} \right) \cdot \lambda[i-1] - C[i] \cdot \left(\frac{\Delta\rho[i]}{\rho[i]} \right) \cdot \lambda[i] \right\} \tag{2.25}$$

When equations 2.21 and 2.22 are satisfied, it means the derivatives of the extended objective function with respect to R_{PP} and state variable (λ) are zero. Then, the gradients of $\mathcal{L}$ and J with reference to the model properties coincide: $\frac{\partial \mathcal{L}}{\partial V_P[i]} = \frac{\partial J}{\partial V_P[i]}$, $\frac{\partial \mathcal{L}}{\partial V_S[i]} = \frac{\partial J}{\partial V_S[i]}$, and $\frac{\partial \mathcal{L}}{\partial \rho[i]} = \frac{\partial J}{\partial \rho[i]}$, and the Lagrangian can be used to find the derivative of J and obtain the gradient equations for $V_P[i]$, $V_S[i]$, and $\rho[i]$. The state variable λ can be computed as:

$$\lambda[i] = -2W[i] * (d[i] - W[i] * R_{PP}[i]) \tag{2.26}$$

2.10 Appendix B: Amplitude scaling factor

To compare the finite difference model and the convolution model, we define an amplitude scaling factor to compensate for the effect of offset-dependent geometrical spreading. If k is the scaling factor, the least-square equation can be written as:

$$\mathbf{J} = \frac{1}{2} \parallel \mathrm{d_C} - k \cdot \mathrm{d_{FD}} \parallel_t^2 \tag{2.27}$$

where d_C and d_{FD} stand for the convolution and the finite difference models computed for all the data for any travel time t. The derivative of the discretized form ($t = 1, 2, 3, ...$) of the Equation 2.27 with respect to the scaling factor k the set equal to 0.

$$\frac{\mathrm{d}\mathbf{J}}{\mathrm{dk}} = -\sum_t ((\mathrm{d_C} - k \cdot \mathrm{d_{FD}}) \cdot \mathrm{d_{FD}}) = 0 \tag{2.28}$$

which leads to:

$$-\sum_t \mathrm{d_C} \cdot \mathrm{d_{FD}} + k \cdot \sum_t {\mathrm{d_{FD}}}^2 = 0 \tag{2.29}$$

The scaling factor for the geometrical spreading can be then defined mathematically as:

$$k = \frac{\sum_t \mathrm{d_C} \cdot \mathrm{d_{FD}}}{\sum_t {\mathrm{d_{FD}}}^2} \tag{2.30}$$

The geometrical spreading scaling factor is plotted as a function of incident angles in Fig. 2.18. The comparison of the derived least-square based k is made with Ursin's method (Ursin 1990) and the results displayed in Fig. 2.18 show the accuracy of the derived scaling factor up to the incident angle of almost 20°.

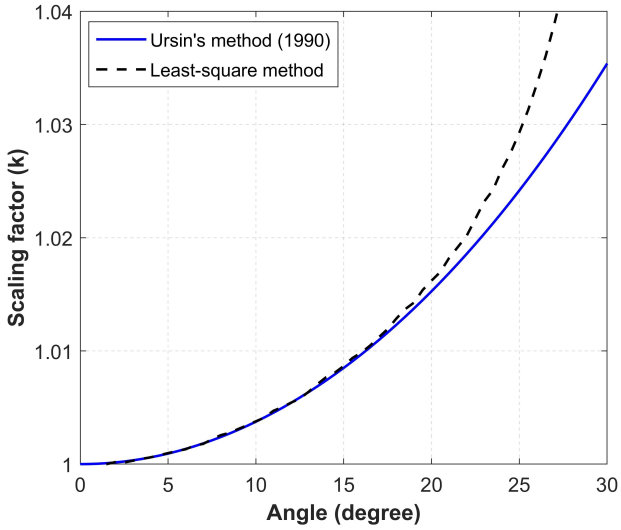

Figure 2.18: The comparison between amplitude correction scaling factors to compensate for the effects of offset-dependent geometrical spreading. The least-square derived scaling factor shows a good correlation with Ursin's method (Ursin 1990) up to incident angle 20°.

2.11 Extended discussion

The uncertainty in the inverted models of the elastic properties can be described as a function of initial model variability. For example, a set of 100 initial models has been generated by using a Monte Carlo simulation and then the inversion process is applied to every initial model to get the distribution of the inverted properties. The probability density estimates for the 100 initial models of each P- and S- wave velocities and density are plotted in Figure 2.19. These initial models are simulated by using a probabilistic method that follows the spatial correlation model (Buland and Omre 2003a; Grana et al. 2021).

The probability density estimates for the posterior solution of the model properties are shown in Figure 2.20. The inverted models are computed with the forward models having a signal-to-noise ratio of 20. Despite the relatively high variability in the initial guesses, the uncertainty in the inverted properties is reasonably small. The probability density estimates of the inverted models are in close agreement with the true models (shown by solid black lines). This further describes the stability and accuracy of the proposed inversion method.

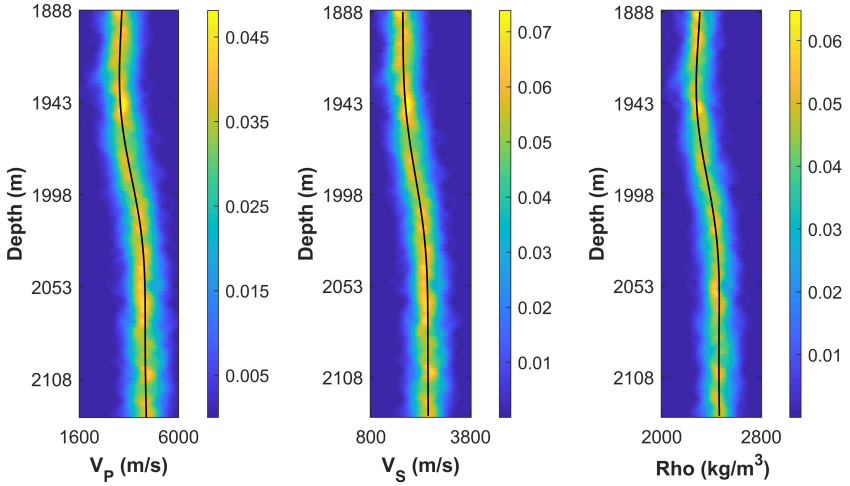

Figure 2.19: The initial guess for the P- wave velocity (V_P), S- wave velocity (V_S), and density. The solid black lines represent the mean of the initial models.

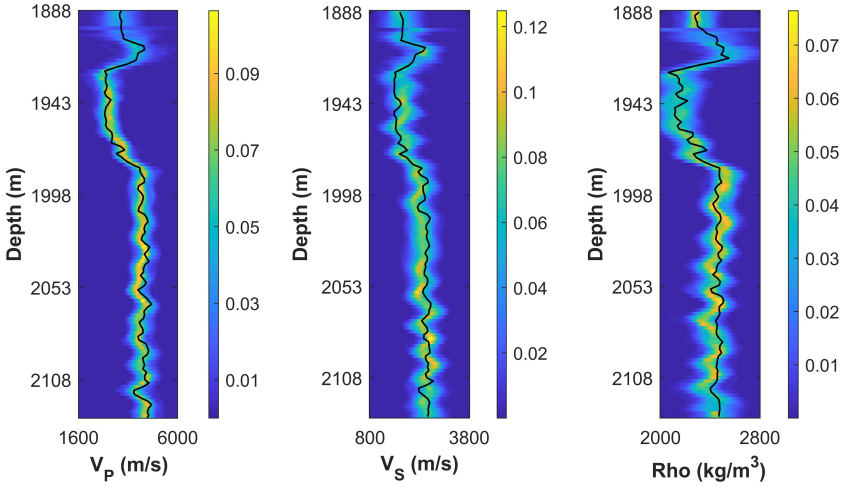

Figure 2.20: The inverted models for the P- wave velocity (V_P), S- wave velocity (V_S), and density. The solid black lines describe the reference or true model.

Chapter 3

Constrained non-linear AVO inversion for dynamic reservoir changes estimation from time-lapse seismic data

By:
Ahmed, Nisar[1]
Weibull, Wiktor Waldemar[1]
Grana, Dario[2]
Bhakta, Tuhin[3]

[1]Department of Energy Resources, 4021 Stavanger, University of Stavanger, Norway
[2]Department of Geology and Geophysics, School of Energy Resources, University of Wyoming, Laramie, Wyoming 82071, United States
[3]NORCE Norwegian Research Centre, and Equinor ASA, Bergen, Norway

Modified/revised version is printed in:
Geophysics, 89:1, pp 1-65, (2024)
https://doi.org/10.1190/geo2022-0750.1

3.1 Summary

We propose a novel elastic AVO inversion process to estimate the fluid saturation and effective pressure or variations in these properties from the time-lapse seismic dataset. These changes occur in oil and gas reservoirs caused by fluid injection or hydrocarbon production that leads to changes in the elastic wave properties, reflectivity, and seismic response. The proposed method is based on a seismic forward model that consists of a linearized AVO equation and a rock physics model. The AVO equation links the elastic wave properties to reflection amplitudes, whereas the rock physics model maps the saturation and pressure into seismic velocities and density. The inversion approach relies on the gradient descent technique to estimate the unknown variables by searching for the minimum of the least-square misfit between observed and modeled data. The first-order gradient of the least-square data misfit function with respect to the model properties is derived by using the adjoint-state method and the chain rule to compute the gradient equations of the seismic response with respect to effective pressure and water saturation. The optimization method used to minimize the misfit function and obtain the best optimal solution is the limited-memory quasi-Newton algorithm. This inversion process allows incorporating the prior constraints and achieving the optimal regularization weight of the measured variables to limit the solution space of the ill-posed inversion problem. The application of the developed workflow on 1D synthetic and real well log data from the Edvard Grieg oil field simulating various saturation-pressure conditions during production demonstrates the validity of the approach with different noise levels. The inversion is then applied to a 2D synthetic dataset modeled from the reservoir model of the Smeaheia field, a potential site for a large-scale offshore CO_2 storage field located in the North Sea. Our results illustrate that the proposed inversion method efficiently estimates reservoir saturation and pressure variations with accurate convergence and reliable robustness.

3.2 Introduction

Time-lapse seismic AVO data are frequently used to monitor the variations in oil and gas reservoirs during hydrocarbon production and to optimize the fluid injection schedule for enhanced oil recovery. Reservoir depletion and/or fluid injection in the reservoir cause variations in the effective and pore (fluid) pressure and fluid (water and hydrocarbon) saturation. These changes might have a considerable effect on elastic and seismic properties (Mavko et al. 2020); hence, geophysical data can be applied to predict the dynamic changes during production (Holt et al. 2005; LI et al. 2005; Tsuneyama and Mavko 2007). The difference between pre-stack seismic data acquired at two different times, for example before and during production, has been successfully utilized to map the changes in reservoir dynamics properties (Bhakta and Landrø 2014; Buland and El Ouair 2006; Dinh and Van der Baan 2019; Landrø 2001; Maharramov et al. 2016; Trani et al. 2011). This information is crucial for field development as dynamic changes are used to determine optimal drainage patterns and understand geomechanical processes.

The prediction of pressure and saturation properties from the 4D pre-stack seismic

gathers is formulated as an inverse problem. By combining seismic partial stacks and rock physics theory, Landrø (2001) introduces an efficient method to estimate the pressure and saturation changes from the pre-stack monitoring data. This approach is on the basis of linear and quadratic approximations of the reflectivity coefficients as a function of pore pressure and water saturation changes have been then extended to several methods for time-lapse seismic inversion (Bhakta 2018; Bhakta and Landrø 2014; Dadashpour et al. 2008; Landrø et al. 2003; Meadows 2001). Probabilistic versions of this approach have also been developed to quantify the model uncertainty (Davolio et al. 2012; Emerick 2014; Lang and Grana 2019; Veire et al. 2006). For example, Veire et al. (2006) formulate the saturation-pressure estimation problem in the Bayesian framework, and rock physics fluid substitution models are implemented to build a prior stochastic model. Then, Lang and Grana (2019), modify Landrø's approach to accounting for the spatial variability of porosity and initial reservoir conditions of pressure and saturation. Landrø's method and its extensions have been often adopted as they provide a direct link between seismic amplitudes and reservoir property based on linear and quadratic approximations (Côrte et al. 2023). These formulations might fail when the combined effect of pressure and saturation on elastic properties is nonlinear and cannot be approximated by simple polynomial functions. In these cases, two-step inversion approaches of time-lapse seismic data have been proposed by combining seismic inversion in the elastic domain with rock physics inversion in the reservoir property domain (Buland and El Ouair 2006; Côrte et al. 2023; Dupuy et al. 2021a; Dupuy et al. 2021b; Forberg et al. 2021; Grana and Mukerji 2015).

In the present research work, we introduce a constrained non-linear algorithm for the amplitude versus offset (AVO) inversion on the basis of the linearized Aki and Richards equation (Aki and Richards 1980) to estimate fluid saturation and pressure changes from 4D pre-stack seismic gathers. The rock physics model is assumed to be known and it includes multiple poroelastic relations such as Gassmann's equation, Hill's average, MacBeth-Grana's equation (Gassmann 1951; Grana 2016; Hill 1963; MacBeth 2004) that are used to link the dynamic reservoir variables (fluid saturation and effective stress) to the changes in elastic parameters. The rock physics models can account for multiple fluid mixing scenarios such as uniform and patchy saturation (Ahmed et al. 2016). In the inversion approach, we apply the gradient descent-based optimization algorithm to minimize the L2-norm misfit function. The gradient of the least-square misfit function with respect to saturation and pressure variables is computed using the adjoint-state numerical method (Ahmed et al. 2023; Plessix 2006). Adjoint methods are already being used in numerous geophysical publications (Ahmed et al. 2022; Ahmed et al. 2023; Biondi et al. 2021; Hu et al. 2021; Ravasi and Vasconcelos 2021; Wang et al. 2021a). In the proposed approach, the adjoint-state method is first applied to derive the gradient equations with respect to P- and S- wave velocities and density by solving the AVO equation as shown in (Ahmed et al. 2022); then, the chain rule for the partial derivatives is used to calculate the adjoint-based gradient expressions for the water saturation and effective pressure. The main advantage of the adjoint method is that it is unrestrained to the number of model variables and consequently provides a more efficient and faster way to calculate the gradient compared to traditional approaches such as finite difference or Fréchet derivative. To minimize the misfit function and iteratively obtain the best optimal solution, we implement a non-linear optimization based on

the limited-memory BFGS algorithm (Liu and Nocedal 1989; Nocedal 1980). In the proposed implementation, Tikhonov regularization weights are applied to make the inverse solution more stable for noisy datasets. The main contribution of the developed technique is the derivation and application of the adjoint-state solution for the gradient of the least-square misfit function with respect to saturation and pressure based on the AVO reflectivity equation and rock physics model. We test the method on two different scenarios. The first example is based on the well-log data of the Edvard Grieg oil field, North Sea, where different saturation-pressure combinations with various noise levels are evaluated. The second example is based on a 2D line extracted from the 3D reservoir model of the Smeaheia field and a synthetic time-lapse seismic dataset mimicking water saturation and pressure variations due to CO_2 injection.

3.3 Theory and method

In this section, we first present the elastic forward model combining AVO and rock physics relations and then describe the inversion scheme for the prediction of changes in unknown model variables (saturation and effective pressure) based on the adjoint-state solution of the least-square misfit function with respect to the model variables.

3.3.1 Seismic forward model

The seismic forward model is approximated by a known convolutional method based on the weak contrast formulation of the PP reflectivity and, in this implementation, is parametrized based on elastic wave velocities (P- and S-wave) and effective density. According to this formulation, the seismic response $d(t,\,\theta)$ is a function of two-way travel time (t) and angle of incident (θ) and it is calculated using the convolutional operator:

$$d(t,\,\theta) = W(t) * R_{PP}(t,\,\theta|m) \tag{3.1}$$

where $W(t)$ denotes the source wavelet and R_{PP} indicates the reflection amplitudes. R_{PP} are modeled using the linearized Aki and Richards AVO approximation:

$$R_{PP}(t,\,\theta) = A(\theta)\,\frac{\Delta\alpha(t)}{\alpha(t)} + B(t,\,\theta)\,\frac{\Delta\beta(t)}{\beta(t)} + C(t,\,\theta)\,\frac{\Delta\rho(t)}{\rho(t)} \tag{3.2}$$

whereas,

$$A = \left[\frac{1}{2}\left(1+\tan^2\theta\right)\right], \qquad B = \left[-\frac{4\beta^2}{\alpha^2}\sin^2\theta\right], \qquad C = \frac{1}{2}\left[1-\frac{4\beta^2}{\alpha^2}\sin^2\theta\right]$$

while $\Delta\rho$, $\Delta\alpha$ and $\Delta\beta$ being the contrast between seismic properties and α, β and ρ being the averages values across the seismic reflection boundary e.g., $\Delta\rho = \rho_2 - \rho_1$, $\Delta\alpha = V_{P2} - V_{P1}$, $\Delta\beta = V_{S2} - V_{S1}$, $\rho = (\rho_2+\rho_1)/2$, $\alpha = (V_{P2}+V_{P1})/2$, $\Delta\beta = (V_{S2}+V_{S1})/2$.

Elastic variables e.g., elastic wave (P- and S-wave) velocities (V_P and V_S) and effective density (ρ) rely on the litho-fluid properties through the fluid-saturated rock bulk and shear moduli K_{sat} and μ_d (Ahmad et al. 2019; Mavko et al. 2020). To link

elastic parameters to the pore fluids and rock properties, we introduce rock physics modeling. For illustration purposes, we assume two fluid phases, namely oil, and water. We also assume that the effective pressure is obtained by subtracting the pore pressure from the overburden pressure (Hussain and Ahmed 2018). Hence, the variables of interest are effective pressure (P_e) and water saturation (S_w). The rock physics theory then comprises several relations, to describe the saturation and pressure effects.

Gassmann (1951) equation describes the pore fluids effect on the saturated rock bulk modulus K_{sat}:

$$K_{sat} = K_d + \beta_c^2 M \tag{3.3}$$

where the Biot coefficient (β_c) and M are:

$$\beta_c = 1 - \frac{K_d}{K_m}, \quad M = \left[\frac{\beta_c - \phi}{K_m} + \frac{\phi}{K_f} \right]^{-1}$$

In this formulation, ϕ denotes reservoir effective porosity, K_m and K_d are the mineral and dry rock bulk moduli respectively, and K_f represents the fluid bulk modulus. In our formulation, the bulk modulus of the rock-forming minerals (K_m) is calculated by using the Voigt-Ruess-Hill average (Mavko et al. 2020). The bulk modulus of the pore fluids (K_f) is calculated using Wood's average equation:

$$K_f = \left[\frac{S_w}{K_w} + \frac{1 - S_w}{K_o} \right]^{-1} \tag{3.4}$$

assuming two reservoir fluids, namely water, and oil, where K_w and K_o are the fluid moduli of water and oil respectively. The Reuss formula holds only if the fluid phases are uniformly distributed within the pore space. Alternatively, the rock physics model for patchy saturation is described in the Appendix A.

The effective pressure effect is modeled using the modified MacBeth's formulas (Grana 2016; MacBeth 2004) for bulk and shear moduli of dry rock (K_d and μ_d), as:

$$K_d = \frac{K_m \left(1 - \frac{\phi}{\phi_c}\right)}{1 + E_k e^{-P_e/P_k}}, \qquad \mu_d = \frac{\mu_m \left(1 - \frac{\phi}{\phi_c}\right)}{1 + E_\mu e^{-P_e/P_\mu}} \tag{3.5}$$

where ϕ_c denotes the critical porosity, μ_m describes the shear modulus of the rock matrix, P_k, P_μ represent the fracturing pressure, and E_k, E_μ represent the closing rate of the pores. These parameters are generally empirically estimated case by case, for example, due to the inaccessibility of experimental data at the well location, these parameters are optimized by defining a misfit function (J) representing the distance between the rock physics model-based P and S wave velocities and the reference well-logs velocities as:

$$\min J(E_k, E_\mu) = \min \frac{1}{2} \parallel V_{P-\mathrm{RPM}}(E_k, E_\mu) - V_{P-\mathrm{well}} \parallel_t^2 \tag{3.6}$$

$$\min J(E_\mu) = \min \frac{1}{2} \parallel V_{S-\mathrm{RPM}}(E_\mu) - V_{S-\mathrm{well}} \parallel_t^2 \tag{3.7}$$

here, subscripts RPM and well indicate rock physics model and well logs-based velocities respectively.

We then applied the unconstrained minimization to the misfit function by using the quasi-Newton method to obtain optimized close rates (E_{k-opt} and $E_{\mu-opt}$). The gradients of the misfit function with respect to E_k and E_μ are calculated by using the finite difference method. The main limitation of this approach is that these parameters might depend on the rock properties such as porosity and lithology as shown (Grana 2016; Lang and Grana 2019) and may spatially vary. Indeed, the parameters of the exponential function should depend on porosity and lithology but their calibration is difficult when these parameters are unknown; hence, we used the approximation in (Grana 2016) where the asymptotic value of the exponential function, for increasing pressure values, depends on porosity.

Elastic wave velocities are then calculated from the moduli and effective reservoir density as:

$$V_P = \left[\frac{K_{sat} + 4/3\mu_d}{\rho}\right]^{1/2}, \quad V_S = \left[\frac{\mu_d}{\rho}\right]^{1/2} \tag{3.8}$$

$$\rho = \rho_m(1-\phi) + \phi\,\rho_w\,S_w + \phi\,\rho_o\,(1-S_w) \tag{3.9}$$

where ρ_m, ρ_w, and ρ_o indicate the density of the minerals, water, and oil respectively.

3.3.2 AVO inversion and adjoint-state solution

Based on the previously described seismic and rock physics models, we formulate an inversion framework where the unknown model properties are predicted by minimizing a misfit function. We define the L2-norm least-squares misfit function for the model variables $m = [S_w(t), P_e(t)]$ as:

$$J(m) = \frac{1}{2} \parallel d - f(m) \parallel^2 \tag{3.10}$$

whereas d represents the real seismic AVO data and $f(m)$ is the previously described forward model. The minimization is performed using the gradient descent optimization technique which requires the calculation of the gradient (∇J) of the misfit function with respect to the model properties:

$$\nabla J = \left[\frac{\partial J}{\partial S_w}, \frac{\partial J}{\partial P_e}\right] \tag{3.11}$$

The partial derivatives of the multivariate misfit function J given by equation 3.11 with respect to $m = [S_w(t), P_e(t)]$ are calculated in the discretized domain for a sequence of interfaces $i = 1, ..., n$ and they are equal to:

$$\frac{\partial J}{\partial S_w[i]} = -\Big[d - f(m)\Big] \cdot \frac{\partial f}{\partial S_w[i]}, \qquad \frac{\partial J}{\partial P_e[i]} = -\Big[d - f(m)\Big] \cdot \frac{\partial f}{\partial P_e[i]} \tag{3.12}$$

The terms $(\partial f / \partial m[i])$ represent the Jacobian matrix and are defined as the matrix of all its first-order partial derivatives which can be expensive to calculate. The gradient of a function, when it depends on model parameters through state variables, can be

computed without the Jacobian matrix by using the adjoint-state method. Therefore to derive the gradient of the multivariate misfit function, the adjoint-state method is implemented here through the augmented Lagrangian of the extended misfit function $\mathcal{L}$ with the additional adjoint-state variable λ as:

$$\mathcal{L}(V_P, V_S, \rho, R_{PP}, \lambda) = \sum_i \int_\theta d\theta \left[d[i] - W[i] * R_{PP}[i] \right]^2 + \sum_i \int_\theta d\theta \left[R_{PP}[i] - A[i] \cdot \frac{\Delta\alpha}{\alpha} - B[i] \cdot \frac{\Delta\beta}{\beta} - C[i] \cdot \frac{\Delta\rho}{\rho} \right] \lambda_{[i]} \quad (3.13)$$

From the above equation, the extended objective function $(\mathcal{L})$ is rescripted as:

$$\mathcal{L} = J + C * \lambda \quad (3.14)$$

here the constraint C is defined such that the Aki and Richards equation is satisfied:

$$\left[R_{PP}[i] - A[i] \cdot \frac{\Delta\alpha}{\alpha} - B[i] \cdot \frac{\Delta\beta}{\beta} - C[i] \cdot \frac{\Delta\rho}{\rho} \right] = 0 \quad (3.15)$$

The gradient of the Lagrangian $(\mathcal{L})$ equals the gradient of the misfit function $\boldsymbol{J}$ as long as the following system holds for all R_{PP} and all λ:

$$\frac{\partial \mathcal{L}}{\partial R_{PP}} = 0, \qquad \frac{\partial \mathcal{L}}{\partial \lambda} = 0 \quad (3.16)$$

The gradients of the extended misfit equation with respect to V_P, V_S and ρ are obtained by solving equation 3.13 as shown in Ahmed et al. (2022) as:

$$\begin{aligned} \frac{\partial \mathcal{L}}{\partial V_P[i]} = \int_\theta d\theta \Bigg\{ & \frac{A}{\alpha[i-1]} \cdot \lambda[i-1] - \frac{A}{\alpha[i]} \cdot \lambda[i] \\ & - \frac{A\Delta\alpha[i-1]}{2\alpha[i-1]^2} \cdot \lambda[i-1] - \frac{A\Delta\alpha[i]}{2\alpha[i]^2} \cdot \lambda[i] \\ & + \frac{4\beta[i-1]^2}{\alpha[i-1]^3} \cdot \sin^2\theta \cdot \frac{\Delta\beta[i-1]}{\beta[i-1]} \cdot \lambda[i-1] \\ & + \frac{4\beta[i]^2}{\alpha[i]^3} \cdot \sin^2\theta \cdot \frac{\Delta\beta[i]}{\beta[i]} \cdot \lambda[i] \\ & + \frac{2\beta[i-1]^2}{\alpha[i-1]^3} \cdot \sin^2\theta \cdot \frac{\Delta\rho[i-1]}{\rho[i-1]} \cdot \lambda[i-1] \\ & + \frac{2\beta[i]^2}{\alpha[i]^3} \cdot \sin^2\theta \cdot \frac{\Delta\rho[i]}{\rho[i]} \cdot \lambda[i] \Bigg\} \end{aligned} \quad (3.17)$$

$$\frac{\partial \mathcal{L}}{\partial V_S[i]} = \int_\theta d\theta \left\{ -\frac{2\Delta\beta[i-1]}{\alpha[i-1]^2} \cdot \sin^2\theta \cdot \lambda[i-1] \right.$$
$$- \frac{2\Delta\beta[i]}{\alpha[i]^2} \cdot \sin^2\theta \cdot \lambda[i]$$
$$- \frac{4\beta[i-1]}{\alpha[i-1]^2} \cdot \sin^2\theta \cdot \lambda[i-1]$$
$$+ \frac{4\beta[i]}{\alpha[i]^2} \cdot \sin^2\theta \cdot \lambda[i]$$
$$- \frac{2\beta[i-1]}{\alpha[i-1]^2} \cdot \sin^2\theta \cdot \frac{\Delta\rho[i-1]}{\rho[i-1]} \cdot \lambda[i-1]$$
$$\left. - \frac{2\beta[i]}{\alpha[i]^2} \cdot \sin^2\theta \cdot \frac{\Delta\rho[i]}{\rho[i]} \cdot \lambda[i] \right\} \quad (3.18)$$

and

$$\frac{\partial \mathcal{L}}{\partial \rho[i]} = \int_\theta d\theta \left\{ C[i-1] \cdot \left(\frac{1}{\rho[i-1]} \right) \cdot \lambda[i-1] - C[i] \cdot \left(\frac{1}{\rho[i]} \right) \cdot \lambda[i] \right.$$
$$\left. - C[i-1] \cdot \left(\frac{\Delta\rho[i-1]}{\rho[i-1]^2} \right) \cdot \lambda[i-1] - C[i] \cdot \left(\frac{\Delta\rho[i]}{\rho[i]} \right) \cdot \lambda[i] \right\} \quad (3.19)$$

The partial derivatives of the extended misfit function with respect to R_{PP} and λ are 0 when equation 3.16 is satisfied. Then the gradients of the extended and misfit functions are equal:

$$\frac{\partial \mathcal{L}}{\partial V_P[i]} = \frac{\partial J}{\partial V_P[i]}, \qquad \frac{\partial \mathcal{L}}{\partial V_S[i]} = \frac{\partial J}{\partial V_S[i]}, \qquad \frac{\partial \mathcal{L}}{\partial \rho[i]} = \frac{\partial J}{\partial \rho[i]} \quad (3.20)$$

and state variable (λ) is calculated by equation $\lambda[i] = -2W[i] * (d[i] - W[i] * R_{PP}[i])$.

The derivatives of the data misfit function with respect to S_w and P_e are computed by using the multivariable chain rule of the partial derivatives. The expressions for these gradients are:

$$\frac{\partial J}{\partial S_w[i]} = \frac{\partial J}{\partial V_P[i]} \cdot \frac{\partial V_P[i]}{\partial S_w[i]} + \frac{\partial J}{\partial V_S[i]} \cdot \frac{\partial V_S[i]}{\partial S_w[i]} + \frac{\partial J}{\partial \rho[i]} \cdot \frac{\partial \rho[i]}{\partial S_w[i]} \quad (3.21)$$

and

$$\frac{\partial J}{\partial P_e[i]} = \frac{\partial J}{\partial V_P[i]} \cdot \frac{\partial V_P[i]}{\partial P_e[i]} + \frac{\partial J}{\partial V_S[i]} \cdot \frac{\partial V_S[i]}{\partial P_e[i]} \quad (3.22)$$

where the partial derivatives of elastic properties (V_P, V_S, ρ) with respect to water saturation and effective pressure are given by:

$$\frac{\partial V_P[i]}{\partial S_w[i]} = \frac{\partial V_P[i]}{\partial \rho[i]} \cdot \frac{\partial \rho[i]}{\partial S_w[i]} + \frac{\partial V_P[i]}{\partial K_{sat}[i]} \cdot \frac{\partial K_{sat}[i]}{\partial K_f[i]} \cdot \frac{\partial K_f[i]}{\partial S_w[i]} \quad (3.23)$$

$$\frac{\partial V_P}{\partial \rho} \cdot \frac{\partial \rho}{\partial S_w} = -\frac{1}{2\rho^{3/2}} \left(K_{sat} + \frac{4}{3}\,\mu_d \right)^{1/2} \cdot \phi\,(\rho_w - \rho_o) \tag{3.24}$$

$$\frac{\partial V_P}{\partial K_{sat}} = \frac{1}{2\sqrt{\rho}} \left(K_{sat} + \frac{4}{3}\,\mu_d \right)^{-1/2} \tag{3.25}$$

$$\frac{\partial K_{sat}}{\partial K_f} \cdot \frac{\partial K_f}{\partial S_w} = \frac{\beta_c^2\,\phi\,K_m^2}{(K_f\,(\beta_c - \phi) + \phi\,K_m)^2} \cdot \frac{-K_w\,K_o\,(K_o - K_w)}{(K_o\,S_w + K_w\,(1 - S_w))^2} \tag{3.26}$$

$$\frac{\partial V_S[i]}{\partial S_w[i]} = \frac{\partial V_S[i]}{\partial \rho[i]} \cdot \frac{\partial \rho[i]}{\partial S_w[i]} \tag{3.27}$$

$$\frac{\partial V_S}{\partial \rho} = -\frac{1}{2}\frac{\sqrt{\mu_d}}{\rho^{3/2}}, \qquad \frac{\partial \rho}{\partial S_w} = \phi\,(\rho_w - \rho_o) \tag{3.28}$$

and

$$\frac{\partial V_P[i]}{\partial P_e[i]} = \frac{\partial V_P[i]}{\partial K_{sat}[i]} \cdot \frac{\partial K_{sat}[i]}{\partial K_d[i]} \cdot \frac{\partial K_d[i]}{\partial P_e[i]} + \frac{\partial V_P[i]}{\partial \mu_d[i]} \cdot \frac{\partial \mu_d[i]}{\partial P_e[i]} \tag{3.29}$$

$$\frac{\partial V_S[i]}{\partial P_e[i]} = \frac{\partial V_S[i]}{\partial \mu_d[i]} \cdot \frac{\partial \mu_d[i]}{\partial P_e[i]} \tag{3.30}$$

$$\frac{\partial V_P}{\partial K_{sat}} = \frac{1}{2\sqrt{\rho}} \left(K_{sat} + \frac{4}{3}\mu_d \right)^{-1/2} \tag{3.31}$$

$$\frac{\partial K_{sat}}{\partial K_d} = \left(1 - \frac{M\beta_c}{K_m} \right)^2 \tag{3.32}$$

$$\frac{\partial K_d}{\partial P_e} = K_m \left(1 - \frac{\phi}{\phi_c} \right) \left[\frac{E_k e^{-P_e/P_k}}{P_k \left(1 + E_k e^{-P_e/P_k} \right)^2} \right] \tag{3.33}$$

$$\frac{\partial V_P}{\partial \mu_d} = \frac{2}{3\sqrt{\rho}} \left(K_{sat} + \frac{4}{3}\mu_d \right)^{-1/2} \tag{3.34}$$

$$\frac{\partial \mu_d}{\partial P_e} = \mu_m \left(1 - \frac{\phi}{\phi_c} \right) \left[\frac{E_\mu e^{-P_e/P_\mu}}{P_\mu \left(1 + E_\mu e^{-P_e/P_\mu} \right)^2} \right] \tag{3.35}$$

$$\frac{\partial V_S}{\partial \mu_d} = \frac{1}{2\sqrt{\rho}} \frac{1}{\sqrt{\mu_d}} \tag{3.36}$$

We assume that the changes in reservoir porosity caused by pore pressure changes are usually minor and therefore the effect of pore pressure changes on the density changes is negligible as considered by several authors (Bhakta 2018; Landrø 2001; Trani et al. 2011). The gradient solution for the patchy saturation case is given in the Appendix A.

To constrain the model parameters between physical bounds, we use the logistic function to map P_e and S_w into the optimization variables m_{P_e} and m_{S_w}. For pressure P_e, we define the forward mapping, inverse mapping, and derivative chain rule mapping between the optimization variable m_{P_e} and the forward modeling variable P_e:

$$m_{P_e} = \frac{1}{k_{P_e}} \ln\left(\frac{P_e - P_{emin}}{P_{emax} - P_e}\right) \tag{3.37}$$

$$P_e = P_{emin} + \frac{P_{emax} - P_{emin}}{1 + \exp\left(-k_{P_e} m_{P_e}\right)} \tag{3.38}$$

$$\frac{\partial J}{\partial m_{P_e}} = \frac{\partial J}{\partial P_e} k_{P_e} (P_{emax} - P_{emin}) \frac{\exp\left(-k_{P_e} * m_{P_e}\right)}{\left(1 + \exp\left(-k_{P_e} m_{P_e}\right)\right)^2}. \tag{3.39}$$

In equations 3.37 – 3.39, P_{emin} and P_{emax} are the lower and upper bounds respectively, while k_{P_e} is a scaling variable that controls the relative contribution of P_e in the gradient descent direction. Similar equations are derived for saturation S_w, where the minimum and maximum saturation are set to 0 and 1.

3.3.3 Gradient-based optimization

Based on the above-computed gradients of the misfit function, a non-linear optimization algorithm is applied. Several optimization algorithms have been introduced and applied to solving seismic inverse problems. We adopt the limited-memory BFGS technique that implicitly approximates the inverse of the Hessian matrix, reducing the computational and storage costs. In L-BFGS, the model m at each iteration of the AVO inversion system is updated as:

$$m_{k+1} = m_k - \alpha_k H_k \nabla J, \qquad k = 0, 1, 2, 3, ..., \tag{3.40}$$

whereas m_k symbolizes the model vector of the updating variables at iteration k, α_k is the step length or size computed by a line search approach using Wolfe conditions (Nocedal and Wright 2006), ∇J represents the first-order gradient of the least-square misfit function J and H_k corresponds the inverse of the Hessian matrix.

In the L-BFGS method, the step length or the line search technique evaluates how far the optimization algorithm moves in every iteration. The most widespread step length conditions are the Wolfe conditions comprised of two criteria, such as Armijo and curvature (which includes Wolfe, and strong Wolfe) conditions. The Armijo condition is the most widely used line search method that ensures that the function decreases sufficiently through the iterations. The Wolfe condition is a line search method that adds a curvature condition to the Armijo condition. The strong Wolfe condition is even a strict version of the Wolfe condition that involves an additional curvature condition. In this work, we adopt the Wolfe conditions, where the step size satisfies the following three inequalities:

$$J(m_k + \alpha_k d_k) \leq J(m_k) + c_1 \alpha_k d_k^T \nabla J(m_k) \tag{3.41}$$

$$-d_k^T \nabla J(m_k + \alpha_k d_k) \leq -c_2 d_k^T \nabla J(m_k) \tag{3.42}$$

and

$$|d_k^T \nabla J(m_k + \alpha_k d_k)| \leq c_2 |d_k^T \nabla J(m_k)| \tag{3.43}$$

Equations 3.41 - 3.43 represent the Armijo, Wolfe, and strong Wolfe conditions respectively. These conditions (equations 3.41 and 3.43) guarantee that the step provides upper and lower bounds on the acceptable step sizes. Whereas c_1 and c_2 are user-defined thresholds for these inequalities, for example $c_1 = 10^{-4}$ and $c_2 = 0.9$ in our application for the quasi-Newton method (Nocedal and Wright 2006), whereas d_k represents the descent direction $(-H_k \nabla J)$.

The Tikhonov regularization is introduced to make the solution more stable in case of noisy data. The regularization weights are chosen based on a trial-and-error approach. Because saturation is bounded between 0 and 1 and pressure has a limited variation, due to engineering constraints, we impose minimum and maximum values to constrain the inversion in the physical range of the solution.

The non-linear inversion algorithm is summarized in the following steps:

- Start with the initial guess for the model variables like initial S_w and P_e.
- Map the model variables S_w and P_e to optimisation variables m_{S_w}, and m_{P_e}.
- Create a function that computes the misfit function and its gradients with respect to the optimization variables. The misfit function is calculated by using forward modeling through the current set of model variables while the gradient is computed by using the adjoint-state equations and associated derivative chain rules.
- Compute the regularization term and its gradients and add to the data misfit function and data misfit gradients, respectively.
- Minimize the misfit function using the minimization algorithm L-BFGS. As a part of this step, the functions in steps 3 and 4 are called many times to compute new values for the objective function and gradients during both line search and update steps (equation 3.40).

The loop is repeated time and again until the convergence criteria are met or the predefined number of iterations is achieved. At this point, the optimized model variables ($m_{S_w}^{opt}$ and $m_{P_e}^{opt}$) are the outputs of the inversion algorithms as shown in Figure 3.1. The inversion scheme following the above steps is described by a concise flowchart in Figure 3.1.

3.4 Applications

We apply the adjoint-state analytical solution-based non-linear seismic AVO inversion scheme to several examples mimicking reservoir production scenarios in different noise level conditions. The numerical tests are based on real well logs data from the North Sea Edvard Grieg field. The clastic reservoir includes a 50 m oil-saturated interval in the

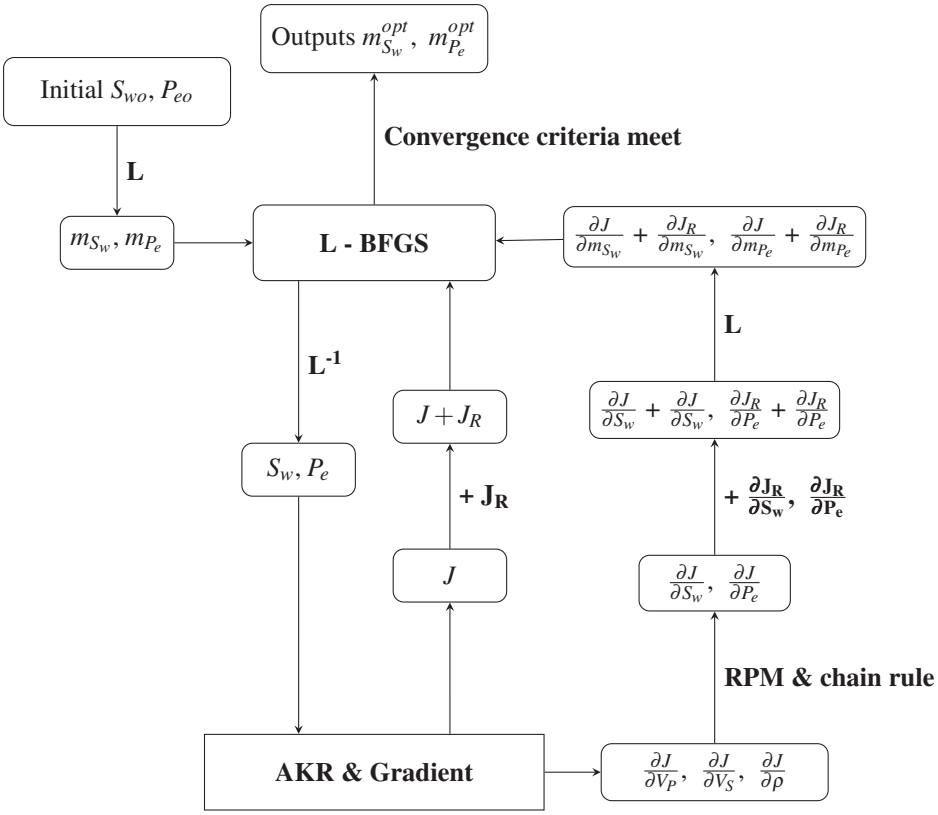

Figure 3.1: Inversion workflow: Flowchart describes the inversion process defined by the five steps. Here AKR, RPM, L, and L^{-1} stand for the Aki and Richards equation, rock physics models, and logistic and inverse logistic functions respectively while J_R defines the regularization of the objective function.

clastic sediments of the Jurassic/Triassic geological ages. The oil-water contact (OWC) is interpreted at approximately 1967 m. The available well logs are shown in the time domain in Figure 3.2. The oil-saturated reservoir sand is located in the two-way time interval of 1865 - 1890 ms and is highlighted in red. The well logs were measured before production started (baseline case). We simulate various time-lapse scenarios during production and injection using rock physics models. We test the inversion method for different noise levels and initial optimization values. Reservoir rock and pore fluids properties used to compute the elastic variables through the rock physics relationships are presented in Table 3.1. The properties of the pore fluid at in-situ conditions are calculated by applying Batzle-Wang relationships and rock mineral densities and bulk moduli are taken from the literature (Batzle and Wang 1992; Mavko et al. 2020).

In the first application case, we present a synthetic seismic AVO gathers modeled on the basis of the well logs describing the reservoir conditions before production starts (baseline case). The seismic forward model is simulated with different signal-

Table 3.1: Reservoir rock and fluid parameters used in the rock physics model.

Parameters	Average values
Average effective porosity (ϕ)	0.26
Critical porosity (ϕ_c)	0.40
Reservoir Temperature (T)	78.18 ($^\circ C$)
Reservoir pressure (P_e)	26 (MPa)
Max. reservoir pressure	40 (MPa)
Density of oil (ρ_o)	0.821 (g/cm^3)
API of oil	35
Gas/oil ratio (GOR)	145.7
Bulk modulus of oil (K_o)	1.04 (GPa)
Density of water (ρ_o)	0.987 (g/cm^3)
Bulk modulus of water (K_o)	2.55 (GPa)

to-noise ratios (S/N), including S/N $= \infty$ and S/N $= 15$. The model variables for the baseline survey include water saturation, effective pressure, and corresponding P- and S-wave seismic velocities and density (Figure 3.2). Seismic velocities and bulk density are obtained through Gassmann's fluid replacement model (FSM) and the modified MacBeth's pressure relations. The rock physics model predictions (green curves) are in agreement with the true well logs (black curves).

The two PP seismic synthetic models representing pre-production scenarios with actual water saturation (about $S_w \approx 0.35$) and effective pressure (about $P_e \approx 26$ MPa) in the oil-producing part are displayed in Figure 3.3. The seismic gathers are numerically modeled by the convolution of a Ricker wavelet of 30 Hz and the reflection coefficient series is calculated using the AVO linearized equation. The synthetic gathers are modeled for incident angles between 0° and 30° at intervals of 5°. The initial model is obtained by filtering the actual wireline logs data to a low frequency.

Figure 3.4 shows the AVO inversion results plotted along with the initial and true models for the baseline water saturation and effective pressure. Figure 3.4 (left penal) shows the inverted models estimated from the noise-free seismic gather while Figure 3.4 (right panel) shows those estimated from the noisy data. The predicted variables match relative well the true models in both cases. The mismatches in the estimated models are below the resolution of the seismic measurements scale. The high-frequency oscillation in the inverted models of effective pressure within the reservoir seal (time window 1850 - 1870 m) might be an edge artifact due to the sharp truncation or abrupt amplitude change at the edges and can be removed by applying a taper to both ends of the seismic inverted traces. A comparative correlation between the mean values of the true and predicted results of the model variables within the reservoir zone is shown in Table 3.2 and the results demonstrate the accuracy of the presented inversion process as the RMS error is fair minor.

As part of the sensitivity study to the backgrounds, we investigate the influence of the initial model by imposing a linear trend on the initial model instead of a filtered model. Figure 3.5 illustrates the inverse prediction of effective pressure and water saturation using the linear trend for noise-free. The inversion algorithm shows accurate

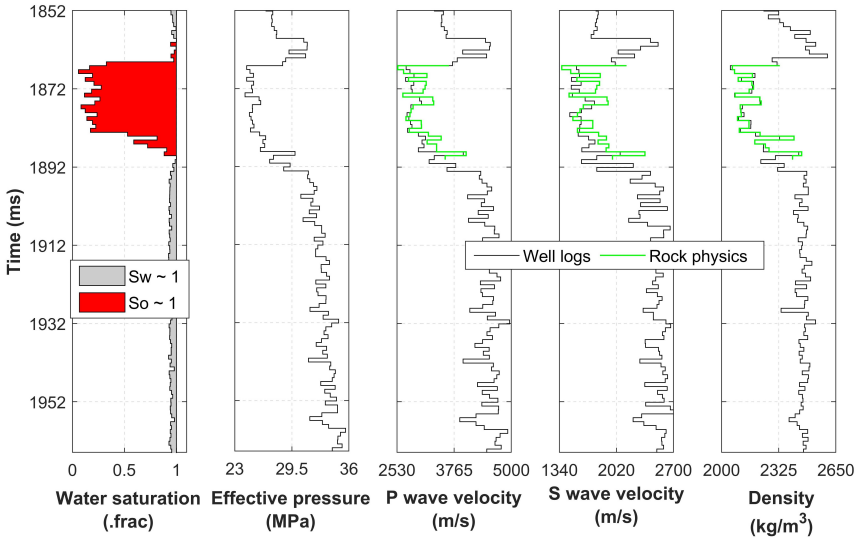

Figure 3.2: Water saturation, effective pressure, and the corresponding seismic velocities and density at the well location (actual data in black and rock physics model predictions in green) in the reservoir zone at in situ conditions. The reservoir sand ($S_w \approx 0.35$) is highlighted.

results also if the background model is back from the real reference models.

In the second example, we assume that at the date of the seismic data acquisition for monitoring, water saturation has increased up to 0.87 (or approximately over 0.80) in the reservoir zone due to oil production, and pressure has dropped approximately to 4.02 MPa. The new set of seismic and model variables for the monitor case is shown in Figure 3.6. The variation in saturation-pressure profiles corresponding to the reservoir sand are highlighted with arrows and the computed seismic properties within the reservoir level are also displayed. The inversion results for the noise-free case of the current saturation-pressure scenarios are illustrated in Figure 3.7 and show a close agreement with the actual reservoir properties. A numerical comparison between reference and inverted values of model properties (saturation and pressure variables) for the monitor case is shown in Table 3.2. The root means square errors for both saturation and pressure are relatively low.

The water saturation and effective pressure changes (ΔS_w and ΔP_e respectively) predicted by the proposed algorithm are displayed in Figure 3.8 and are crosschecked with the reference values. The reference mean values for ΔS_w and ΔP_e are 0.52 and 4.02 MPa and the inverted estimates are 0.51 and 3.93 MPa respectively (Table 3.2). The uncertainty in the optimal solution of water saturation and pressure is comparably minor regardless of the high variability in the background models and that supports the consistency and reliability of the method.

In the third example, we assume a partial reservoir depletion due to water injection, where the water has been injected in the lower part of the reservoir ($S_w \approx 1$) with constant

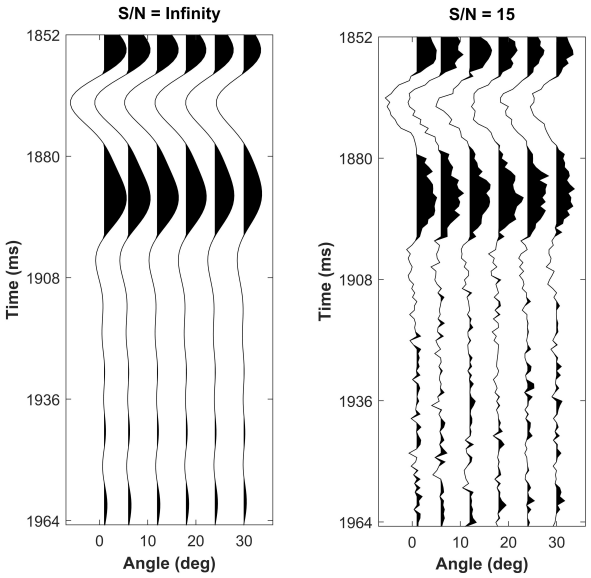

Figure 3.3: Seismic AVO gathers modeled up to maximum incident angle 30° for signal-to-noise ratios SNR = ∞ and SNR = 15).

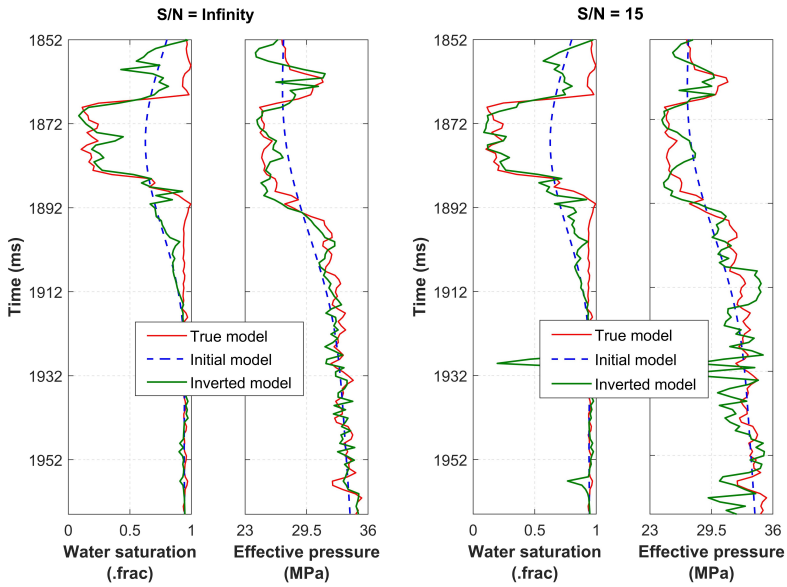

Figure 3.4: Inverted water saturation and effective pressure models obtained from the noise-free (SNR = ∞) data (left panel) and noisy (SNR = 15) data (right panel).

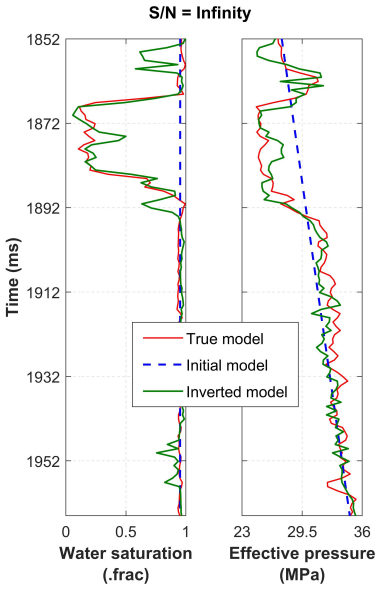

Figure 3.5: Inverted water saturation and effective pressure models obtained using a linear trend for the initial model.

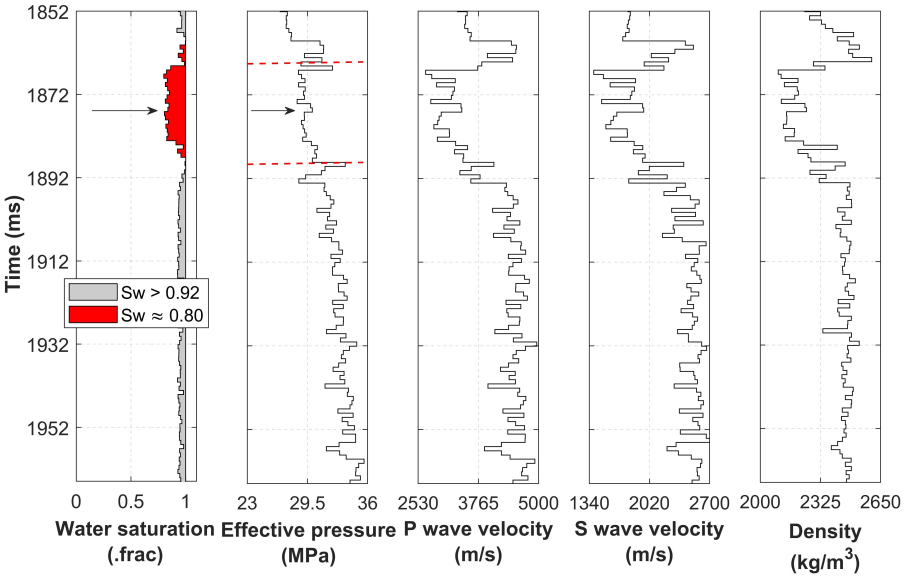

Figure 3.6: Water saturation and effective pressure for the monitor survey. Dynamic changes are marked by the arrows.

Table 3.2: Comparison of average true and inverted results of the water saturation and effective pressure within reservoir window (1865 - 1890 ms) for pre- and post-production cases. The last two rows of the table describe the inversion results in the case of patchy fluid distribution. The RMSE values represent the errors in the reservoir interval (between 1D arrays of true and inverted values) instead of the given mean values. The inverted results with the patchy rock physics model are more accurate and show low errors.

Model variables	True model	Inverted model	RMSE
Uniform fluid distribution			
Baseline case - S/N = infinity			
S_w (.frac)	0.35	0.38	0.10
P_e (MPa)	25.65	25.75	1.27
Monitoring case			
S_w (.frac)	0.87	0.89	0.068
P_e (MPa)	29.67	29.68	1.20
Difference			
ΔS_w (.frac)	0.52	0.51	
ΔP_e (MPa)	4.02	3.93	
Baseline case - S/N = 15			
S_w (.frac)	0.35	0.34	0.11
P_e (MPa)	25.65	25.84	1.56
Patchy fluid distribution			
Baseline case - S/N = infinity			
S_w (.frac)	0.35	0.32	0.11
P_e (MPa)	25.65	25.74	1.17
S/N = 15			
S_w (.frac)	0.35	0.37	0.18
P_e (MPa)	25.65	26.26	1.25

pressure. The model variables for the fluid injection case are shown in Figure 3.9a. The inversion results for the model variables and the homologous predicted properties are shown in Figure 3.9b. The inversion of water saturation shows accurate results compared to the reference model in both injected and partially oil-saturated zones, whereas the pressure prediction is less accurate.

In the fourth example, we assume a patchy saturation rock physics model for the pore fluid mixture. The inverse solution for saturation and pressure is shown in Figure 3.10 and shows very close agreement with the true models. The quantitative comparison of the results is given in Table 3.2. The comparison of the estimation of water saturation and pressure variables by using uniform and patchy fluid distribution rock physics models in Table 3.2 shows that the patchy rock physics model provides a better prediction with lower RMSE values.

Furthermore, we investigate the model uncertainty based on the variability of the initial model. The uncertainty in the inverse solution is evaluated using Monte Carlo

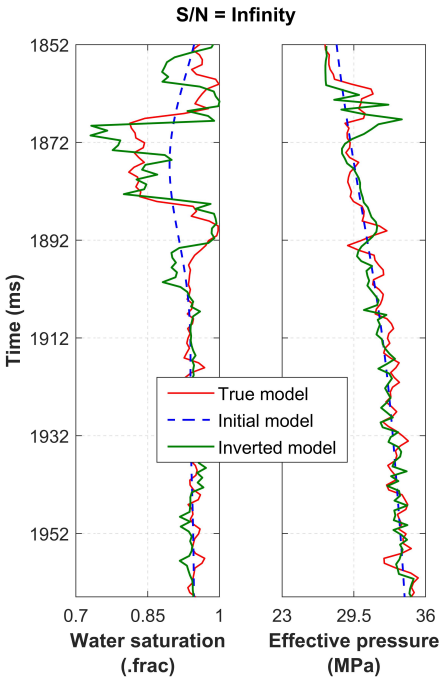

Figure 3.7: Inverted water saturation and effective pressure models for the monitor survey.

simulation in which we create a set of prior realizations and then obtain the analogous group of posterior realizations. We first create a set of 200 prior background realizations of the saturation and pressure at well bore location by sampling from a multivariate spatially correlated Gaussian distribution (Buland and Omre 2003b; Grana et al. 2021). The empirical prior distribution estimated from the 200 realizations is demonstrated in Figure 3.11. We then run the developed inversion workflow to every initial model individually and estimate the distributions of the predicted realizations (Fig. 3.12). The actual water saturation and pressure curves show a very good agreement with the maximum of the posterior distribution. The uncertainty across the posterior distribution stays reasonably small compared to the large variability among the prior distribution. However, the uncertainty at some locations is higher and the reference models of saturation and pressure variables do not show a good correlation with the maximum of the posterior distribution. Nevertheless, the correlations with the true models are very good at the reservoir zone. In the case of incorrect bound constraints, the inversion method can underestimate/overestimate the properties in the reservoir zone which can be therefore overcome by applying narrow and accurate physical constraints. The distribution of the posterior is much narrower (brighter yellow and narrower confidence interval). The ranges of the color bars of prior and posterior for water saturation are the same (0 - 0.1) and likewise for the pressure distribution are 0 - 0.035.

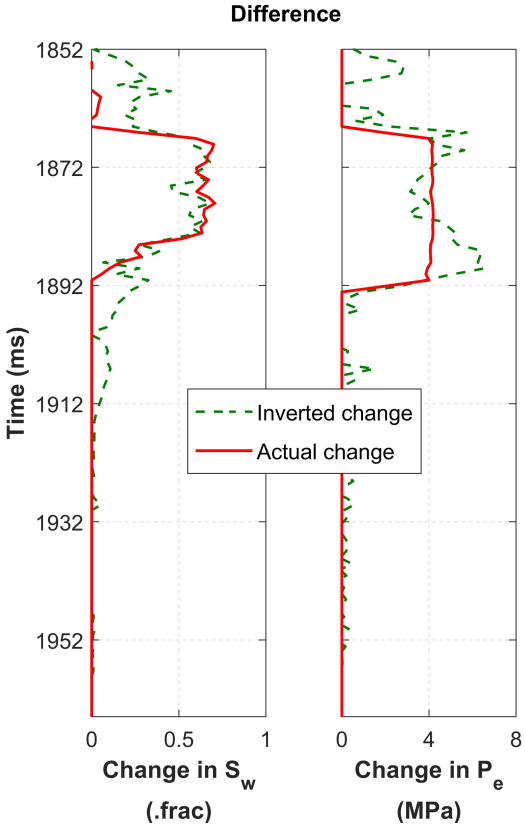

Figure 3.8: Changes in water saturation and effective pressure: reference values versus predicted models.

Similarly, at a location away from the wells or in the case of 2D or 3D scenarios, the uncertainties in the model variables prediction can be captured by running the inversion method for numerous prior realizations and by computing the posterior solution. Then the mean standard deviation of the posterior solution can be used as a possible estimation.

In the latter half of the application section, we apply the presented inverse modeling process to a 2D line extracted from the reservoir model from the Smeaheia CO_2 storage field, located within the Northern North Sea. The Smeaheia area is based around 20 and 40 km east and northwest of the Troll oil and gas field. The reservoir in the Smeaheia CO_2 storage site is the brine aquifer that could be potentially used for carbon capture storage (Mulrooney et al. 2020). In this research work, we apply the inversion technique for the monitor case mimicking the CO_2 injection scenario and then take the difference between the baseline and true/inverted monitors to estimate the CO_2 saturation and changes in effective pressure. The dynamic flow simulation is carried out by Eclipse to calculate the field's saturation-pressure evaluation with gradual CO_2 injection throughout the sand reservoir (Paap et al. 2022). The fluid state of injected

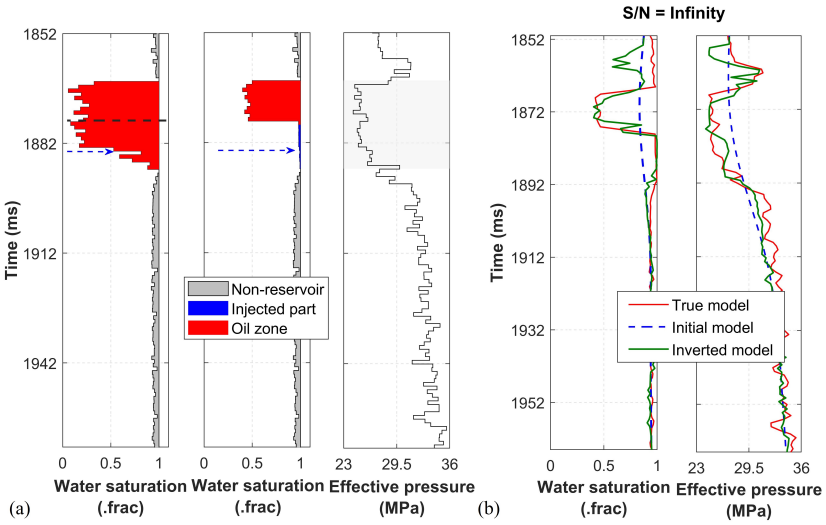

Figure 3.9: (a) Model variables (from left to right) baseline water saturation, and water saturation and pressure curves after injection (b) inverted water saturation and effective pressure for the monitor survey mimicking partial reservoir depletion due to water injection.

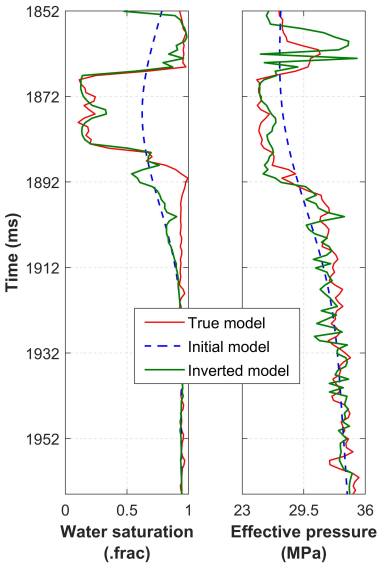

Figure 3.10: Inverted water saturation and effective pressure for the baseline survey mimicking patchy fluid mixture.

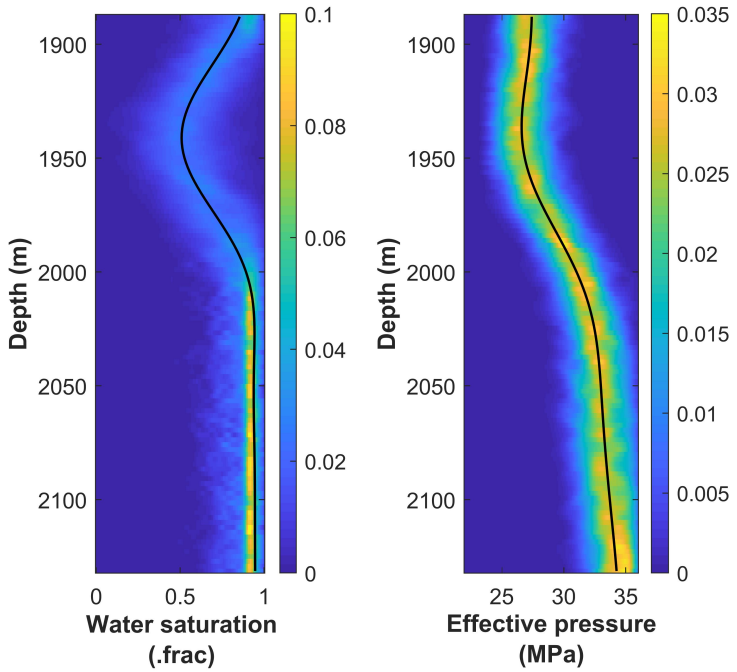

Figure 3.11: Prior realizations of water saturation and effective pressure at the well location.

CO_2 is assumed supercritical carbon dioxide as the fluid properties e.g., CO_2 density and bulk modulus (600 - 700 kg/m^3 and 100 MPa respectively) lie in the supercritical region determined by (Yam and Schmitt 2011) based on the laboratory data. We then use the patchy fluid distribution rock physics model to link the model properties with elastic parameters for this inversion application. The patchy saturation model describes that the multiple fluid states exist separately in the pores and therefore it provides a more accurate computation of seismic velocity in the partially saturated reservoirs. During CO_2 storage, however, comparatively high pressure is applied to the storage aquifer and CO_2 is injected rapidly; therefore, CO_2 distribution in the reservoir may become patchy instead of homogeneous saturation. The empirical constants (E_k and E_μ) in equation 3.5 are calculated by integrating rock physics model-based seismic velocities with the Hertz-Mindlin model (Mindlin 1949). In this research work, we adopted a strategy to apply the inversion technique for the monitor case mimicking the injection scenario. It can be applied on baseline and monitor datasets separately to obtain a high-resolution baseline and monitor models of reservoir dynamic properties and is more robust against potential differences in the frequency spectra of the wavelets of seismic datasets from two different vintages. However, this inversion method can be easily adapted to the case of time-lapse seismic differences as chosen by (Grana and Mukerji 2015).

The true 2D models of water saturation and effective pressure before CO_2 injection

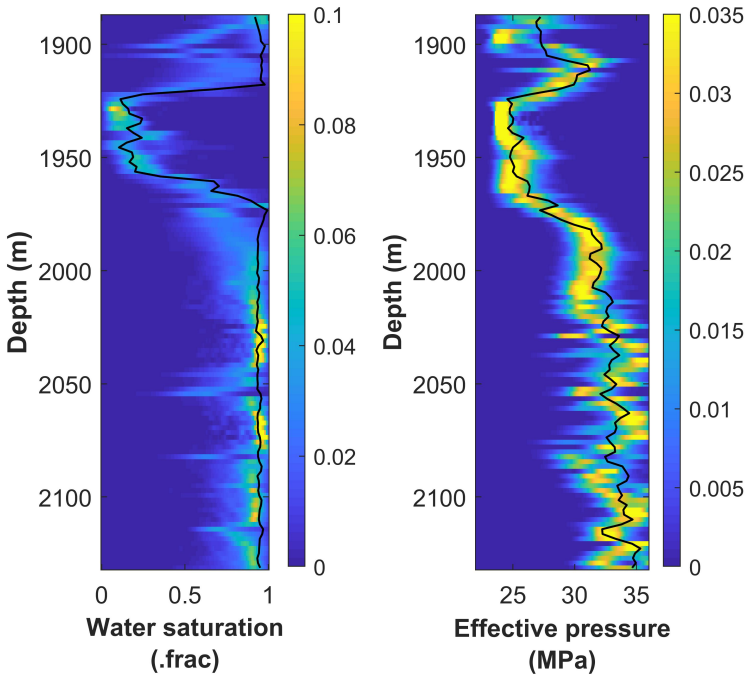

Figure 3.12: Inverted realizations of water saturation and effective pressure based on Monte Carlo inverted simulations.

(baseline case) are shown in Figure 3.13. For the baseline case, it is assumed that the injection site is fully water-saturated and effective pressure is continuously increasing with depth. The seismic pre-stack gathers for the monitoring data, including near, mid, and far angles, are displayed in Figure 3.14. These seismic gathers are numerically simulated with a signal-to-noise ratio equal to 20. The seismic section has 97 traces and 100-time samples per trace with a sampling interval of 2 ms for three seismic waves incident angles 10°, 20° and 30° (Bhakta et al. 2022; Mavko et al. 2020; Paap et al. 2022). The bright spot anomaly on the seismic images is because of the acoustic impedance contrast between CO_2 plume and saline-saturated sand. The effect is more prominent at far-angle traces.

In the monitoring case, we test the inversion to monitor the water saturation and pressure variations resulting from the injection of CO_2. The true saturation and pressure models for the monitor survey are shown in Figure 3.15 (left side panel). Higher CO_2 saturation levels are observed above the injection point; likewise, low effective pressure values are also observed, as shown in Figure 3.15 (left side panel). The inverse modeling results for saturation and pressure are described in Figure 3.15 (right side panel). The inversion accurately captures the spatial distribution of the CO_2 plume. The differences between true and inverted saturation and effective pressure variables are plotted in Figure 3.16. The actual changes are computed by taking the difference between true

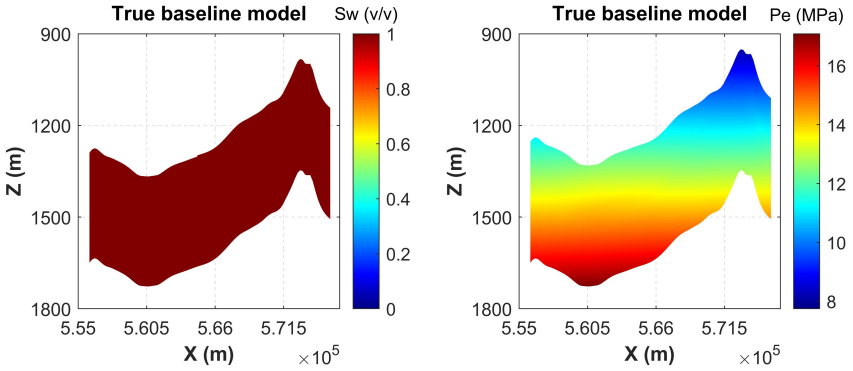

Figure 3.13: True water saturation and effective pressure models for the baseline case.

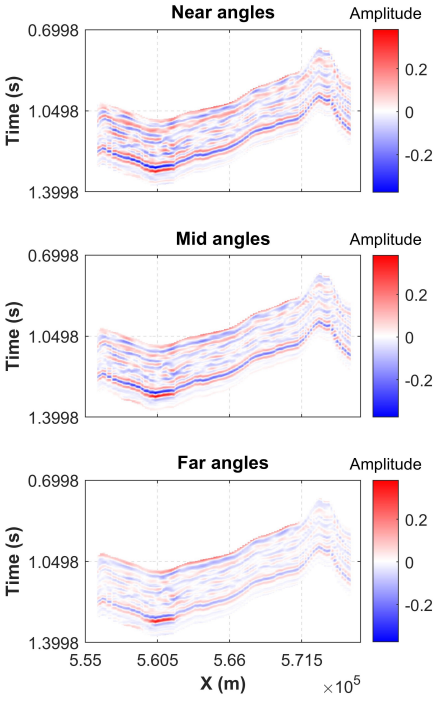

Figure 3.14: Synthetic seismic dataset modeled for the monitoring case: near, mid, and far angles. A Ricker wavelet of 35 Hz is used to convolve it with the earth's reflectivity series.

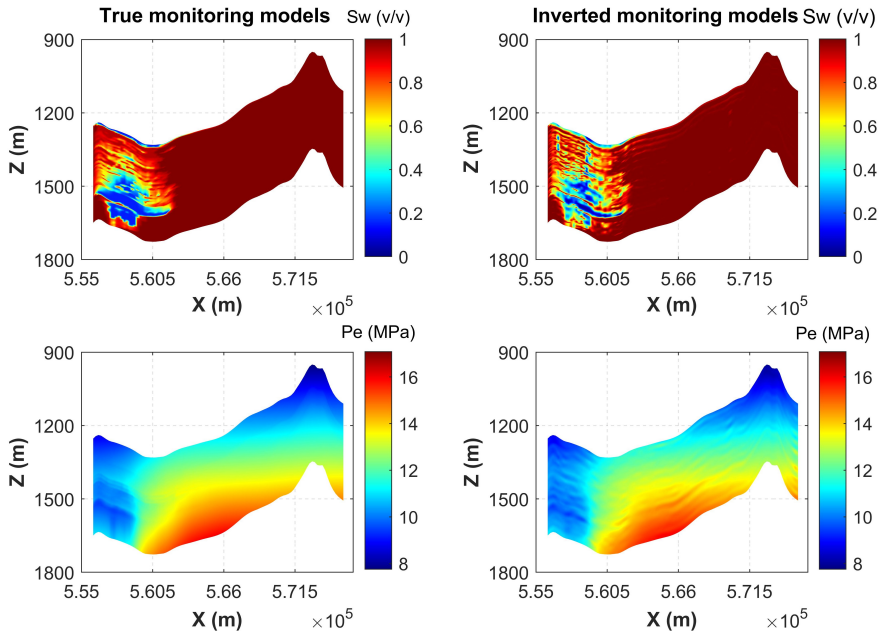

Figure 3.15: True and predicted water/CO_2 saturation and effective pressure models for the monitoring case.

models before and after injection and between the true model before injection and the inverted monitor model.

In the next application example, the 4D FAVO inversion has been applied to the 2D monitoring data of the Smeaheia field by using the starting models that are sufficiently far from the reference models. The inversion method is applied to the first 40 traces covering the CO_2 injection plume. The reference models, initial models, predicted models, and real and inverted changes in water saturation and effective pressure due to CO_2 injection are shown in Figure 3.17 and 3.18 respectively. The results describe that the inversion method provides a good estimation of dynamic properties even if the initial models are not sufficiently close to the true models. However, the uncertainty at some locations is comparatively high.

To measure the accuracy of the predicted models, the root mean squared error (RMSE) between the true and inverted monitor models of saturation and pressure variables given in Figures 3.15, 3.17 and 3.18 is computed. The RMSEs are calculated for the first 40 traces covering the CO_2 injection plume. The RMSEs are plotted in Figures 3.19 and 3.20. Figure 3.19 represents the error of the predicted model shown in Figure 3.15 wherein the initial models are assumed somehow closer to the reference models. Figure 3.20 describes the errors for the estimated models when the initial models are sufficiently far away from the true models. The lower RMSE in both saturation and pressure-predicted models shown in Figure 3.19 indicates that the inverted model is a better fit with the reference model. In Figure 3.20, the RMSEs in the saturation

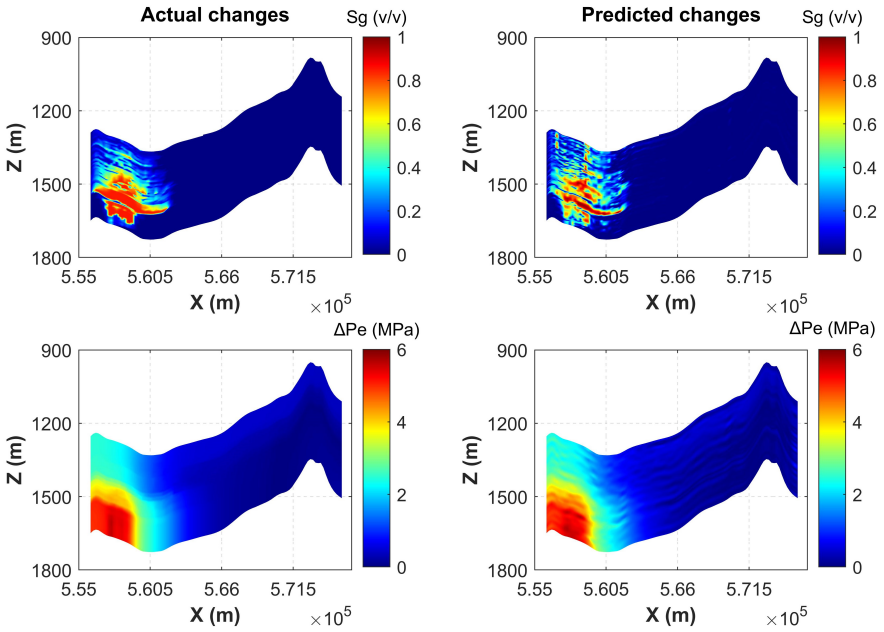

Figure 3.16: Actual and predicted changes in water saturation and effective pressure due to CO_2 injection. S_g indicates the CO_2 saturation and ΔP_e represents the changes in effective pressure.

and pressure models are comparatively higher for some traces but still fall within the acceptable range.

3.5 Discussion

In the proposed time-lapse AVO inversion methodology, we implement a gradient-based optimization method combined with the adjoint state technique for the computation of the gradient of the objective function with respect to the model properties of interest. The adjoint method is faster and more efficient than other methods such as finite difference or Fréchet derivative (Plessix 2006). The limited memory BFGS approximates the second-order Hessian inverse, stores only a limited number of previous iterations, and provides a good convergence rate to the minima. The inversion is relatively efficient thanks to the use of the adjoint method. However, the inversion results might not be stable and require a regularization term to increase the stability of the solution. The current implementation is based on independent inversions of the base and monitor surveys. In theory, the inversion method could also be applied to time-lapse seismic differences (Grana and Mukerji 2015); however, this approach requires a warping technique for travel time corrections of the monitor survey. The successful application of this approach relies on the repeatability of the seismic surveys (Dinh and Van der Baan 2019; Romero et al. 2023; Trani et al. 2011).

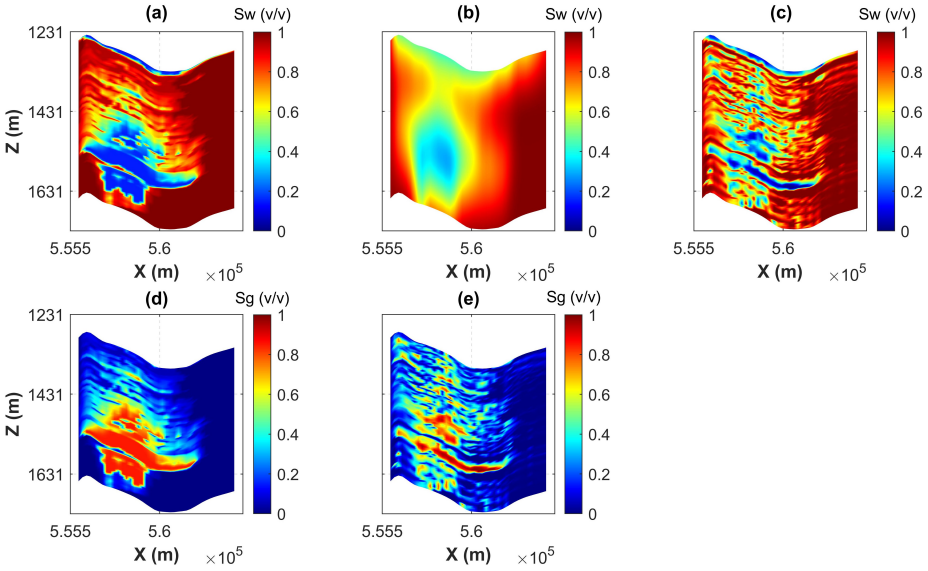

Figure 3.17: 2D slice of the (a) reference model, (b) initial model, (c) predicted model, (d) reference changes in saturation variables, and (e) predicted changes in the model property.

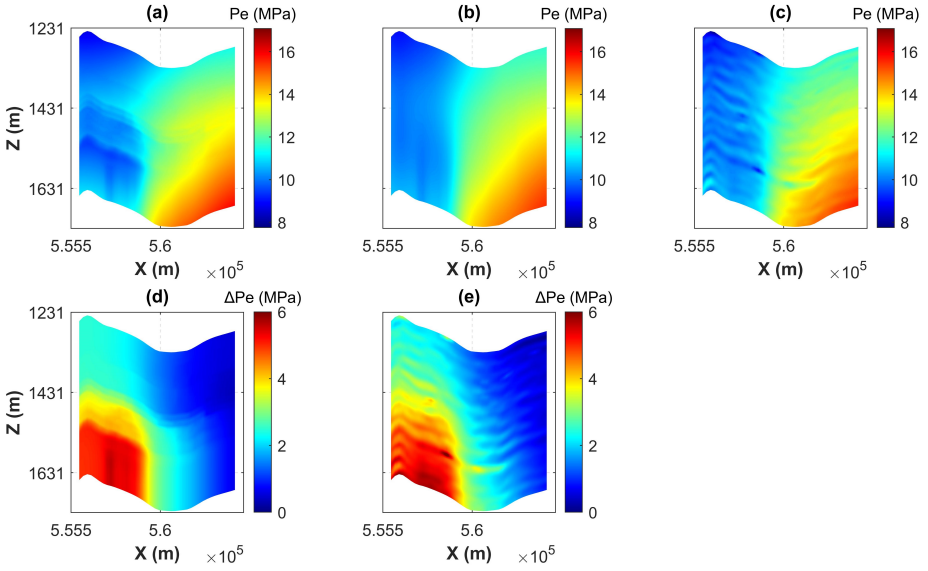

Figure 3.18: 2D section of the (a) reference model, (b) initial model, (c) predicted model, (d) reference changes in effective pressure variables, and (e) predicted changes in the model property.

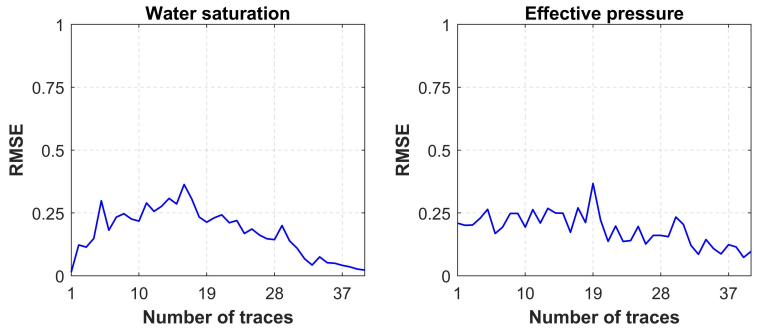

Figure 3.19: Root mean squared errors (RMSE) between the predicted and actual values of the first 40 traces are plotted. The RMS error plots are calculated between true and predicted models shown by Figure 3.15.

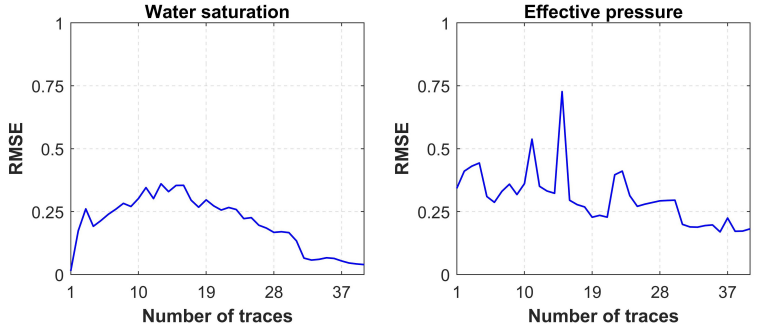

Figure 3.20: Root mean squared errors (RMSE) between the predicted and actual values of the first 40 traces are plotted. The RMS error plots are calculated between true and predicted models shown by Figure 3.17 and 3.18.

The main challenge of rock physics inversion for time-lapse studies is the calibration of the rock physics model and the uncertainty in the calibrated parameters far away from the well controls due to the spatial heterogeneity of rock and fluid properties. The proposed rock physics model includes some approximations such as the negligible effect of pressure on density and the assumption that rock physics parameters do not change spatially. However, the effect of density and reservoir porosity changes due to compaction can be included by using MacBeth's model (MacBeth 2004) and the compaction-porosity trend (Rimstad et al. 2012) as described (Ahmed et al. 2024). The relationship between elastic moduli and pressure includes a porosity term that controls the asymptotic value of the elastic moduli when pressure increases. Lang and Grana (2017) show that the parameters of the exponential relation depend on the initial porosity and saturation values. The proposed approach can be extended to the porosity-dependent formulation by including the porosity term in the partial derivatives. This term is certainly relevant in datasets with high spatial heterogeneity in porosity and when the compaction due to the production mechanisms causes significant porosity

reduction in the reservoir rocks due to the decreasing effective pressure. In addition, the rock physics model used for this study is assumed to be less appropriate for the carbonate reservoir due to their complex pore system and the violation of some assumptions of Gassmann's equation. However, this inversion workflow can be applied to the carbonate reservoirs with some percent of uncertainty in the seismic properties. More detailed comments are added in the concluding remarks of the thesis (see Chapter 6).

For applications with large lateral heterogeneity in rock properties, the inversion might provide inaccurate predictions of the saturation changes due to the effect of the rock properties on elastic properties. A possible solution is to increase the number of unknown model variables and invert for rock properties and saturation changes at the same time. This approach often leads to large uncertainty in the predictions. Furthermore, one of the main limitations of the current approach is that it does not account for uncertainty in the rock physics model. Overall, the larger the lateral heterogeneity, the less precise the saturation predictions are.

The gradient descent-based optimization requires an initial guess to find the minima of a misfit function. Low-frequency models can be used as initial models by filtering well-log data at the borehole locations and interpolating far away from the wells along the seismic horizons. Alternatively, initial pressure and saturation models can be estimated from basin models, nearby fields, borehole data, and static reservoir models. The current approach can be included in a Bayesian framework by applying a stochastic method such as Monte Carlo sampling or Approximate Bayesian Computation (Grana et al. 2021); however, accurate assessment of the posterior uncertainty might require a large number of stochastic realizations leading to an increase of the computational cost.

It is generally difficult to assess the accuracy of the inversion because of the limited number of direct measurements. The models can be calibrated using core samples and well logs, but the inversion results can only be compared to fluid flow simulation models for validation. The uncertainty of the model variables obtained in this approach should be interpreted as a measurement of the precision of the inversion, but the absolute values often depend on initial assumptions and uncertainty sources. A possible verification of this approach is with seismic history matching where seismic data are integrated into a data assimilation workflow that accounts for fluid flow simulation. This approach is beyond the scope of our work because it is not a direct validation of the inversion as the seismic history matching is also the result of a model.

3.6 Conclusions

We presented a non-linear inversion for the time-lapse seismic AVO dataset to predict water saturation and effective pressure variables due to reservoir production and/or injection. The inversion is based on the linearized AVO approximation and rock physics relations including well-known fluid substitution models (FSM) and modified MacBeth's pressure equation to link the effect of variations in fluid saturation and pressure to the reflectivity response. The proposed 4D AVO inversion algorithm is relying on the first-order gradient-descent-based iterative optimization algorithm wherein a non-linear L-BFGS optimization algorithm is used to minimize the least-square L2 norm misfit function iteratively. The novel contribution in the developed inversion process is the

analytical derivation of the first-order gradients of the data misfit function with respect to the time-lapse model variables by implementing the adjoint-state method, which results in a fast and efficient algorithm. The proposed inversion is also less dependent on the choice of background models compared with traditional methods especially when reservoir dynamic properties have a good spatial correlation with the elastic properties. The primary limitation of the proposed technique is that it depends on the constraints to limit the solution space; however, such constraints can be obtained by integrating prior geological information and engineering data. The results show that adequate constraint limits are very helpful in reducing the uncertainty in the predicted models. To validate the proposed method, we applied the inversion to simulated reservoir scenarios obtained by applying dynamic changes to a set of true well logs, for different production mechanisms and different noise conditions. The inversion method was also validated on a 2D realistic reservoir model for CO_2 monitoring. The results show that the inversion workflow provides accurate estimates of saturation and pressure values for the monitor surveys. However, the RMS error in the results of CO_2 saturation and pressure inversion increases when the initial models are sufficiently away from the reference models. This is perhaps due to the fact of low spatial correlation between saturation and pressure (after injection) and with elastic properties (V_P, V_S, ρ). The model properties are inverted by using two rock physics models (uniform and patchy) and the results describe that the patchy distribution model is more accurate than the uniform fluid distribution model. The inversion method conceivably expanded to all other known rock physics models with adequate calibration of the rock physics parameters. Similarly, the presented inversion technique can be extended to invert 4D seismic measurements for other reservoir parameters, for instance, changes in temperature due to fluid/steam injection or changes in porosity caused by the subsidence. Real case studies might require the calibration of rock physics parameters using core samples or well logs.

3.7 Acknowledgments

We are grateful to the National IOR Centre of Norway led by the University of Stavanger for the financial support of this project. We would also like to acknowledge Lundin Energy Norway and their partners Wintershall Dea and OMW in the Edvard Grieg license for providing the seismic data and well logs for this project. The computations and simulations were carried out with resources given by UNINETT Sigma2 - the National Infrastructure for High-Performance Computing and Data Storage in Norway. The authors also like to acknowledge the Digimon project which is an ACT2 project (no 299622) supported by the ACT international initiative for 2D synthetic data of CO_2 monitoring. We are deeply indebted to Professor Tapan Mukerji for his review and some good suggestions to improve the quality of our work.

3.8 Appendix A: Analytical solution of the partial derivatives

To model the effect of patchy fluids mixture in the reservoir, the patchy saturated bulk modulus (K^*_{sat}) is computed according to the rock physics model by Wollner and Dvorkin (2018):

$$K^*_{sat} = \left[\frac{S_w}{K_{sat-wet}+4\mu_d/3} + \frac{1-S_w}{K_{sat-oil}+4\mu_d/3}\right]^{-1} - \frac{4}{3}\mu_d \tag{3.44}$$

and the saturated bulk moduli in water- and oil-filled patches are:

$$K_{sat-wet} = K_m \frac{\phi K_d - (1+\phi)K_w K_d/K_m + K_w}{(1-\phi)K_w + \phi K_m - K_w K_d/K_m} \tag{3.45}$$

$$K_{sat-oil} = K_m \frac{\phi K_d - (1+\phi)K_o K_d/K_m + K_o}{(1-\phi)K_o + \phi K_m - K_o K_d/K_m} \tag{3.46}$$

This model assumes that the fluid patches are hydraulically isolated compared to others and that the elastic wave wavelength is higher than the individual patch size of the fluid.

The partial derivative of the compressional wave velocity with respect to water saturation for patchy saturation can be written in the discretized form as:

$$\frac{\partial V^*_P[i]}{\partial S_w[i]} = \frac{\partial V^*_P[i]}{\partial \rho[i]} \cdot \frac{\partial \rho[i]}{\partial S_w[i]} + \frac{\partial V^*_P[i]}{\partial K^*_{sat}[i]} \cdot \frac{\partial K^*_{sat}[i]}{\partial S_w[i]} \tag{3.47}$$

where

$$\frac{\partial V^*_P}{\partial \rho} \cdot \frac{\partial \rho}{\partial S_w} = -\frac{1}{2\rho^{3/2}} \left(K^*_{sat} + \frac{4}{3}\mu_d\right)^{1/2} \phi\ (\rho_w - \rho_o) \tag{3.48}$$

$$\begin{aligned} \frac{\partial V^*_P}{\partial K^*_{sat}} \cdot \frac{\partial K^*_{sat}}{\partial S_w} = \frac{1}{2\sqrt{\rho}} \left(K^*_{sat} + \frac{4}{3}\mu_d\right)^{-1/2} \cdot \\ (-1)\left[\frac{S_w}{K_{sat-wet}+4\mu_d/3} + \frac{1-S_w}{K_{sat-oil}+4\mu_d/3}\right]^{-2} \\ \left[\frac{1}{K_{sat-wet}+4\mu_d/3} - \frac{1}{K_{sat-oil}+4\mu_d/3}\right] \end{aligned} \tag{3.49}$$

where * with V_P and K_{sat} indicates the properties representing the patchy saturation case.

Similarly, the partial derivative of elastic wave velocity (V^*_P) with respect to effective pressure can be modified for the patchy saturation model as:

$$\frac{\partial V^*_P[i]}{\partial P_e[i]} = \frac{\partial V^*_P[i]}{\partial K^*_{sat}[i]} \cdot \frac{\partial K^*_{sat}[i]}{\partial P_e[i]} + \frac{\partial V^*_P[i]}{\partial \mu_d[i]} \cdot \frac{\partial \mu_d[i]}{\partial P_e[i]} \tag{3.50}$$

where

$$\begin{aligned} \frac{\partial K^*_{sat}[i]}{\partial P_e[i]} = \frac{\partial K^*_{sat}[i]}{\partial K_{sat-wet}[i]} \cdot \frac{\partial K_{sat-wet}[i]}{\partial P_e[i]} + \frac{\partial K^*_{sat}[i]}{\partial K_{sat-oil}[i]} \cdot \\ \frac{\partial K_{sat-oil}[i]}{\partial P_e[i]} + \frac{\partial K^*_{sat}[i]}{\partial \mu_d[i]} \cdot \frac{\partial \mu_d[i]}{\partial P_e[i]} \end{aligned} \tag{3.51}$$

and

$$\frac{\partial K_{sat-wet}[i]}{\partial P_e[i]} = \frac{\partial K_{sat-wet}[i]}{\partial K_d[i]} \cdot \frac{\partial K_d[i]}{\partial P_e[i]} \tag{3.52}$$

$$\frac{\partial K_{sat-oil}[i]}{\partial P_e[i]} = \frac{\partial K_{sat-oil}[i]}{\partial K_d[i]} \cdot \frac{\partial K_d[i]}{\partial P_e[i]} \tag{3.53}$$

$$\frac{\partial V_P^*}{\partial K_{sat}^*} = \frac{1}{2\sqrt{\rho}} \left(K_{sat}^* + \frac{4}{3}\mu_d \right)^{1/2} \tag{3.54}$$

$$\frac{\partial K_{sat}^*}{\partial K_{sat-wet}} = \left[\frac{S_w}{K_{sat-wet} + 4\mu_d/3} + \frac{1 - S_w}{K_{sat-oil} + 4\mu_d/3} \right]^{-2} \frac{S_w}{(K_{sat-wet} + 4\mu_d/3)^2} \tag{3.55}$$

$$\frac{\partial K_{sat-wet}}{\partial K_d} = \frac{K_m^2 \phi^2 (K_w^2 - 2K_m K_w + K_m^2)}{(K_m K_w (1-\phi) + K_m^2 \phi - K_d K_w)^2} \tag{3.56}$$

$$\frac{\partial K_{sat}^*}{\partial K_{sat-oil}} = \left[\frac{S_w}{K_{sat-wet} + 4\mu_d/3} + \frac{1 - S_w}{K_{sat-oil} + 4\mu_d/3} \right]^{-2} \frac{1 - S_w}{(K_{sat-oil} + 4\mu_d/3)^2} \tag{3.57}$$

$$\frac{\partial K_{sat-oil}}{\partial K_d} = \frac{K_m^2 \phi^2 (K_o^2 - 2K_m K_o + K_m^2)}{(K_m K_o (1-\phi) + K_m^2 \phi - K_d K_o)^2} \tag{3.58}$$

$$\frac{\partial K_{sat}^*}{\partial \mu_d} = -\left[\frac{S_w}{K_{sat-wet} + 4\mu_d/3} + \frac{1 - S_w}{K_{sat-oil} + 4\mu_d/3} \right]^{-2} \left[\frac{-S_w}{(K_{sat-wet} + 4\mu_d/3)^2} \frac{4}{3} + \frac{-(1 - S_w)}{(K_{sat-oil} + 4\mu_d/3)^2} \frac{4}{3} \right] - \frac{4}{3} \tag{3.59}$$

$$\frac{\partial V_P^*}{\partial \mu_d} = \frac{2}{3\sqrt{\rho}} \left(K_{sat}^* + \frac{4}{3}\mu_d \right)^{-1/2} \tag{3.60}$$

The partial derivatives of K_d and μ_d with respect to effective pressure are given in the equations 3.33 and 3.35 respectively.

Chapter 4

Frequency-dependent AVO inversion applied to physically based models for seismic attenuation

By:
Ahmed, Nisar[1]
Weibull, Wiktor Waldemar[1]
Quintal, Beatriz[2]
Grana, Dario[3]
Bhakta, Tuhin[4]

[1]Department of Energy Resources, 4021 Stavanger, University of Stavanger, Norway
[2]Institute of Earth Sciences, University of Lausanne, 1015 Lausanne, Switzerland
[3]Department of Geology and Geophysics, School of Energy Resources, University of Wyoming, Laramie, Wyoming 82071, United States
[4]NORCE Norwegian Research Centre, Norway

Printed in:
Geophysical Journal International, 233:1, pp 234–252, (2023)
https://doi.org/10.1093/gji/ggac461.

4.1 Summary

Seismic inversion of amplitude versus offset (AVO) data in viscoelastic media can potentially provide high-resolution subsurface models of seismic velocities and attenuation from offset/angle seismic gathers. P- and S- wave quality factors (Q), whose inverse represent a measure of attenuation, depend on reservoir rock and pore fluid properties, in particular, saturation, permeability, porosity, fluid viscosity, and lithology; however, these quality factors are rarely taken into account in seismic AVO inversion. For this reason, in the present work, we aim to integrate quality factors derived from physically-based models in AVO inversion by proposing a gradient descent optimization-based inversion technique to predict the unknown model properties (P- and S-wave velocities, the related quality factors, and density). The proposed inversion minimizes the non-linear least-squares misfit with the observed data. The optimal solution is iteratively obtained by optimizing the data misfit using a second-order limited-memory quasi-Newton technique. The forward model is performed in the frequency-frequency-angle domain based on a convolution of broadband signals and a linearized viscoelastic frequency-dependent amplitude versus offset (FAVO) equation. The optimization includes the adjoint-state-based gradients with the Lagrangian formulation to improve the efficiency of the non-linear seismic FAVO inversion process. The inversion is tested on synthetic seismic data, in 1D and 2D, with and without noise. The sensitivity for seismic quality factors is evaluated using various rock physics models for seismic attenuation and quality factors. The results demonstrate that the proposed inversion method reliably retrieves the unknown elastic and an-elastic properties with good convergence and accuracy. The stability of the inverse solution especially seismic quality factors estimation relies on the noise level of the seismic data. We further investigate the uncertainty of the solution as a function of the variability of the initial models.

Keywords: Rock Physics and AVO inversion; Marine geosciences and applied geophysics; Inverse theory; Seismic attenuation; Numerical modelling; Joint inversion

4.2 Introduction

Seismic waves propagation through the geological layers leads to the amplitude loss of coherent wave-front due to absorption and transmission caused by numerous elastic and an-elastic subsurface mechanisms (Kneib and Shapiro 1995; Wang 2019). The energy absorption effect also referred to as seismic attenuation, is measured by the inverse of the quality factor (Q), which can thus be estimated, for example, from the amplitude decay of seismic waves. The energy loss might depend on the heterogeneity of rock and pore fluid properties which can cause both scattering and wave-induced fluid flow (Carcione and Picotti 2006; Caspari et al. 2019; Chapman et al. 2021; Mavko et al. 2020; Pride and Berryman 2003a; Pride and Berryman 2003b; Pride et al. 2004; Tisato and Quintal 2013; White 1975). Seismic wave attenuation caused by such physically-based mechanisms is frequency dependent and can be approximated by a viscoelastic model (Jänicke et al. 2019; Jänicke et al. 2015).

At a geological horizon between two viscoelastic interfaces, the seismic reflection

amplitude variations depend on the P- and S- wave quality factors together with P- and S- wave velocities and density (Innanen 2011; Li and Liu 2019; Zhao et al. 2014a). In viscoelastic media, seismic waves exhibit dispersion, and thereby the magnitude of reflection amplitudes is not only dependent on the medium properties and incident angles but are also strongly affected by the frequency (Chapman et al. 2006; Jin et al. 2017; Kumar et al. 2020). Therefore, the estimation of both seismic quality factors along with elastic properties can give valuable information regarding the earth's subsurface properties, such as temperature, pressure, lithology, and fluid content (Chen et al. 2018; Cheng 2013; Li and Liu 2019; Peters et al. 2012; Sheehan et al. 2014; Zong et al. 2015). Numerous studies (Carcione 2007; Chapman et al. 2021; Pride et al. 2004; Tisato and Quintal 2013) have shown that the wave-induced fluid flow (WIFF) is the dominant source of seismic waves attenuation in partially fluid-saturated sediments in the seismic frequencies range, i.e. at the mesoscopic scale. The seismic energy attenuation can have a substantial impact on the seismic reflectivity and hence can provide additional information regarding pore fluids saturation (Dvorkin and Mavko 2006; Mavko et al. 2005; Mavko et al. 2020; Quintal et al. 2009; Quintal et al. 2011; Zhao et al. 2014a).

The frequency-dependent amplitude versus offset (FAVO) inversion method is used to estimate seismic velocities and quality factors from pre-stack seismic gathers of partially fluid-saturated reservoirs where higher attenuation of seismic waves is observed. Innanen (2011) carried out a direct AVO inversion process for an-elastic targets from a single absorptive reflectivity event. Teng et al. (2012) presented a viscoelastic AVO inversion method by using the Bayesian approach to estimate the seismic wave quality factors and velocities from the imaginary component of pre-stack seismic gathers. Zong et al. (2015) proposed an inversion strategy for P- and S- quality factors from complex seismic data. Chen et al. (2018) developed a frequency-dependent AVO approximation and a Markov Chain Monte Carlo (MCMC) inversion to predict inverse seismic quality factors and attenuative seismic impedances. Li and Liu (2019) derived a decoupled viscoelastic AVO equation based on the Aki and Richards (2002) nearly constant Q models which relate the dispersion of P- and S- wave velocities to the P- and S- wave quality factors. To avoid decoupling effects in the inversion results due to the simultaneous inversion of multi-parameters, they invert only for P- and S- wave quality factors and density under the assumption of known P- and S- wave velocities at a dominant frequency in the an-elastic medium. However, the inversion process given by Li and Liu (2019) does not take into consideration seismic velocity dispersion effects. Recent advances in frequency-dependent AVO studies and FWI in viscoelastic media include (Cheng et al. 2020; Cheng et al. 2022; JafarGandomi and Takenaka 2013; Keating and Innanen 2020; Li et al. 2021; Liu et al. 2022; Pan et al. 2020; Pan and Wang 2020; Pang and Stovas 2020; Yang et al. 2020); however, the use of the adjoint-state method for non-linear optimization with analytical solutions for the partial derivatives of the gradient of the misfit function for FAVO inversion has not been yet presented.

In this research work, we propose a novel inversion scheme that is a constrained non-linear frequency-dependent AVO algorithm that relies on Li and Liu's (2019) linearized viscoelastic equation. We first develop a generalized seismic forward model for the frequency-angle dependent reflectivity time series by performing a 1D Fourier transform from frequency-time-angle to frequency-frequency-angle. Then, we apply a gradient descent optimization-based inversion method to iteratively minimize the

least-squares misfit function that defines the distance between the forward synthetic model and the observed data. Gradient-based numerical optimization algorithms are highly efficient thanks to the implementation of the adjoint-state method (Plessix 2006) to calculate the gradient. The adjoint-state method is widely used in non-linear inverse geophysical problems (Ahmed and Weibull 2022; Ahmed et al. 2022; Fabien-Ouellet et al. 2017; Guo et al. 2022; Wang et al. 2021b; Yong et al. 2022) and provides the analytical gradient solution more efficiently than the finite difference approximation. For this reason, the adjoint-state method is applied to differentiate the misfit function with respect to the set of viscoelastic AVO variables. We then adopt the chain rule of derivatives to obtain the gradient equations for the P- and S- wave quality factors. For model updating at every non-linear iteration step, we apply the limited-memory BFGS algorithm (Nocedal and Wright 2006) to define the descent search direction for the data misfit minimization towards the local minima. L-BFGS is a second-order algorithm for numerical optimization that refers to the class of quasi-Newton methods. L-BFGS performs numerical optimization for large-scale problems very efficiently.

The novelty of the presented inversion process is the analytical derivation of the adjoint-state solution to find the gradient of data misfit with respect to the viscoelastic AVO variables. Furthermore, unlike the Li and Liu (2019) approach, the gradients of seismic (P- and S-) wave velocities also depend on the frequency and therefore may incorporate the possible velocity dispersion. To validate the FAVO non-linear inversion process, we test the proposed methodology using synthetic data computed from borehole sonic measurements. The direct measurements of seismic wave quality factors during wireline logging are problematic. Therefore, various rock physics models, such as Waters empirical relationships, constant Q models, and frequency-dependent White analytical solution (Dvorkin and Mavko 2006; Li and Liu 2019; Mavko et al. 2020; Quintal et al. 2009; Waters and Waters 1981; White et al. 1975), are applied to compute the reference seismic quality factors.

4.3 Theory and method

4.3.1 Viscoelastic FAVO model

A frequency-dependent reflectivity equation that is a function of seismic velocities, quality factors, and density is used to estimate the viscoelastic subsurface properties. In the viscoelastic geological medium, the seismic wave velocity exhibits a dispersion behavior. Therefore, the reflection coefficients also relate to seismic frequency rather than only incident angles. We implement a forward modeling approach in the frequency domain with the help of a Fourier transform to do convolution in the frequency-frequency-angle domain in order to compute the broadband viscoelastic seismic gather of multilayer dispersive media.

We use the frequency-dependent AVO approximation derived by Li and Liu (2019) for the forward model in the viscoelastic isotropic media. The reflectivity equation in the frequency-time-angle (ω', t, θ) domain is given by:

$$R_{PP}(t,\,\theta,\,\omega_o,\,\omega') = A(\theta)\,\frac{\Delta V_P(t,\,\omega_o)}{V_P(t,\,\omega_o)} + B(t,\,\theta)\,\frac{\Delta V_S(t,\,\omega_o)}{V_S(t,\,\omega_o)} + C(t,\,\theta)\,\frac{\Delta\rho(t)}{\rho(t)} + D(\theta,\,\omega_o,\,\omega')\,\frac{\Delta\xi_P(t)}{\xi_P(t)} + E(t,\,\theta,\,\omega_o,\,\omega')\,\frac{\Delta\xi_S(t)}{\xi_S(t)} \tag{4.1}$$

where,

$$A = \left[\frac{1}{2}\left(1+\tan^2\theta\right)\right], \qquad B = \left[-\frac{4\beta^2}{\alpha^2}\,\sin^2\theta\right], \qquad C = \frac{1}{2}\left[1-\frac{4\beta^2}{\alpha^2}\,\sin^2\theta\right]$$

and

$$D = \left[-\frac{1}{2}(1+\tan^2\theta)\,\frac{1}{\pi}\,\ln\left(\frac{\omega_o}{\omega'}\right)\right], \qquad E = \left[\frac{4\beta^2}{\alpha^2}\,\sin^2\theta\,\frac{1}{\pi}\,\ln\left(\frac{\omega_o}{\omega'}\right)\right]$$

whereas, ω_o refers to the reference angular frequency, while V_P and V_S are the seismic wave phase velocities at an angular reference frequency ω_o and ρ is density. In equation 4.1, the denominators represent the average values of elastic and an-elastic properties whereas the Δ-terms are the differences across the viscoelastic geological boundaries. In the forward modeling equation, it is assumed that the medium above and below the interface is viscoelastic and dissipative. The terms ξ_P and ξ_S are defined as functions of both compressional and shear Q-factors, Q_P, and Q_S, as:

$$\xi_P(t) = 1+\frac{1}{Q_P(t)}, \qquad \xi_S(t) = 1+\frac{1}{Q_S(t)}$$

Seismic quality factors are not measured directly during borehole logging and are thus computed using empirical equations as in (Li 2017; Waters and Waters 1981) or rock physics models such as Dvorkin-Mavko nearly constant Q approximations (Dvorkin and Mavko 2006; Mavko et al. 2020) and the frequency-dependent White's analytical solution (Quintal et al. 2009; White et al. 1975). The rock physics formulations for the quality factors are given in Appendix A.

4.3.2 Viscoelastic FAVO inversion

The aim of the FAVO inverse modeling is to retrieve the viscoelastic model properties i.e., $m = (V_P, V_S, \rho, Q_P, Q_S)$ based on the broadband seismic data $d(t,\,\omega',\,\theta)$. We first set up the formulation of the seismic FAVO inverse process as the minimization of a differentiable error function J with respect to m using the least-squares error between seismic data (d) and forward model predicted data $f(m)$.

Let j, p, and n be the maximum number of reflection interfaces, broadband frequencies ranges, and corresponding incident angles, then the data misfit equation is given by:

$$\min J(m) = \min \frac{1}{2}\sum_{t=1}^{j}\sum_{\omega'=1}^{p}\sum_{\theta=1}^{n} \parallel d(t,\,\theta) - f(m(t,\,\theta)) \parallel^2 \qquad \text{over} \qquad C \tag{4.2}$$

where forward model $f(m)$ is the time-domain convolution after applying the inverse Fourier transform.

$$f(m(t,\,\theta)) = \mathcal{F}^{-1} \sum_{\omega'=1}^{p} \left[W(\hat{\omega}) \cdot R_{PP}(t,\,\theta,\,\hat{\omega},\,\omega')\delta(\omega' - \hat{\omega}) \right] \tag{4.3}$$

whereas, δ represents Dirac's delta function.

In non-linear inverse optimization, an initial guess for the model properties V_P, V_S, ρ, Q_P, and Q_S is required to iteratively update the solution, together with a set of constraints to set their physical boundaries:

$$C = \{m = (V_P,\, V_S,\, \rho,\, Q_P,\, Q_S) \mid m_{min} \;\leq\; m \;\leq\; m_{max}\} \tag{4.4}$$

The gradient of the data misfit J described in equation 4.2 is the vector of partial derivatives of the misfit error J in respect of model properties m as given:

$$\nabla J = \left[\frac{\partial J}{\partial V_P}, \frac{\partial J}{\partial V_S}, \frac{\partial J}{\partial \rho} \frac{\partial J}{\partial Q_P}, \frac{\partial J}{\partial Q_S} \right] \tag{4.5}$$

and the solution of misfit J with respect to $m = [V_P,\, V_S,\, \rho,\, Q_P,\, Q_S]$ is.

$$\frac{\partial J}{\partial m} = -\Big[d - f(V_P,\, V_S,\, \rho,\, Q_P,\, Q_S) \Big] \cdot \frac{\partial f}{\partial m} \tag{4.6}$$

In practical applications, viscoelastic seismic properties are discretized at the interfaces $i = 1, \ldots\, i_n$ in the time (or depth) domain. Therefore, in the following, we adopt the discretized notation for all the model variables

$$m = [V_{P1},\, ...,\, V_{Pi_n},\, V_{S1},\, ...,\, V_{Si_n},\, \rho_1,\, ...,\, \rho_{i_n},\, Q_{P1},\, ...,\, Q_{Pi_n},\, Q_{S1},\, ...,\, Q_{Si_n}]^T$$

4.3.3 Adjoint-state method and L-BFGS

The adjoint-state method provides an effective numerical approach to computing the gradient of the non-linear least-square data misfit that relies on a set of state variables without computation of the Fréchet derivatives. The adjoint solution is implemented here by introducing the augmented Lagrangian function $\mathcal{L}$ as:

$$\begin{aligned} \mathcal{L}\,(V_P,\, V_S,\, \rho,\, \xi_P,\, \xi_S,\, R_{PP},\, \lambda\,) &= \sum_i \int_\theta d\theta \Big[d[i] - f[i] \Big]^2 \\ + \sum_i \int_{\theta,\,\omega} d\theta \Big[R_{PP}[i] - A[i]\, \frac{\Delta\alpha}{\alpha} - B[i]\, \frac{\Delta\beta}{\beta} - C[i]\, \frac{\Delta\rho_0}{\rho_0} - D[i]\, \frac{\Delta\Xi_P}{\Xi_P} - E[i]\, \frac{\Delta\Xi_S}{\Xi_S} \Big]\, \lambda_{[i]} \end{aligned} \tag{4.7}$$

where λ refers the adjoint-state variable, R_{PP} denotes the state variable and forward model f is given by the equation 4.3. The Lagrangian function in equation 4.7 can be reformulated as $\mathcal{L} = J(R_{PP},\, m) + C(R_{PP},\, m) * \lambda$, where the constraint (C) in the Lagrangian formalism is automatically satisfied by:

$$[R_{PP}[i] - A[i]\ \frac{\Delta\alpha}{\alpha} - B[i]\ \frac{\Delta\beta}{\beta} - C[i]\ \frac{\Delta\rho_0}{\rho_0} - D[i]\ \frac{\Delta\Xi_P}{\Xi_P} - E[i]\ \frac{\Delta\Xi_S}{\Xi_S}\Big] = 0 \tag{4.8}$$

In equation 4.7, the denominators indicate the average values at the interfaces and the numerators are the differential values across the interfaces. To make the derivation of the gradient solution of the Lagrangian of the misfit function ease for ourselves, we replace the seismic velocities, density, and quality factor terms in equation 4.7 with α, β, ρ_0, Ξ_P and Ξ_S which are related to the model variables m as:

$$\alpha[i] = \frac{V_P[i+1] + V_P[i]}{2} \qquad \Delta\alpha[i] = V_P[i+1] - V_P[i]$$

$$\beta[i] = \frac{V_S[i+1] + V_S[i]}{2} \qquad \Delta\beta[i] = V_S[i+1] - V_S[i]$$

$$\rho_0[i] = \frac{\rho[i+1] + \rho[i]}{2} \qquad \Delta\rho_0[i] = \rho[i+1] - \rho[i]$$

$$\Xi_S[i] = \frac{\xi_S[i+1] + \xi_S[i]}{2} \qquad \Delta\Xi_S[i] = \xi_S[i+1] - \xi_S[i]$$

$$\Xi_P[i] = \frac{\xi_P[i+1] + \xi_P[i]}{2} \qquad \Delta\Xi_P[i] = \xi_P[i+1] - \xi_P[i]$$

The gradient solution of the data misfit is achieved by solving the subsequent adjoint-state equations:

$$\frac{\partial\mathcal{L}}{\partial R_{PP}} = 0, \qquad \frac{\partial\mathcal{L}}{\partial\lambda} = 0 \tag{4.9}$$

The analytical formulation of the partial derivatives is given in Appendix B.

When the adjoint equations 4.9, the partial differentials of the Lagrangian function in respect of viscoelastic R_{PP} and state variable λ are satisfied, i.e. equal to 0. Then the partial derivatives coincide with:

$$\frac{\partial\mathcal{L}}{\partial\cdot} = \frac{\partial J}{\partial\cdot}$$

where $\cdot$ represents one of the five unknown variables m.

Then the partial derivatives with respect to P- and S- quality factors are acquired using the chain rule derivative:

$$\frac{\partial J}{\partial Q_P[i]} = \frac{\partial J}{\partial\xi_P[i]} \cdot \frac{\partial\xi_P[i]}{\partial Q_P[i]} \tag{4.10}$$

$$\frac{\partial J}{\partial Q_S[i]} = \frac{\partial J}{\partial\xi_S[i]} \cdot \frac{\partial\xi_S[i]}{\partial Q_S[i]} \tag{4.11}$$

$$\frac{\partial\xi[i]}{\partial Q_P[i]} = -\frac{1}{Q_P^2[i]}, \qquad \frac{\partial\xi_S[i]}{\partial Q_S[i]} = -\frac{1}{Q_S^2[i]} \tag{4.12}$$

The model m, including the five unknown variables, is updated at every iteration using the second-order quasi-Newton L-BFGS optimization technique that iteratively approximates the inverse Hessian ($H^{(k)}$) based on the gradient values and the previous solution as:

$$m^{(k+1)} = m^{(k)} + \alpha^{(k)}[-H^{(k)}\nabla J], \tag{4.13}$$

whereas $m^{(k)}$ and $m^{(k+1)}$ are referred as the current and updated values and $\alpha^{(k)}$ is described as step length. The gradient descent search direction is determined by $[-H^{(k)}\nabla J]$. The L-BFGS procedure is described in Algorithm 1.

Algorithm 1 The standard L-BFGS algorithm

L-BFGS procedure
Choose a stating value $\mathbf{m}_0$, and integer $l > 0$
do k = 0, 1, 2, 3 ...
    Calculate data misfit value J and gradient ∇
    Compute the search direction $[-\mathbf{H}^{(k)}\nabla J]$ using L-BGFS two-loop recursion
    Find the step length $\alpha^{(k)}$ using line search algorithm
        First trial step length: $\alpha^{(0)} = l/\parallel \nabla^0 \parallel^2$, if k>**m** try $\alpha^{(k,0)} = 1$
        do $i = 0, 1, 2, 3 ..., l$
            Verify function minimization conditions
            Get new $\alpha^{(k,i+1}$ using line search algorithm
        End do
    Update $\mathbf{m}^{(k+1)} = \mathbf{m}^{(k)} + \alpha^{(k)}[-\mathbf{H}^{(k)}\nabla J]$
    Repeat until convergence
End procedure

The physics involving seismic wave velocities and corresponding seismic quality factors are coupled in the simultaneous viscoelastic inversion (Kamei and Pratt 2013). Consequently, the inverse solution of the estimation of the parameters in the presence of low-resolution noisy data is not unique and the prediction of velocities and quality factors might be inaccurate. The lack of model properties resolution is referred to as crosstalk or trade-off between the variables. Operto et al. (2013) present different strategies to reduce the coupling effect between optimized properties, such as the use of second order Hessian matrix, the selection of an appropriate parametrization, and a model-driven approach where the more sensitive variables are estimated before the least sensitive ones.

The linearized AVO equation for viscoelastic media relies on a set of five variables, i.e. P- and S- wave velocities, density, and the seismic quality factors (V_P, V_S, ρ, Q_P, Q_S). In this model, the crosstalk affects the following couples of variables: V_P and Q_P, V_S and Q_S, V_P and V_S and Q_P and Q_S. To examine the crosstalk effects between model variables, we run several tests and study the coupling effects between seismic velocities and quality factors at initial iterations as well as for low and high incident angles. In the first crosstalk test, we introduced two perturbations for P- and S- wave velocities (e.g., ΔV = 50 and 200 ms^{-1}) and computed the gradient of corresponding quality factors. In

theory, if the velocities and quality factors were independent, the perturbation in V_P or V_S with a constant corresponding Q_P and Q_S respectively should not affect the partial derivatives with respect to the quality factors. However, in reality, these parameters are not independent and the partial derivatives of the quality factors are affected by the velocity perturbation. Fig. 4.1 shows the results of the perturbation for the following couples: V_P and Q_P, V_S, and Q_S, by comparing the gradient results with and without perturbation. The results demonstrate that strong crosstalk exists between the variables, as a small perturbation in the seismic velocities results in a variation in the corresponding quality factors. We also investigate the crosstalk between V_P and V_S as well as Q_P and Q_S derived through a rock physics model by considering the WIFF mechanism. The perturbations are added to the compressional wave velocity and the related quality factor. The gradients of V_S and Q_S with and without perturbations are shown in 4.2 (right side panel). The gradients plotted in Figures 4.1 and 4.2 are scaled by different factors ranging between 10^3 and 10^5. The results show limited crosstalk between V_P and V_S and quality factors. Despite the large perturbation in the P wave quality factor, limited crosstalk between Q_P and Q_S is observed. Then, we study the crosstalk effects between two classes (V_P and Q_P, and V_S and Q_S) at low and high incident angles (Figures 4.3 and 4.4). The results show that the crosstalk between variables exists at different incident angles: for example, at the near offset, the coupling between V_P and Q_P is higher than the coupling between V_S and Q_S for large offset; this result is even more evident for the coupling between V_S and Q_S.

Due to the coupling between seismic velocities and corresponding quality factors, we adopt the strategy of inverting the most sensitive model variables first (V_P, V_S, and density) and then predicting the least sensitive properties (Q_P and Q_S). The crosstalk between V_P and V_S or Q_P and Q_S is limited; hence, it does not affect the inversion of seismic velocities at the first phase nor the inversion of the quality factors in the next step.

4.4 Applications

We present several applications with two synthetic datasets to verify the described FAVO inversion scheme by using the frequency-domain convolution of broadband signals. Dataset 1 represents a 1D vertical profile, whereas dataset 2 represents a 2D seismic section. In both examples, the quality factors have been computed from well logs using empirical and rock physics models (Appendix A).

In the first example, a 1D synthetic seismic forward model obtained from wireline logs in the Edvard Grieg field located in the North Sea is used. The quality factors are calculated using the empirical expressions given by equation 4.14. The reference model is upscaled at the seismic scale (Fig. 4.5). The seismic response with signal-to-noise ratio infinity and with seismic random noise level (S/N = 50) is shown in Fig. 4.6. Seismic reflection amplitudes are displayed up to the incident angle 30° with an interval of 5°. Fig. 4.7 to 4.10 present the results of the inversion scheme for the elastic and an-elastic properties. In the case of S/N = 0, the inversion method shows good convergence, and the estimated parameters are in close agreement with the reference properties (Fig.4.7) and 4.8). In the case of noisy data, the inversion method produces

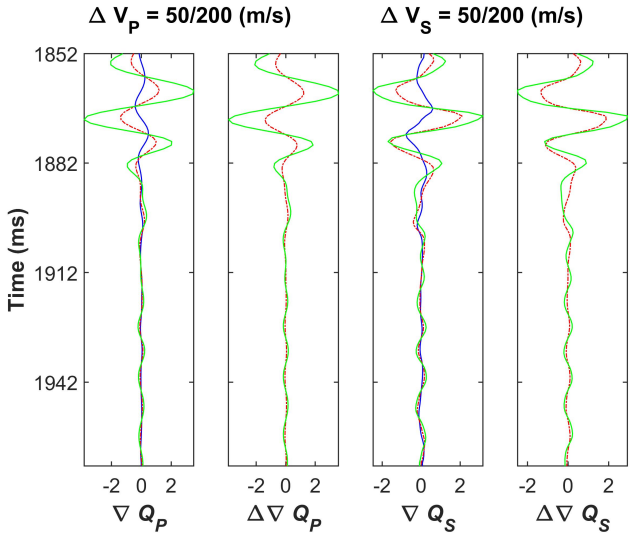

Figure 4.1: Crosstalk between elastic and an-elastic variables; V_P and Q_P, V_S and Q_S. The panels represent the gradients: red lines indicate a perturbation of 50 m/s, green lines indicate a perturbation of 200 m/s, and blue lines indicate no perturbation.

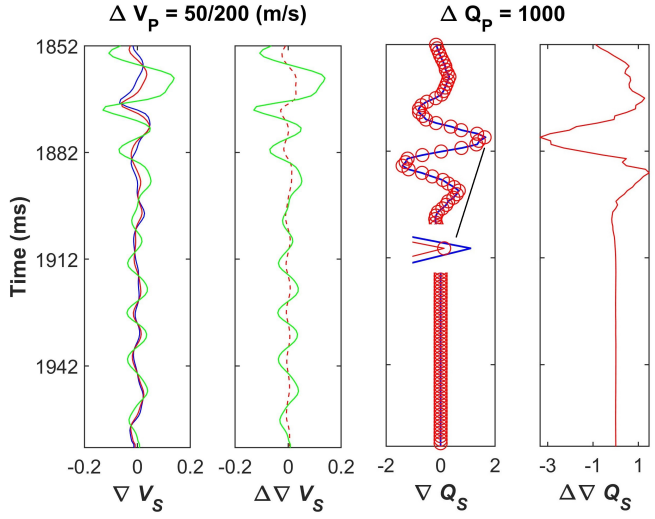

Figure 4.2: Crosstalk between elastic and an-elastic variables; V_P and V_S and Q_P and Q_S. The panels represent the gradients: red lines indicate a perturbation of 50 m/s, green lines indicate a perturbation of 200 m/s, and blue lines indicate no perturbation. The crosstalk between Q_P and Q_S is calculated based on the rock physics model.

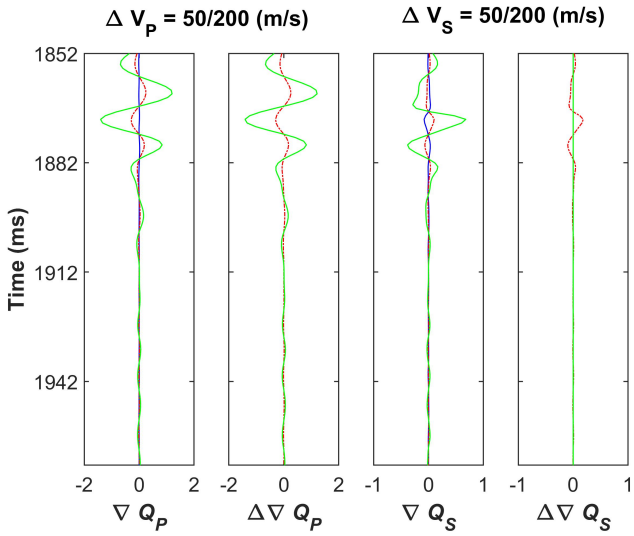

Figure 4.3: Crosstalk between elastic and an-elastic variables; V_P and Q_P, V_S and Q_S, at incident angles of $1-5^\circ$. The panels represent the gradients: red lines indicate a perturbation of 50 m/s, green lines indicate a perturbation of 200 m/s, and blue lines indicate no perturbation.

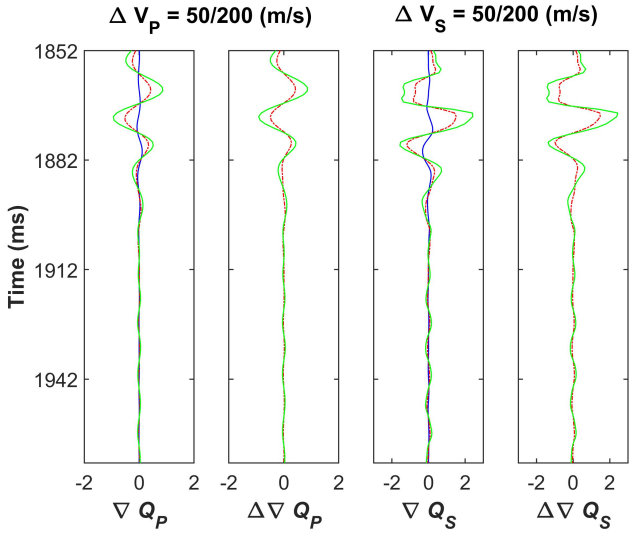

Figure 4.4: Crosstalk between elastic and an-elastic variables; V_P and Q_P, V_S and Q_S, at incident angles of $25-30^\circ$. The panels represent the gradients: red lines indicate a perturbation of 50 m/s, green lines indicate a perturbation of 200 m/s, and blue lines indicate no perturbation.

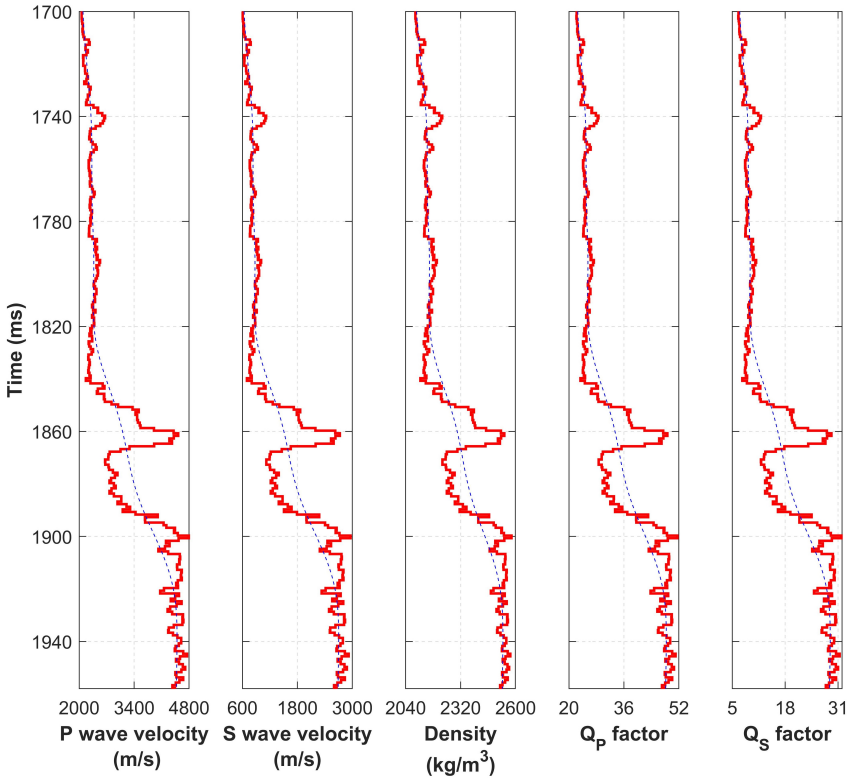

Figure 4.5: Example 1 - Reference model variables including P- and S- wave velocities, density, and P- and S- quality factors, with respective initial guesses.

stable results for P- and S- wave seismic velocities and density are consistent with the reference models, whereas the inversion of quality factors are more unstable and less accurate (Fig. 4.9 and 4.10). To reduce the instability of the solution, we apply small Tikhonov regularization weights (Aster et al. 2018), whereas the inaccuracy is due to noise in the seismic data and the limited sensitivity of the forward model.

In example 2, we applied the proposed non-linear inversion process on a 2D synthetic example mimicking faulted geological boundaries and inclined horizons. Seismic velocities interpreted in seismic velocity analysis during processing are used to generate a 2D visco-elastic model. The FAVO inversion process is implemented trace by trace in the entire time window (0 - 5000 ms). The resulting elastic and viscoelastic properties are shown in Fig. 4.11. The inverted P- and S- wave velocity, density, and the related seismic quality factors are accurately estimated. The initial Q factors are obtained by using the empirical expressions. The inversion produces some mismatches, especially in the density prediction, which can be partially compensated using Tikhonov regularization.

In the next examples, we focus on partially saturated reservoirs to investigate frequency-dependent mechanisms. A leading cause of seismic wave attenuation and velocity dispersion in partially fluid-saturated rock or sediments is WIFF. Fig. 4.12

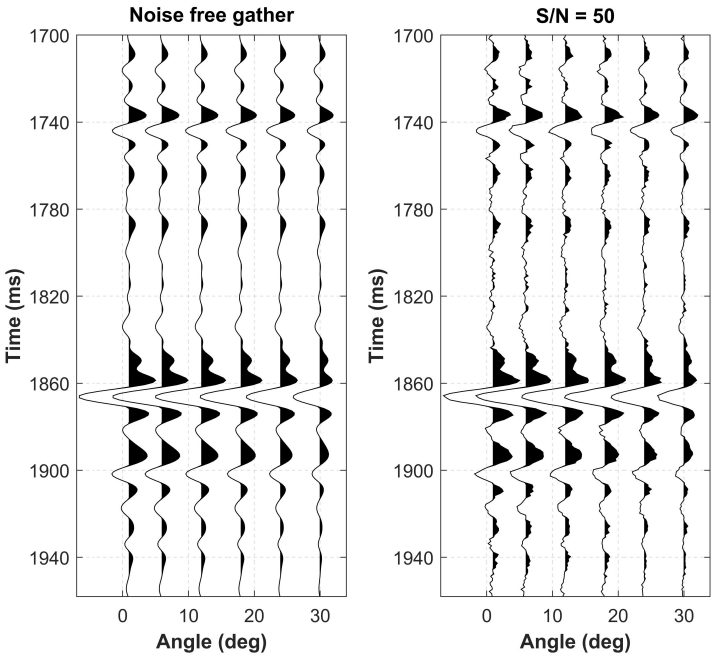

Figure 4.6: Example 1 - Synthetic seismic pre-stack gathers with different noise levels (no noise and S/N = 50) .

shows the P wave attenuation behavior in two cases when the magnitude of attenuation is estimated as frequency independent (constant Q model, Fig. 4.12a) and frequency-dependent (Fig. 4.12b and c) in a partially saturated rock. Partially saturated gas reservoirs exhibit higher attenuation compared to oil and water. Furthermore, partially saturated reservoirs exhibit the P wave energy dissipation which also varies as a function of seismic frequencies. In the next examples, we adopt a rock physics model for seismic (P- and S-) wave attenuation due to WIFF in an oil-water system.

In example 3, we first adopt a simple physically-based model with constant Q (equations 4.15 to 4.18) which allows for estimating the P- and S- wave attenuation from the well logging curves. This model provides reasonable attenuation curves without considering frequency-dependence effects and can be easily incorporated into the seismic model (Dvorkin and Mavko 2006). The model example in Fig. 4.13 is taken from the Edvard Grieg oil field located in the North Sea. The reservoir zone (1865 - 1888 ms) has a partial oil saturation of about 66 %. Fig. 4.13(a - d) shows the water saturation curve and the computed attenuation curves in the corresponding zones. The calculated P-wave attenuation due to WIFF is shown in Fig. 4.13b. The partially oil-saturated zone displays higher attenuation due to partially fluid saturation heterogeneities e.g., the seismic energy loss in the oscillatory pore-fluid flow induced by the passage of waves. The seismic wave passage induces fluid pressure gradients which cause the fluid flow between softer-stiffer fluid patches, which then results in

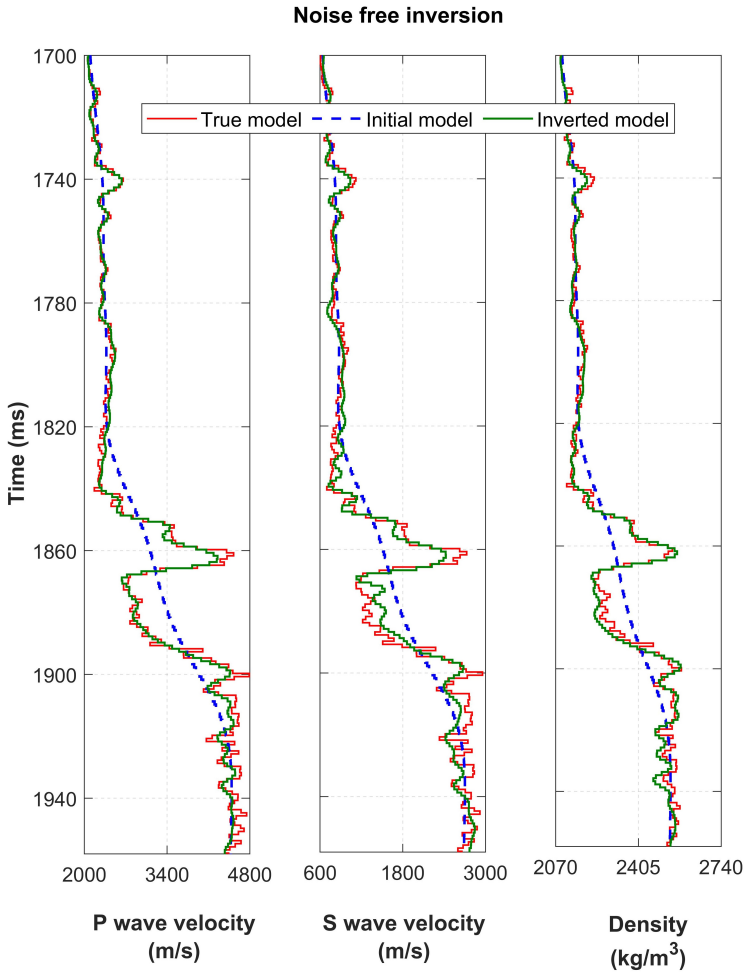

Figure 4.7: Example 1 - Inverted model variables including P- and S- wave velocities, density for the noise-free case.

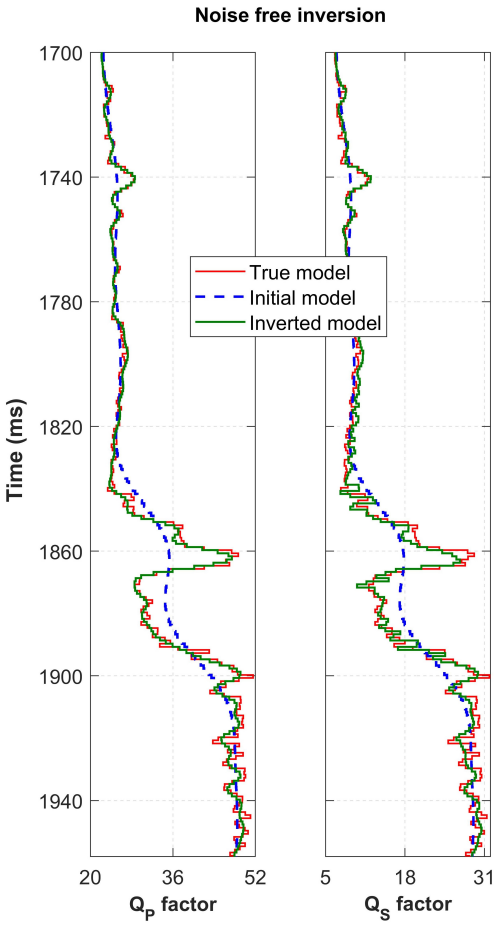

Figure 4.8: Example 1 - Inverted model variables including P- and S- wave quality factors for the noise-free case.

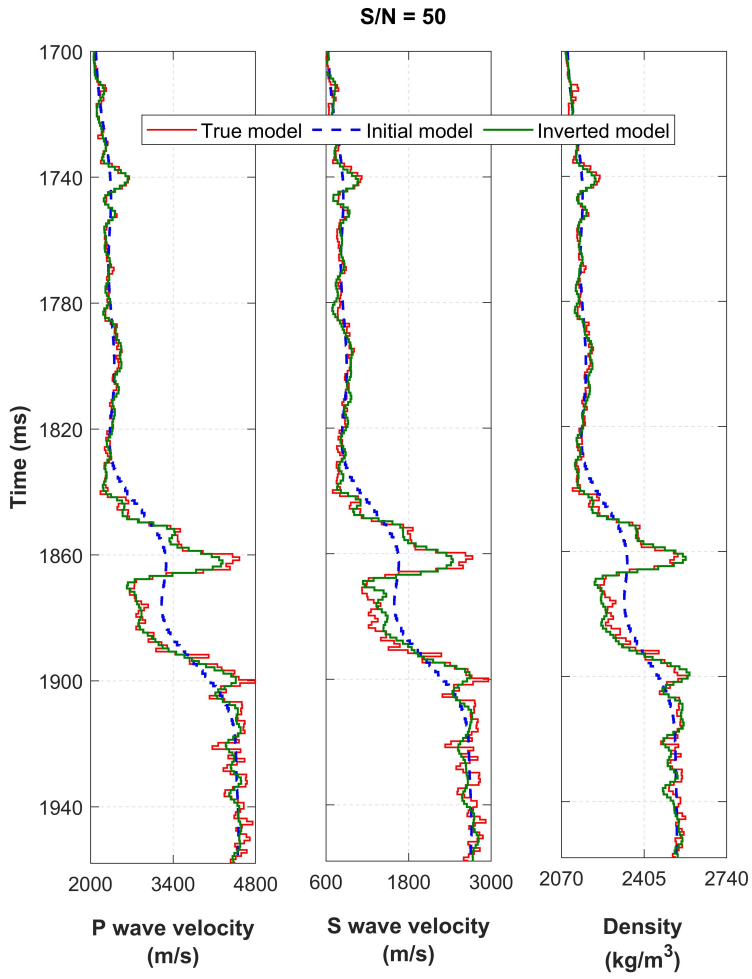

Figure 4.9: Example 1 - Comparison of initial and inverted properties estimated from the noisy seismic data.

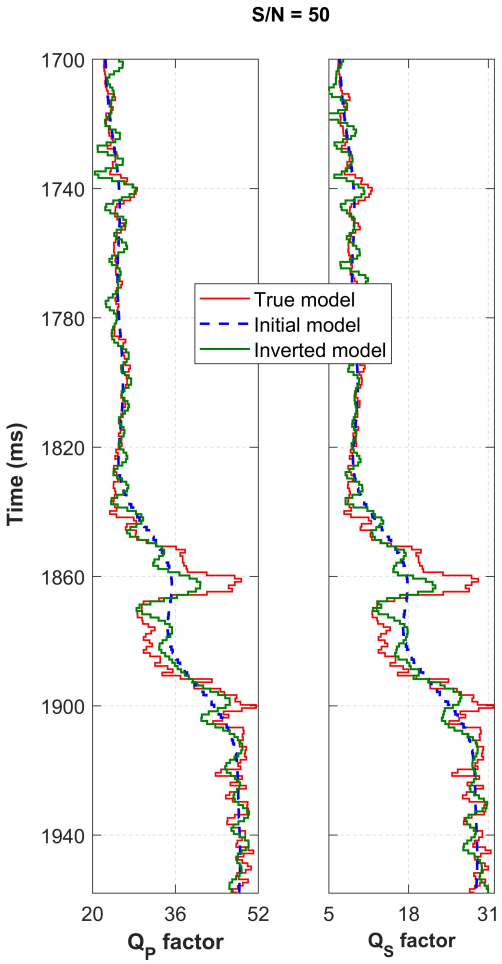

Figure 4.10: Example 1 - Comparison of initial and inverted properties estimated from the noisy seismic data.

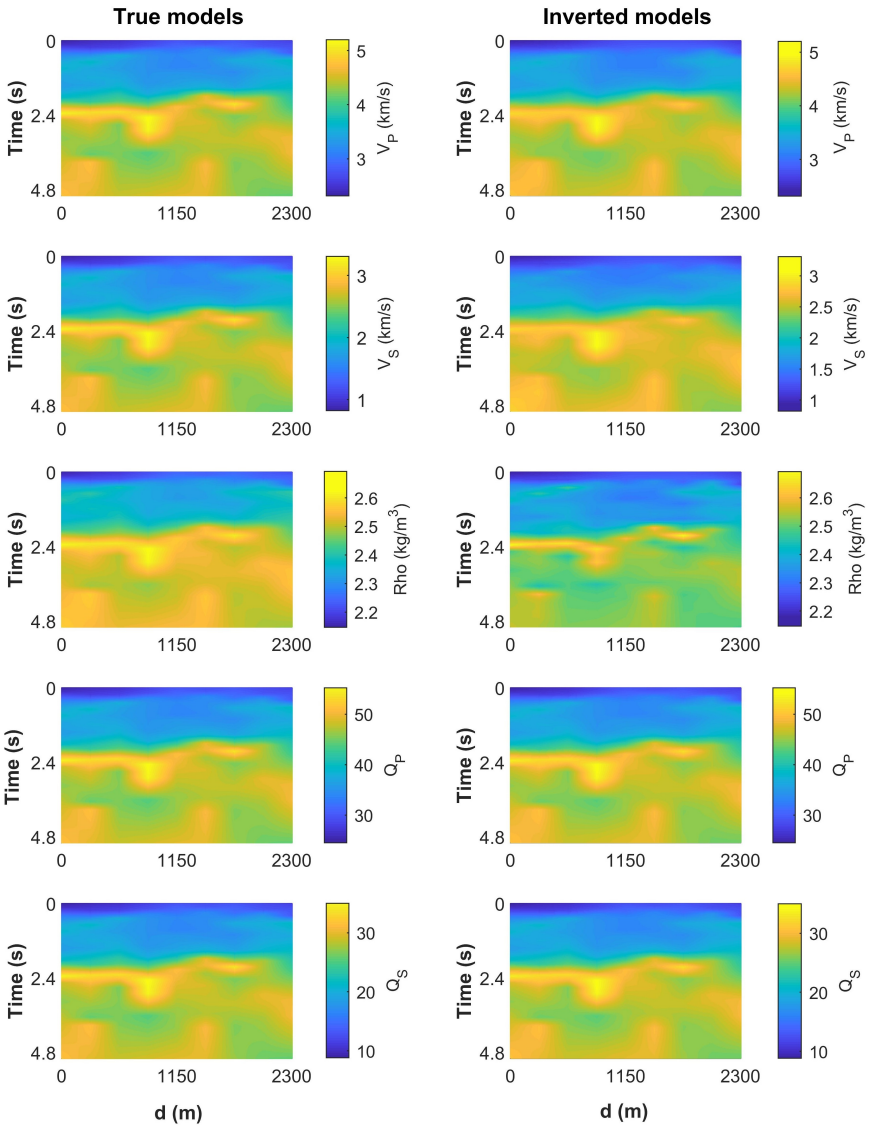

Figure 4.11: Example 2 - Reference model variables (left) and inverted variables (right) including P- and S- wave velocities, density, and P- and S- quality factors.

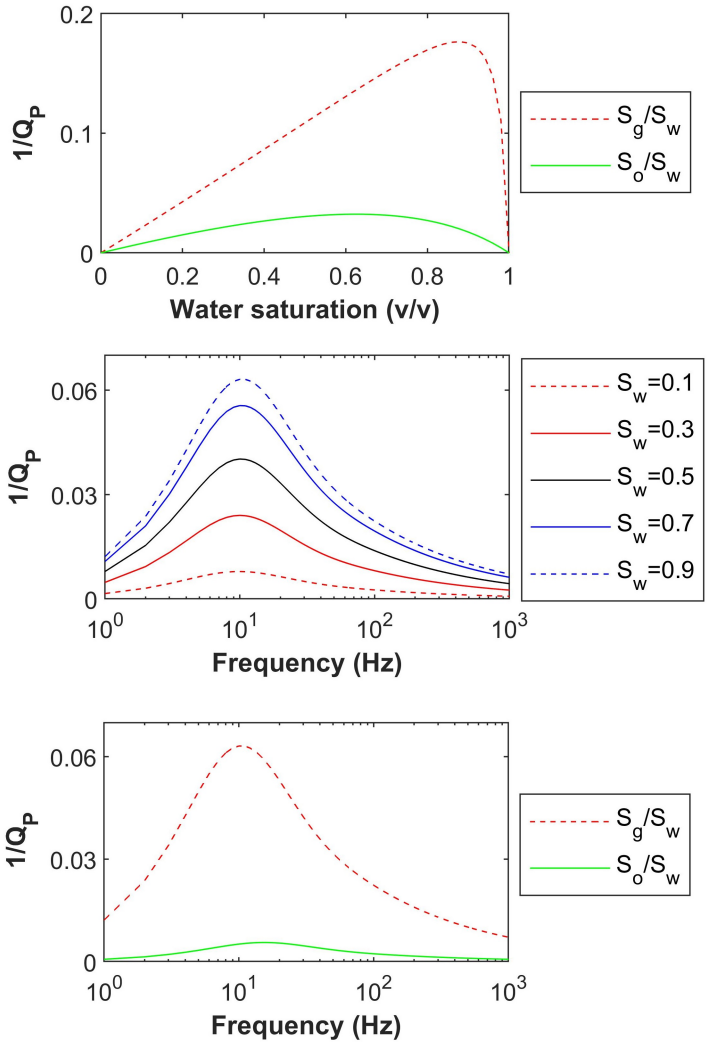

Figure 4.12: P- wave attenuation results: (top) P- attenuation as a function of water saturation estimated by using nearly constant Q-model (red dashed line for the gas-water case and solid green line for the oil-water case); (middle) P- attenuation as a function of frequencies at different gas/water saturation computed at mesoscopic scale using White's analytical solution; and (bottom) P- attenuation for the gas-water and oil-water cases as a function of frequency in the case of $S_w = 0.9$ at the mesoscopic scale.

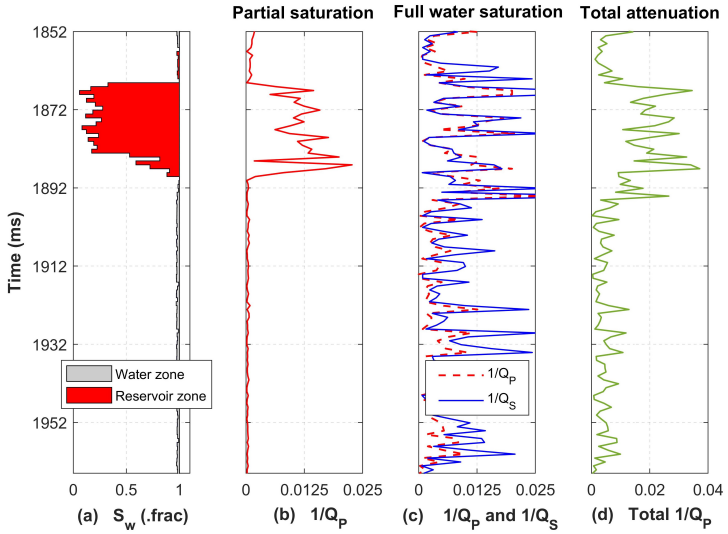

Figure 4.13: Example 3 - Water saturation (a) and corresponding P- wave attenuation (b-d): (b) attenuation due to pore fluid heterogeneities in partially saturated rocks; (c) attenuation due to pore fluid heterogeneities in fully water-saturated rocks; (d) the total attenuation due to both fluid and solid frame heterogeneities.

viscus-friction losses. The Q_P^{-1} is approximately zero in the water zone as low and high limit moduli become equal. Fig. 4.13c shows both the theoretical P- and S- wave attenuation curves for fully water-saturated rocks, where the attenuation depends on the heterogeneities of both fluid and the solid phase. The P-wave attenuation shown in Fig. 4.13d accounts for attenuation due to partial fluid saturation, full water saturation, and solid frame heterogeneities. The corresponding quality factors (Q_P and Q_S) are shown in Fig. 4.14. The properties used in the rock physics model are given in Table 4.1.

We then apply the inversion method to estimate the energy dissipation from the seismic frequency-angle gather. The seismic response up to 30° with intervals of 5° (Fig. 4.14a) together with initial guesses and true models for Q_P and Q_S are shown in Fig. 4.14b. The inversion results are shown in Fig. 4.14c: the P-wave quality is accurate whereas there is a mismatch between the S-wave quality factor predictions, possibly because of the low sensitivity of the seismic data to the shear wave attenuation due to rock-fluid inhomogeneities.

In example 4, we test the inversion workflow for the frequency-dependent mesoscopic loss which is responsible for the P- wave seismic energy dissipation mechanisms at seismic frequencies range (Tisato and Quintal 2013). The magnitude of the seismic energy attenuation is associated with both characteristics of the reservoir strata and of the fluid within pores (Carcione and Picotti 2006). We model the frequency-dependent Q_P based on White's analytical solution (Appendix A) at various vertical locations by using the well log data with the parameters given in Table 4.1. We then apply the inversion technique to invert the seismic frequency-dependent P-wave quality factors.

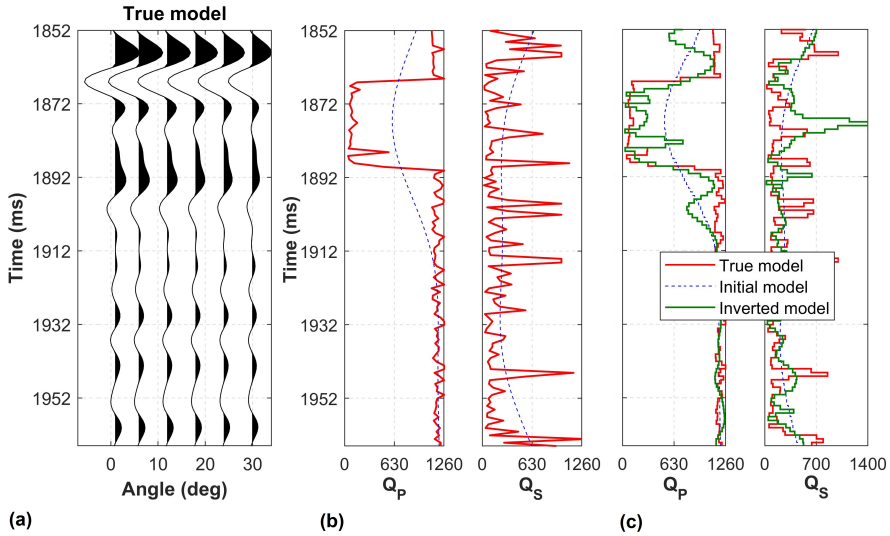

Figure 4.14: Example 3 - Seismic response up to the incident angle 30 (a), P- and S-wave quality factors calculated from the attenuation logs given in Fig. 4.13 (b), and the inverted P- and S- wave quality factors estimated by using constant Q rock physics models (c). The solid red curves are the reference models and the dashed blue curves represent the initial models.

The results for a subset of frequencies are shown in Fig. 4.15 in the partially saturated reservoir zone. The inverted Q_P curves are in good agreement with the reference models, especially at lower frequencies. Fig. 4.16 shows a comparison of the theoretical P-wave attenuation computed from White's model and the predicted P-wave attenuation estimated with the inversion method, which has been made for a broad range of seismic frequencies and demonstrates a high good correlation. This shows the efficiency of the inversion process to estimate the fluids-related attenuation from seismic gather. Thus, our proposed inversion method can be used to locate partially hydrocarbon zones. At higher frequencies, the FAVO inversion overestimates the P wave attenuation but the difference in magnitude is small.

Finally, we propose an uncertainty quantification study where we investigate the uncertainty of the solution as a function of the variability of the initial model. The uncertainty is quantified using a Monte Carlo simulation where we generate a set of initial models and predict the corresponding set of posterior solutions. The variability of the posterior ensemble of solutions is used to investigate the uncertainty propagation with respect to the initial uncertainty. We first generate a set of 75 initial models of the five unknown model variables by sampling from a multivariate Gaussian distribution estimated from the well logs of the properties. The initial models are simulated according to a spatial correlation model (Grana et al. 2021) estimated from the well log (Fig. 4.17). We then apply the proposed inversion method to each initial realization to obtain the distribution of the inverted models (Fig. 4.18). The uncertainty in the inverted models

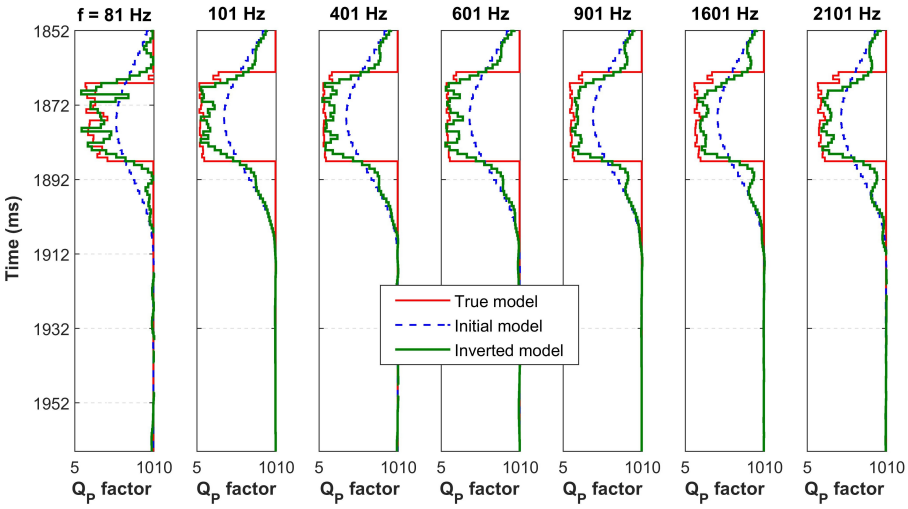

Figure 4.15: Example 4 - Inverted Q_P at different frequencies together with reference and initial models. The inversion results show a good correlation with the true models.

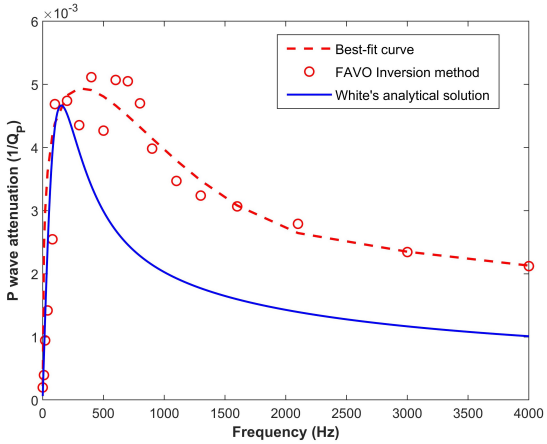

Figure 4.16: Example 4 - Comparison of P-wave attenuation curves computed using approximated White's analytical solution (blue curve) and the proposed FAVO inversion method (red curve).

Table 4.1: The reservoir rock and fluid parameters used in rock physics models, based on lab measurements and literature values (Mavko et al. 2020).

Parameters	Average values
Effective porosity (ϕ)	0.26
Permeability (k)	50*mD
Bulk modulus of quartz	37 (GPa)
Bulk modulus of clay	21 (GPa)
Shear modulus of quartz	44 (GPa)
Shear modulus of clay	7 (GPa)
Layer 1 thickness (d_1)	0.20 (m)
Layer 2 thickness (d_2)	0.50 (m)
Temperature (T)	78.18 ($^\circ C$)
Pressure (P_e)	26 (MPa)
Oil API	35
Gas/oil ratio (GOR)	145.7
Density of water (ρ_o)	987 (kg/m^3)
Density of oil (ρ_o)	821 (kg/m^3)
Bulk modulus of oil (K_o)	1.04 (GPa)
Bulk modulus of water (K_o)	2.55 (GPa)
Water viscosity (η_w)	0.001 (Pa.s)
Oil viscosity (η_o)	0.11 (Pa.s)

of the model variables is relatively narrow despite the large variability in the initial realizations, which shows that the presented inversion scheme is very stable and precise.

4.5 Discussion

The proposed inversion is relying on the gradient descent method which requires the computation of the first-order gradients of the data misfit in respect of the unknown model variables. By defining the Lagrangian formulation, we derive the adjoint solutions and the gradients of the data misfit function, leading to a more efficient algorithm compared to the classic non-linear inverse theory. Furthermore, the optimal solution is obtained by minimizing the misfit function iteratively and by using the non-linear L-BFGS optimization method.

Global optimization is often used in seismic inverse modeling (Sen and Stoffa 2013) thanks to its ability to explore the model space and avoid local minima; however, for the proposed seismic inverse problem, local optimization can produce results comparable to global optimization with a lower computational cost, as seismic data provide relative information about the property contrasts at the interfaces and the solution is expressed as a perturbation of the low-frequency model. Because of the seismic noise and the band-limited nature of the seismic data, the solution is not unique and the objective function might include several local minima. For this reason, we propose a sensitivity study on the initial guess of the inversion to investigate the variability of the solution with respect to the initial models. On the other hand, the Bayesian methods for seismic

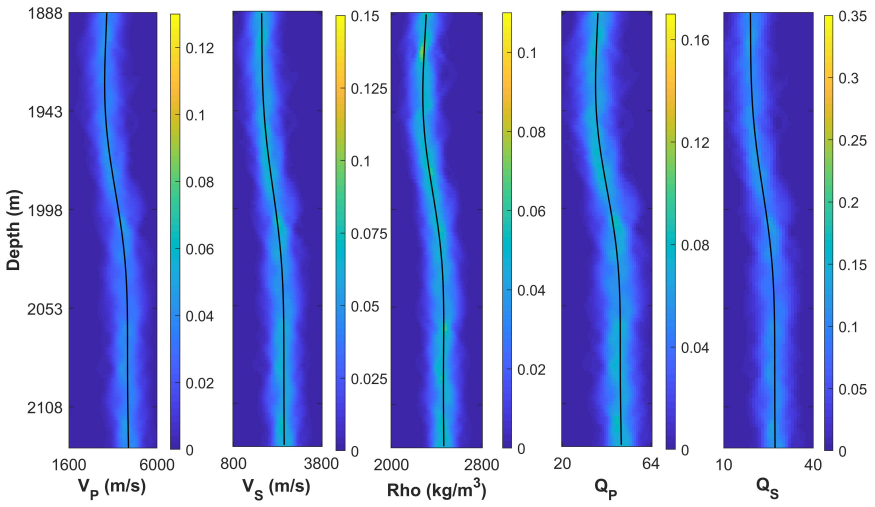

Figure 4.17: Initial realizations of P wave velocity, S wave velocity, density, P, and S wave quality factors. The mean of the initial models is also shown in black color.

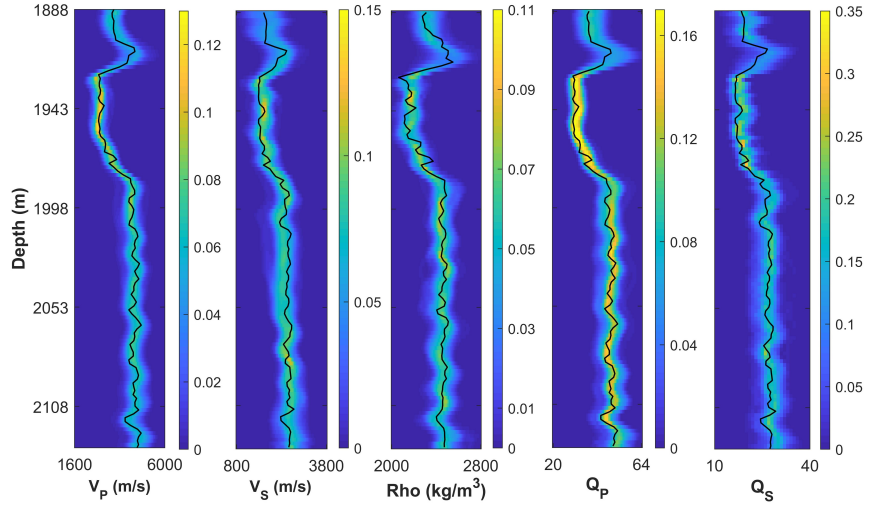

Figure 4.18: Inverted realizations of P wave velocity, S wave velocity, density, P, and S wave quality factors. The black solid lines represent the true reference model.

inverse problems (Avseth et al. 2010; Buland and Omre 2003b; Doyen 2007; Grana et al. 2021; Mosegaard and Tarantola 1995; Sen and Stoffa 1996) can be extended to viscoelastic inversion; however, the computational efficiency of the Bayesian inverse methods generally requires assumptions on the linearization of the forward model and the Gaussian distribution of the model variables. In the Bayesian context, Monte Carlo simulation methods can also be applied for non-linear inverse problems with complex prior models (Cordua et al. 2012; Figueiredo et al. 2019), but the application to large geophysical datasets is generally not feasible because of the spatial correlation of the model variables (Grana et al. 2022).

The forward model is relying on the frequency-angle dependent linearized AVO equation derived from constant Q models for the P- and S- wave quality factors, where the seismic response depends on the incident angles and the seismic frequencies. In the objective function of the inversion, we did not apply weights associated with angles nor frequencies, as the calibration of such weights is often challenging as it depends on uncertain information such as acquisition and processing parameters. In the inversion, all frequencies and angles are used simultaneously to define the update direction of the optimization step. Hierarchical approaches for the sequential inversion with respect to the frequency or angles could also be applied but it might strengthen the crosstalk. The proposed inversion accounts for the velocity dispersion in both P- and S- wave velocities as the derived gradient equations (4.28 and 4.29) for V_P and V_S variables are frequency-dependent. The inversion predicts the model variables by simultaneously modeling the multi-angle broadband frequencies.

The viscoelastic inversion shows crosstalks between model variables, specifically seismic velocities and quality factors. Based on our tests, the velocity variables are dominant over the quality factors; hence to avoid the crosstalk, we perform the inversion in two steps: first, we invert the seismic data for the most sensitive properties e.g., seismic velocities and bulk density; then we apply inversion process for the less sensitive variables e.g., quality factors. This approach provides stable inversion results for less sensitive properties. In general, due to a lower sensitivity of the shear wave quality factor to the seismic data, it is more challenging to accurately estimate the Q_S when the seismic data is noise contaminated.

The proposed sensitivity analysis aims to quantify the uncertainty of the inverted model as a function of the variability of the initial models. Approximate Bayesian computation and Markov chain Monte Carlo methods could also be used to assess the posterior uncertainty in a Bayesian setting; however, the computational cost of these techniques is generally higher than the proposed sensitivity. Another approach for uncertainty quantification in the context of local optimization is the calculation of the inverse Hessian matrix around the convergence point as a proxy to the model covariance matrix, which provides an estimate of the null space around the solution of the optimization problem.

One of the main limitations of the described method is the instability of the solution for the quality factors in case of noisy data. This effect can be mitigated by Tikhonov regularization which improves the stability of the optimized model. The solution shows some dependency on the initial model possibly due to the presence of noise in the data, the approximation of the seismic forward model, and the local minima of the objective functions; however, the proposed uncertainty quantification captures the variability of

the solution as a function of the uncertainty of the initial model.

4.6 Conclusions

We proposed a constrained non-linear frequency-angle-dependent pre-stack inversion method to estimate seismic properties in viscoelastic media. The inversion of an-elastic properties, which are the P- and S- wave attenuation described as inverse quality factors (Q_P and Q_S), in addition to seismic velocities and density, provides high-resolution seismic images that can be used in the geophysical exploration and seismic monitoring of hydrocarbon fields, as well as in geothermal energy or geological sequestration of CO_2. The inversion algorithm relies on the gradient descent optimization technique in which a differentiable misfit function is iteratively minimized by using a second-order non-linear L-BFGS algorithm. The least-square misfit function is based on an angle-frequency-dependent forward model of broadband signals in the frequency domain. The first-order derivatives of the misfit function with respect to five model variables are analytically obtained using the adjoint-state technique and chain rule of derivatives, which results in an accurate and efficient implementation. The inversion method was tested on synthetic examples, in 1D and 2D, to predict the quality factors and validated for different an-elastic mechanisms and noise-contaminated seismic data. The results demonstrate that the proposed an-elastic non-linear AVO inversion process accurately retrieves the model variables with good convergence. The inversion process reliably estimates the fluid-related attenuation which demonstrates its effectiveness to be used as a direct fluid indicator. In the case of noisy data, the inversion results might show some instability and the solution might depend on the choice of the prior realization. In this case, we recommend the application of regularization parameters to obtain a stable estimation.

4.7 Acknowledgments

We are grateful to the National IOR Centre of Norway led by the University of Stavanger for the financial support of this project. We would also like to acknowledge Lundin Energy Norway and their partners Wintershall Dea and OMW in the Edvard Grieg license for providing the seismic data and well logs for this project. The computations and simulations were carried out with resources given by UNINETT Sigma2 - the National Infrastructure for High-Performance Computing and Data Storage in Norway.

4.8 Data availability statement

The synthetic data underlying this paper (example 1) will be shared on reasonable request to the corresponding author.

4.9 Appendix A: Rock physics models for quality factors

The Waters empirical expressions (Waters and Waters 1981) in relation to P- and S-wave velocities V_P and V_S (expressed in $km.s^{-1}$) are:

$$Q_P = 10.76 * V_P, \qquad Q_S = 10.76 * V_S \tag{4.14}$$

In the Dvorkin-Mavko nearly constant Q approximations, the formulation follows the wave-induced fluid flow (WIFF) mechanism, and the order of magnitude of the P-wave seismic attenuation (inverse quality factor) is proportional to the contrast between relaxed and unrelaxed moduli (Mavko et al. 2020) as:

$$\frac{1}{Q_P} \approx \frac{M_\infty - M_0}{\sqrt{M_\infty M_0}} \tag{4.15}$$

where M_0 and M_∞ are the low frequency (relaxed) and high frequency (unrelaxed) limits of the compressional P- wave modulus M_P respectively. The low-frequency limit (M_0) is obtained using Gassmann's fluid-substitution while the high-frequency limit (M_∞) is calculated using the patchy-saturation model (Mavko et al. 2020). The P-wave seismic attenuation depends on the difference between the two moduli. The S-wave seismic attenuation (Q_S^{-1}) is computed using a rock physics model for fully water-saturated rocks with heterogeneous solid frame (Dvorkin and Mavko 2006) as:

$$\left(\frac{Q_{P-\text{wet}}}{Q_{S-\text{wet}}}\right)^{-1} = \frac{5}{4}\frac{(\gamma-2)^2}{(\gamma-1)}\left(\frac{2\gamma}{3\gamma-2}\frac{\gamma}{3\gamma-3}\right)^{-1}, \qquad \gamma = \left(\frac{V_{P-\text{wet}}}{V_{S-\text{wet}}}\right)^2 \tag{4.16}$$

where the subscript *wet* means that the rock is fully saturated with water and the attenuation depends on the spatial heterogeneity of the rocks. For fully water-saturated rocks, the low-frequency limit of the P-wave modulus is obtained as:

$$M_{0-\text{wet}} = \overline{M}_{min}\frac{\bar{\phi}\,\overline{M}_{dry} - (1+\bar{\phi})K_w\,\overline{M}_{dry}/\overline{M}_{min} + K_w}{(1-\bar{\phi})K_w + \bar{\phi}\,\overline{M}_{min} - K_w\,\overline{M}_{dry}/\overline{M}_{min}} \tag{4.17}$$

where $\bar{\phi} = \langle\phi\rangle$ and $\overline{M}_{dry} = \left\langle M_{dry}^{-1}\right\rangle^{-1}$ represent the arithmetic average of porosity and a harmonic average of dry-rock modulus and $\overline{M}_{min}$ and K_w are mineral and water moduli respectively. The unrelaxed limit is computed as:

$$M_{\infty-\text{wet}} = \left\langle \left(M_{min}\frac{\phi\,M_{dry} - (1+\phi)K_w\,M_{dry}/M_{min} + K_w}{(1-\phi)K_w + \phi\,M_{min} - K_w\,M_{dry}/M_{min}}\right)^{-1}\right\rangle^{-1} \tag{4.18}$$

The P- wave seismic attenuation (Q_P^{-1}) is calculated from equation 4.15 by replacing the relaxed and unrelaxed moduli with $M_{0-\text{wet}}$ and $M_{\infty-\text{wet}}$. Finally, P- and S- wave velocities for water-saturated rocks ($V_{P-\text{wet}}$ and $V_{S-\text{wet}}$) are calculated using Gassmann's fluid substitution model by assuming the rock is fully saturated with water (Ahmed et al. 2017). The total attenuation is the sum of the two attenuation curves i.e., the sum of the attenuation due to fluid and elastic heterogeneity in rock (Mavko et al. 2020).

Several studies (Ehsan et al. 2016; Khalid and Ahmed 2016; Pride et al. 2004; Quintal et al. 2009; Quintal et al. 2011; Tisato and Quintal 2013; White et al. 1975; White 1975) demonstrate that the P- wave attenuation is frequency-dependent in partially

saturated rocks due to wave-induced fluid flow (WIFF). Here, we use the analytical solution of White's 1D interlayer-flow model (a 1D WIFF model) given by Quintal et al. (2009) to estimate the frequency-dependent Q_P.

White's analytical solution (White 1975) for the interlayer-flow model describes the P wave attenuation as frequency-dependent for a set of reservoir rock properties. Quintal et al. (2009) reformulated White's analytical solution as follows:

$$Q_{-White} = \frac{\mathrm{Re}(b)}{\mathrm{Im}(b)} \tag{4.19}$$

where Re and Im represent the real and imaginary parts while b is a complex number given by:

$$b = (1 + (I_1 g_1 + I_2 g_2)^{-1}) - 1 \tag{4.20}$$

The complex P wave modulus (H) is defined by the product of real numbers E_0 and b.

$$H = E_0 b \tag{4.21}$$

where

$$E_0 = \left(\frac{p_1}{E_{G1}} + \frac{p_2}{E_{G2}} \right)^{-1} \tag{4.22}$$

Indexes 1 and 2 describe the two different porous media and for each single saturated porous medium ($j = 1,2$). The equations are:

$$g_j = \frac{K_{Ej}}{2E_0(r_2 - r_1)^2 p_j}, \qquad I_j = \sqrt{i\omega' s_j} \coth\left(\frac{\sqrt{i\omega' s_j}}{2} \right), \qquad s_j = \frac{\eta_j d_j^2}{K_{Ej} k_j} \tag{4.23}$$

$$p = \frac{d}{d_1 + d_2} \tag{4.24}$$

In the above equations, $\omega' = 2\pi f$, k, and η are angular frequency, permeability, and fluid viscosity while p and d refer to the saturation levels and layer thicknesses respectively. The rest of the elastic properties (without index j) are given below and symbols are defined in Table 4.2.

$$E_G = K_{sat} + \frac{4}{3}\mu_d, \qquad K_E = \frac{E_d M}{E_G}, \qquad r = \frac{\beta_c M}{E_G} \tag{4.25}$$

$$K_{sat} = K_d + \beta_c^2 M, \qquad \beta_c = 1 - \frac{K_d}{K_m}, \quad M = \left[\frac{\beta_c - \phi}{K_m} + \frac{\phi}{K_f} \right]^{-1} \tag{4.26}$$

and

$$E_d = K_d + \frac{4}{3}\mu_d \tag{4.27}$$

4.10 Appendix B: Partial derivatives of the Lagrangian

The partial derivatives of the Lagrangian of the misfit function are as follows:

$$\begin{aligned}\frac{\partial \mathcal{L}}{\partial V_P[i]} = \int_{\theta,\omega} d\theta \Bigg\{ & \frac{A}{\alpha[i-1]}\,\lambda[i-1] - \frac{A}{\alpha[i]}\,\lambda[i] - \frac{A\Delta\alpha[i-1]}{2\alpha[i-1]^2}\,\lambda[i-1] - \frac{A\Delta\alpha[i]}{2\alpha[i]^2}\,\lambda[i] \\ & + \frac{4\beta[i-1]^2}{\alpha[i-1]^3}\,\sin^2\theta\,\frac{\Delta\beta[i-1]}{\beta[i-1]}\,\lambda[i-1] + \frac{4\beta[i]^2}{\alpha[i]^3}\,\sin^2\theta\,\frac{\Delta\beta[i]}{\beta[i]}\,\lambda[i] \\ & + \frac{2\beta[i-1]^2}{\alpha[i-1]^3}\,\sin^2\theta\,\frac{\Delta\rho[i-1]}{\rho[i-1]}\,\lambda[i-1] + \frac{2\beta[i]^2}{\alpha[i]^3}\,\sin^2\theta\,\frac{\Delta\rho[i]}{\rho[i]}\,\lambda[i] \\ & + \frac{4}{\pi}\frac{\beta[i-1]^2}{\alpha[i-1]^3}\,\sin^2\theta\,\ln\left(\frac{\omega_o}{\omega'}\right)\,\frac{\Delta\Xi_S[i-1]}{\Xi_S[i-1]}\,\lambda[i-1] \\ & + \frac{4}{\pi}\frac{\beta[i]^2}{\alpha[i]^3}\,\sin^2\theta\,\ln\left(\frac{\omega_o}{\omega'}\right)\,\frac{\Delta\Xi_S[i]}{\Xi_S[i]}\,\lambda[i] \Bigg\}\end{aligned} \tag{4.28}$$

$$\begin{aligned}\frac{\partial \mathcal{L}}{\partial V_S[i]} = \int_{\theta,\omega} d\theta \Bigg\{ & -\frac{2\Delta\beta[i-1]}{\alpha[i-1]^2}\,\sin^2\theta\,\lambda[i-1] - \frac{2\Delta\beta[i]}{\alpha[i]^2}\,\sin^2\theta\,\lambda[i] \\ & - \frac{4\beta[i-1]}{\alpha[i-1]^2}\,\sin^2\theta\,\lambda[i-1] + \frac{4\beta[i]}{\alpha[i]^2}\,\sin^2\theta\,\lambda[i] \\ & - \frac{2\beta[i-1]}{\alpha[i-1]^2}\,\sin^2\theta\,\frac{\Delta\rho[i-1]}{\rho[i-1]}\,\lambda[i-1] - \frac{2\beta[i]}{\alpha[i]^2}\,\sin^2\theta\,\frac{\Delta\rho[i]}{\rho[i]}\,\lambda[i] \\ & + \frac{4}{\pi}\frac{\beta[i-1]}{\alpha[i-1]^2}\,\sin^2\theta\,\ln\left(\frac{\omega_o}{\omega'}\right)\,\frac{\Delta\Xi_S[i-1]}{\Xi_S[i-1]}\,\lambda[i-1] \\ & + \frac{4}{\pi}\frac{\beta[i]}{\alpha[i]^2}\,\sin^2\theta\,\ln\left(\frac{\omega_o}{\omega'}\right)\,\frac{\Delta\Xi_S[i]}{\Xi_S[i]}\,\lambda[i] \Bigg\}\end{aligned} \tag{4.29}$$

$$\begin{aligned}\frac{\partial \mathcal{L}}{\partial \rho[i]} = \int_{\theta} d\theta \Bigg\{ & C[i-1]\left(\frac{1}{\rho[i-1]}\right)\,\lambda[i-1] - C[i]\left(\frac{1}{\rho[i]}\right)\,\lambda[i] \\ & - C[i-1]\left(\frac{\Delta\rho[i-1]}{\rho[i-1]^2}\right)\,\lambda[i-1] - C[i]\left(\frac{\Delta\rho[i]}{\rho[i]}\right)\,\lambda[i] \Bigg\}\end{aligned} \tag{4.30}$$

$$\begin{aligned}\frac{\partial \mathcal{L}}{\partial \xi_P[i]} = \int_{\theta,\omega} d\theta \Bigg\{ & \frac{D}{\Xi_P[i-1]}\,\lambda[i-1] - \frac{D}{\Xi_P[i]}\,\lambda[i] - \frac{D}{2}\,\frac{\Delta\Xi_P[i-1]}{\Xi_P[i-1]^2}\,\lambda[i-1] \\ & + \frac{D}{2}\,\frac{\Delta\Xi_P[i]}{\Xi_P[i]^2}\,\lambda[i] \Bigg\}\end{aligned} \tag{4.31}$$

and

$$\frac{\partial \mathcal{L}}{\partial \xi_S[i]} = \int_{\theta,\omega} d\theta \left\{ \frac{E}{\Xi_S[i-1]}\,\lambda[i-1] - \frac{E}{\Xi_S[i]}\,\lambda[i] - \frac{E}{2}\,\frac{\Delta\Xi_S[i-1]}{\Xi_S[i-1]^2}\,\lambda[i-1] - \frac{E}{2}\,\frac{\Delta\Xi_S[i]}{\Xi_S[i]^2}\,\lambda[i] \right\} \tag{4.32}$$

The state variable λ is given by the equation as:

$$\lambda[i] = -\sum_{\omega'=1}^{p} W(\omega') * (d[i] - f[i])(\hat{\omega}).\delta(\omega' - \hat{\omega}) \tag{4.33}$$

Table 4.2: Symbols used for the elastic moduli given in the equations 4.25 to 4.27.

Symbol	Parameter
E_G	Plane P wave modulus of saturated rock
K_E	Effective bulk modulus
r	Ratio of fast P wave fluid tension to total normal stress ratio
K_{sat}	Gassmann modulus
E_d	Dry-rock fast P-wave modulus
M	Solid-grain bulk modulus
β_c	Biot's coefficient
K_d	Frame bulk modulus
K_m	Solid bulk modulus
μ_d	Shear modulus

Chapter 5

Time lapse frequency-dependent AVO inversion method

By:
Ahmed, Nisar[1]
Weibull, Wiktor Waldemar[1]
Bhakta, Tuhin[2]
Grana, Dario [3]
Mukerji, Tapan[4]

[1]Department of Energy Resources, 4021 Stavanger, University of Stavanger, Norway

[2]NORCE Norwegian Research Centre, Norway

[3]Department of Geology and Geophysics, School of Energy Resources, University of Wyoming, Laramie, Wyoming 82071, United States

[4]Stanford University, Department of Geophysics, Stanford, California, USA

Paper to be submitted to:
Geophysics (2023)

The pre-print is not available in the repository (online) version.

Chapter 6

Concluding Remarks

"It takes a great deal of artwork to craft a rock into a masterpiece"

KAK

6.1 Summary of conclusions

The primary focus of this PhD dissertation is to develop new AVO inversion methods for seismic monitoring of fluid saturation and pore pressure changes in the reservoir rock either due to hydrocarbon production or fluid injection, for example, to enhance oil recovery or CO_2 storage by considering the elastic and an-elastic properties of the porous medium. Therefore, the developed inversion workflows not only consider the variation of seismic amplitudes with incident angles but also consider the frequency-dependent AVO. The new inversion techniques allow theoretical rock physics knowledge to be combined with the seismic reflectivity equations to interpret the seismic amplitudes in terms of fluid saturation and pressure variables quantitatively. In addition to the saturation and pressure changes, the inversion processes further estimate the seismic properties i.e., seismic velocities and corresponding quality factors and density in the elastic and an-elastic media. The conclusions based on the inversion processes are summarized as follows:

- The inversion methods to predict the model parameters are based on the gradient descent optimization technique wherein the least-square data misfit function is minimized by using a local optimization algorithm known as L-BFGS. The limited-memory BFGS algorithm approximates the second-order Hessian matrix and exclusively stores a few prior iterations and therefore allows faster convergence of the objective function to its minima.
- The gradient solution of the least-square data misfit function with respect to seismic velocities, density, and seismic quality factors is derived by using the adjoint-state method which provides a more accurate and efficient solution than another method e.g., the finite difference approximation. A discussion regarding the computational cost of the adjoint method in comparison with the finite difference approximation has been made in the dissertation appendices.
- In optimization, a constraint can be of many different types e.g., bound constraints, a constraint given by the equations (like constraint in the Lagrangian solution), prior bound constraints to restrict the solution space, or constraints such as Tikhonov regularization, etc. The developed elastic and frequency-dependent inversion methods to predict the seismic velocities, density, P and S wave quality factors, and saturation-pressure properties are defined as a constraint problem because of the constraint in the Lagrangian solution and Tikhonov regularization. However, in case of saturation and pressure inversion, physical bounds i.e., upper and lower bound limits are also implemented to get inverted results between these physical bounds e.g., water saturation must be between 0 and 1. Similarly, the pressure constraints are defined based on some prior engineering data.
- The proposed seismic AVO inverse theory follows the deterministic approach and finds the single best optimal solution, therefore, it does not account for the uncertainty in the model solution. However, we attempt to include the uncertainty study in the estimated properties by applying the inversion methods to various prior models obtained from spatially correlated multivariate Gaussian distribution.

- The elastic AVO inversion method provides a very good convergence by minimizing the least-square data misfit function and therefore provides a good estimation of seismic velocities and density. However, in the FAVO inversion method, reflection amplitude at an interface depends on the relative information of five properties (V_P, V_S, ρ, Q_P, and Q_S) of upper and lower mediums. Therefore, due to crosstalk between properties during the simultaneous inversion of multi-parameters, it becomes difficult to invert the least sensitive properties e.g., P and S wave quality factors. The crosstalk issue has been overcome by inverting the data in two steps i.e., first performing the inversion for the most sensitive properties and then less influential properties. This way FAVO inversion method provides a close estimation of seismic velocities, quality factors, and density. However, the signal-to-noise ratio also affects the estimation of the least influential parameters such as P and S wave quality factors. The S wave quality factor computed from the constant Q-model due to rock heterogeneities does not have a spatial and vertical correlation with other seismic properties and is also the least influential parameter to the seismic data. Therefore, the inverted Q_S profile is not in close agreement with the true model. The applications of the elastic and an-elastic inversion schemes have been tested on 1D and 2D synthetic examples.

- The elastic AVO and the frequency-dependent AVO inversion methods are extended to predict the pore fluids saturation and effective pressure or changes in these properties. Various rock physics models, for example, the Gassmann fluid substitution equation with uniform and patchy fluids distribution patterns, the MacBeth-Grana's formulas, and constant Q methods are used to relate the saturation-pressure variables with elastic properties and seismic quality factors. Then the multivariable chain rule for derivatives and the adjoint method are applied to derive the gradient solution of the water saturation and effective pressure. The rock physics model for the P wave attenuation considers the seismic energy loss due to the viscous friction between the pore fluids (partially saturated rock) and elastic heterogeneities in the reservoir rock (when rock is fully water-saturated). While the S wave attenuation model only assumes that the heterogenous rock is fully water-saturated. However, the energy loss is not only due to rock inhomogeneities but also caused by wave-induced fluid flow, for example, water moves from one part of the rock to the other part due to WIFF.

- Various application tests for both 4D inversion methods (elastic and FAVO) have been run on 1D synthetic data modeled from the real well logs by assuming various time-lapse scenarios with different SNR levels. Similarly, the inversion methods are also tested on 2D synthetic data simulated for the CO_2 injection. Both methods provide a stable and reliable estimation of these properties with very good convergence and the RMSE between true and predicted values is very small. However, when there is a very good spatial correlation between model properties and elastic properties (e.g., the 1D example of oil saturation simulated for various 4D scenarios), both inversion methods provide a better estimation. In the case of 2D CO_2 injection data, there is no good spatial correlation between saturation and pressure properties and with elastic and an-elastic properties. Therefore, root

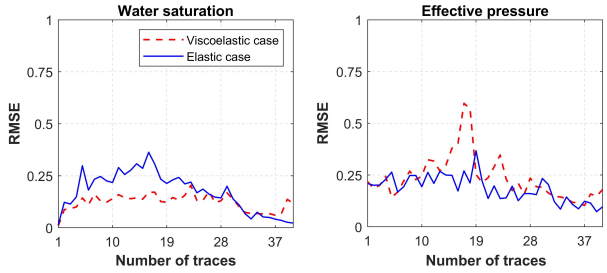

Figure 6.1: Comparisons between root mean squared errors (RMSEs) of the elastic AVO and FAVO inversion methods. The error comparison is calculated for the true and inverted models shown in Figures 3.15 and 5.10 when initial models somehow seem in correlation with true models.

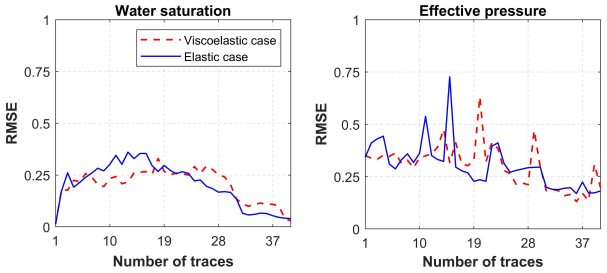

Figure 6.2: Comparisons between root mean squared errors (RMSEs) of the elastic AVO and FAVO inversion methods. The error comparison is calculated for the true and inverted models shown in Figures 3.17 and 3.18 (elastic AVO case) and Figures 5.12 and 5.13 (FAVO case) when initial models are not in good correlation with true models.

mean square error is comparatively higher in the inverted models of saturation and pressure properties in the CO_2 injected part.

- Further, the partially gas-saturated reservoirs like CO_2/water exhibit higher P wave attenuation (as shown in Figure 1.2), therefore, the 4D FAVO inversion method provides CO_2/water saturation estimation with higher accuracy than the elastic AVO inversion method. The comparisons between root mean squared errors (RMSEs) of the elastic AVO and FAVO inversion methods have been shown in Figures 6.1 and 6.2. The viscoelastic inversion method shows lower errors as compared to elastic AVO inversion in the case of saturation estimation. However, both methods provide pressure estimation with almost equal accuracy. The error comparisons have been made for the first 40 traces.

- Both elastic and FAVO inversion methods provide a good estimation in the case of an oil-water reservoir. In the case of CO_2 monitoring, the viscoelastic FAVO inversion provides a better estimation of CO_2 saturation. This is because the oil/water phases display small time-lapse P wave attenuation whereas the gasses (especially when a small amount of gas is present in the reservoir) show higher

attenuation and the dispersive nature of the medium. This leads to the conclusion that the FAVO method is more suitable while monitoring the CO_2 injection or mapping the gas saturation.

- This dissertation also concludes that bound constraints and regularization are essential, especially for the accurate inversion of water saturation and pressure variables. The accuracy in the predicted results therefore largely affected by the regularization weights and upper and lower limits of the bound constraints.

- The described inversion method is based on the Gassmann theory and one very general perception is that the Gassmann equation is perhaps inappropriate for the carbonate reservoirs due to the complex pore system and the violation of some of its assumptions. Therefore, another question about the validity of this method for the carbonate reservoirs can also be posed in the reader's mind. From the scientific literature (Agersborg et al. 2008; Li et al. 2014; Vega et al. 2007), enough support for the use of Gassmann's theory in the modeling of carbonate rocks-fluids interaction is available. The laboratory measurements indicate that Gassmann's equation estimates the P wave velocity in the non-clastic textures to an accuracy of 5 % (Adam et al. 2006). Another way to answer this question is if the information about pore space morphology, detailed mineralogy, etc. is available, other rock physics models reported (Mavko et al. 2020) for the carbonates can be add-on to this inversion method in a similar fashion.

- In addition, this work supposes constant mass density as a result of pore (or effective) pressure variations by ignoring the minor porosity changes due to varying pressure. Numerous researchers (Gurevich 2004; Shapiro and Kaselow 2005) have studied the effect of pressure on the reservoir density, and these changes occur in the reservoir rock during the production or recovery process. Therefore, it is important to assume a few percent variations in reservoir porosity due to pressure changes (MacBeth 2004), and these changes ultimately affect the seismic reflection amplitudes during the time-lapse inverse process (Ahmed et al. 2024). MacBeth (2004) stated the pressure effects on the reservoir density by deriving an exponential compaction model as given below:

$$\rho(P_e) = \rho_\infty + (\rho_0 - \rho_\infty)^{-P_e/P_\rho}, \tag{6.1}$$

whereas ρ_∞ is considered to be equal to the density of rock-forming minerals (ρ_m), P_ρ denotes the characteristic pressure for the compaction process, and the bulk density ρ_0 is a function of fluid saturation and reservoir porosity given by the mass balance equation (Equation 3.9).

The pressure effect on the porosity can be further estimated by assuming that the compaction trend for porosity is supposed to be known everywhere and can be modeled by using the following empirical model:

$$\phi_t = \phi_0 - \alpha_c(P_{e_t} - P_{e_0}), \tag{6.2}$$

where the subscripts 0 and t define the time at the baseline and monitor respectively and α_c represent the calibration constant for the compaction trend (Rimstad

et al. 2012). Both density and porosity effects are modeled well in the inversion method published by Ahmed et al. (2024) which is the modified version of Chapter 3 titled 'Constrained non-linear AVO inversion for dynamic reservoir changes estimation from time-lapse seismic data'. This work has been accepted and is going to be published in the Geophysics, 89:1 (2024).

6.2 Future work

There is a wide range of possibilities that exist to significantly extend the proposed methodologies for the elastic and frequency-dependent inversion schemes. Some possible future working domains are listed below:

- The described frequency-dependent AVO inversion schemes are based on the constant Q models and therefore do not consider the seismic wave velocities and attenuation factors as a function of frequency. In other words, these inverse modeling techniques do not take into account the velocity dispersion. Therefore, the FAVO inversion algorithm can be extended, for instance, by using the R_{PP} equation wherein the P wave reflection coefficients depend on the seismic frequencies through seismic velocities and quality factors (or attenuation).

- In the inversion of saturation and pressure properties (S_w and P_e respectively), these parameters are linked to the seismic parameters through rock physics. Therefore, the sensitivity S_w and P_e depends on the appropriate rock physics model and reservoir rock properties e.g., porosity and permeability. For this reason, it might be required a more detailed study by implementing the various rock physics models that relate the seismic velocities, attenuation, and density with saturation and pressure properties. This will help to choose a rock physics model that defines more sensitivity of the model properties to the reflectivity operator. In the same way, the convergence of the objective function to the minima can be tested by using the global optimization methods which however require a large number of iterations in comparison to the local optimizations to find the desirable minima.

- The uncertainty in the present work has been shown by computing the probability distributions against individual prior realizations. However, the uncertainty quantification in the time-lapse frequency-dependent AVO inversion methods can be shown by computing the full probability distributions by using the Bayesian and Markov Chain Monte Carlo (MCMC) techniques (Grana et al. 2022; Grana and Mukerji 2015).

- Further future work might also include the viscoelastic full waveform inversion - FWI (Fabien-Ouellet et al. 2017) integrated with rock physics theory to estimate the reservoir dynamic changes. However, highly optimized modeling FWI algorithms are perhaps quite time-consuming to predict the model variables of interest.

Bibliography

Adam, L., Batzle, M., and Brevik, I. (2006). "Gassmann's fluid substitution and shear modulus variability in carbonates at laboratory seismic and ultrasonic frequencies". In: *Geophysics* 71.6, F173–F183.

Agersborg, R., Johansen, T. A., Jakobsen, M., Sothcott, J., and Best, A. (2008). "Effects of fluids and dual-pore systems on pressure-dependent velocities and attenuations in carbonates". In: *Geophysics* 73.5, N35–N47.

Ahmad, M., Ahmed, N., Khalid, P., Badar, M. A., Akram, S., Hussain, M., Anwar, M. A., Mahmood, A., Ali, S., and Rehman, A. U. (2019). "Impact of pore fluid heterogeneities on angle-dependent reflectivity in poroelastic layers: A study driven by seismic petrophysics". In: *Geomech Eng* 17, pp. 343–354.

Ahmed, N. and Weibull, W. (2022). "Gradient Descent Optimization Method for AVO Inversion in Viscoelastic Media". In: *83rd EAGE Annual Conference & Exhibition*. Vol. 2022. European Association of Geoscientists & Engineers, pp. 1–5.

Ahmed, N., Khalid, P., and Anwar, A. W. (2016). "Rock physics modeling to assess the impact of spatial distribution pattern of pore fluid and clay contents on acoustic signatures of partially-saturated reservoirs". In: *Acta Geodaetica et Geophysica* 51.1, pp. 1–13.

Ahmed, N., Khalid, P., Shafi, H. M. B., and Connolly, P. (2017). "DHI evaluation by combining rock physics simulation and statistical techniques for fluid identification of Cambrian-to-Cretaceous clastic reservoirs in Pakistan". In: *Acta Geophysica* 65.5, pp. 991–1007.

Ahmed, N., Weibull, W. W., and Grana, D. (2022). "Constrained non-linear AVO inversion based on the adjoint-state optimization". In: *Computers & Geosciences*, p. 105214.

Ahmed, N., Weibull, W. W., Grana, D., and Bhakta, T. (2024). "Constrained non-linear AVO inversion for dynamic reservoir changes estimation from time-lapse seismic data". In: *Geophysics* 89.1, pp. 1–65.

Ahmed, N., Weibull, W. W., Quintal, B., Grana, D., and Bhakta, T. (2023). "Frequency-dependent AVO inversion applied to physically based models for seismic attenuation". In: *Geophysical Journal International* 233.1, pp. 234–252.

Aki, K. and Richards, P. G. (1980). *Quantitative seismology: Theory and methods*. The Maple-Vail Book Manufacturing Group USA.

— (2002). *Quantitative seismology*. The Maple-Vail Book Manufacturing Group USA.

Alessandrini, G., Maarten, V., Faucher, F., Gaburro, R., and Sincich, E. (2019). "Inverse problem for the Helmholtz equation with Cauchy data: Reconstruction with conditional well-posedness driven iterative regularization". In: *ESAIM: Mathematical Modelling and Numerical Analysis* 53.3, pp. 1005–1030.

Alvarez, E. and MacBeth, C. (2014). “An insightful parametrization for the flatlander’s interpretation of time-lapsed seismic data”. In: *Geophysical Prospecting* 62.1, pp. 75–96.

Angelov, P., Spetzler, J., and Wapenaar, K. (2004). “Pore pressure and water saturation variations; Modification of Landrø’s AVO approach”. In: *SEG Technical Program Expanded Abstracts 2004*. Society of Exploration Geophysicists, pp. 2279–2282.

Assis, C. A. and Schleicher, J. (2021). “Introduction of the Hessian in joint migration inversion and improved recovery of structural information using image-based regularization”. In: *Geophysics* 86.6, R777–R793.

Aster, R. C., Borchers, B., and Thurber, C. H. (2018). *Parameter estimation and inverse problems*. Elsevier.

Avseth, P., Mukerji, T., and Mavko, G. (2010). *Quantitative seismic interpretation: Applying rock physics tools to reduce interpretation risk*. Cambridge university press.

Azevedo, L., Grana, D., and Figueiredo, L. de (2020). “Stochastic perturbation optimization for discrete-continuous inverse problems”. In: *Geophysics* 85.5, pp. M73–M83.

Barton, N. (2006). *Rock quality, seismic velocity, attenuation and anisotropy*. CRC press.

Batzle, M. and Wang, Z. (1992). “Seismic properties of pore fluids”. In: *Geophysics* 57.11, pp. 1396–1408.

Bhakta, T. (2018). “Improvement of pressure-saturation changes estimations from time-lapse PP-AVO data by using non-linear optimization method”. In: *Journal of Applied Geophysics* 155, pp. 1–12.

Bhakta, T. and Landrø, M. (2014). “Estimation of pressure-saturation changes for unconsolidated reservoir rocks with high VP/VS ratio”. In: *Geophysics* 79.5, pp. M35–M54.

Bhakta, T., Paap, B., Vandeweijer, V., and Mannseth, T. (2022). “Monitoring of CO2 plume movement using time-lapse distributed acoustic sensing (DAS) data”. In: *SEG/AAPG International Meeting for Applied Geoscience & Energy*. OnePetro.

Biondi, E., Barnier, G., Clapp, R. G., Picetti, F., and Farris, S. (2021). “An object-oriented optimization framework for large-scale inverse problems”. In: *Computers & Geosciences* 154, p. 104790.

Biot, M. A. (1956). “Theory of propagation of elastic waves in a fluid-saturated porous solid. II. Higher frequency range”. In: *The Journal of the acoustical Society of america* 28.2, pp. 179–191.

— (1962). “Mechanics of deformation and acoustic propagation in porous media”. In: *Journal of applied physics* 33.4, pp. 1482–1498.

Blanchard, T. D. and Delommot, P. (2015). “An example of the measurement and practical applications of time-lapse seismic attenuation”. In: *Geophysics* 80.2, WA25–WA34.

Blanchard, T. D. (2011). *Time-lapse seismic attenuation as a tool for monitoring hydrocarbons and CO2 in geological materials*. University of Leeds.

Bourbié, T., Coussy, O., Zinszner, B., and Junger, M. C. (1992). *Acoustics of porous media*.

Brossier, R., Operto, S., and Virieux, J. (2010). "Which data residual norm for robust elastic frequency-domain full waveform inversion?" In: *Geophysics* 75.3, R37–R46.

Broyden, C. G. (1970). "The convergence of a class of double-rank minimization algorithms 1. general considerations". In: *IMA Journal of Applied Mathematics* 6.1, pp. 76–90.

Buland, A. and Omre, H. (2003a). "Bayesian linearized AVO inversion". In: *Geophysics* 68.1, pp. 185–198.

Buland, A. and El Ouair, Y. (2006). "Bayesian time-lapse inversion". In: *Geophysics* 71.3, R43–R48.

Buland, A. and Omre, H. (2003b). "Bayesian linearized AVO inversion". In: *Geophysics* 68.1, pp. 185–198.

Carcione, J. M. (2007). *Wave fields in real media: Wave propagation in anisotropic, anelastic, porous and electromagnetic media*. Elsevier.

Carcione, J. M., Helle, H. B., and Zhao, T. (1998). "Effects of attenuation and anisotropy on reflection amplitude versus offset". In: *Geophysics* 63.5, pp. 1652–1658.

Carcione, J. M., Kosloff, D., and Kosloff, R. (1988). "Wave propagation simulation in a linear viscoacoustic medium". In: *Geophysical Journal International* 93.2, pp. 393–401.

Carcione, J. M. and Picotti, S. (2006). "P-wave seismic attenuation by slow-wave diffusion: Effects of inhomogeneous rock properties". In: *Geophysics* 71.3, O1–O8.

Caspari, E., Novikov, M., Lisitsa, V., Barbosa, N. D., Quintal, B., Rubino, J. G., and Holliger, K. (2019). "Attenuation mechanisms in fractured fluid-saturated porous rocks: a numerical modelling study". In: *Geophysical Prospecting* 67.4-Rock Physics: from microstructure to seismic signatures, pp. 935–955.

Castagna, J. P., Batzle, M. L., and Eastwood, R. L. (1985). "Relationships between compressional-wave and shear-wave velocities in clastic silicate rocks". In: *geophysics* 50.4, pp. 571–581.

Castagna, J. P., Swan, H. W., and Foster, D. J. (1998). "Framework for AVO gradient and intercept interpretation". In: *Geophysics* 63.3, pp. 948–956.

Chapman, M., Liu, E., and Li, X.-Y. (2006). "The influence of fluid sensitive dispersion and attenuation on AVO analysis". In: *Geophysical Journal International* 167.1, pp. 89–105.

Chapman, S., Borgomano, J. V., Quintal, B., Benson, S. M., and Fortin, J. (2021). "Seismic wave attenuation and dispersion due to partial fluid saturation: Direct measurements and numerical simulations based on X-ray CT". In: *Journal of Geophysical Research: Solid Earth* 126.4, e2021JB021643.

Chen, H., Innanen, K. A., and Chen, T. (2018). "Estimating P-and S-wave inverse quality factors from observed seismic data using an attenuative elastic impedanceP-and S-wave inverse quality factors". In: *Geophysics* 83.2, R173–R187.

Cheng, G., Yin, X., and Zong, Z. (2020). "Frequency-dependent spherical-wave nonlinear AVO inversion in elastic media". In: *Geophysical Journal International* 223.2, pp. 765–776.

Cheng, G., Yin, X., Zong, Z., Xia, T., Wang, J., and Liu, H. (2022). "Seismic inversion using complex spherical-wave reflection coefficient at different offsets and frequencies". In: *Geophysics* 87.2, R183–R192.

Cheng, W.-B. (2013). “Three-dimensional seismic attenuation structure beneath the Taiwan region and its tectonic implication”. In: *Journal of Asian Earth Sciences* 65, pp. 86–99.

Chiappa, F. and Mazzotti, A. (2009). “Estimation of petrophysical parameters by linearized inversion of angle domain pre-stack data”. In: *Geophysical Prospecting* 57.3, pp. 413–426.

Constable, S. C., Parker, R. L., and Constable, C. G. (1987). “Occam’s inversion: A practical algorithm for generating smooth models from electromagnetic sounding data”. In: *Geophysics* 52.3, pp. 289–300.

Cordua, K. S., Hansen, T. M., and Mosegaard, K. (2012). “Monte Carlo full-waveform inversion of crosshole GPR data using multiple-point geostatistical a priori information”. In: *Geophysics* 77.2, H19–H31.

Correia, G., Davolio, A., and Schiozer, D. (2014). “Improvement of pressure and saturation estimations from 4D seismic supported by flow simulation data”. In: *76th EAGE Conference and Exhibition 2014*. Vol. 2014. 1. EAGE Publications BV, pp. 1–5.

Côrte, G., Amini, H., and MacBeth, C. (2023). “Bayesian inversion of 4D seismic data to pressure and saturation changes: Application to a west of Shetlands field”. In: *Geophysical Prospecting* 71.2, pp. 292–321.

Dadashpour, M., Landrø, M., and Kleppe, J. (2008). “Nonlinear inversion for estimating reservoir parameters from time-lapse seismic data”. In: *Journal of Geophysics and Engineering* 5.1, pp. 54–66.

Davolio, A., Maschio, C., and Schiozer, D. J. (2012). “Pressure and saturation estimation from P and S impedances: a theoretical study”. In: *Journal of Geophysics and Engineering* 9.5, pp. 447–460.

— (2013). “A methodology to constrain pressure and saturation estimation from 4D seismic using multiple simulation models and observed data”. In: *Journal of Petroleum Science and Engineering* 105, pp. 51–61.

Dinh, H. N. and Van der Baan, M. (2019). “A grid-search approach for 4D pressure-saturation discrimination”. In: *Geophysics* 84.4, pp. IM47–IM62.

Downton, J. (2005). “Seismic parameter estimation from AVO inversion [Ph. D. thesis]”. In: *Calgary: The University of Calgary*.

Downton, J. E. and Ursenbach, C. (2006). “Linearized amplitude variation with offset (AVO) inversion with supercritical angles”. In: *Geophysics* 71.5, E49–E55.

Doyen, P. (2007). *Seismic reservoir characterization: An earth modelling perspective*. Vol. 2. EAGE publications Houten.

Du, B.-Y., Yang, W.-Y., Zhang, J., Yong, X.-S., Gao, J.-H., and Li, H.-S. (2019). “Matrix-fluid decoupling-based joint PP-PS-wave seismic inversion for fluid identification”. In: *Geophysics* 84.3, R477–R487.

Dupuy, B., Romdhane, A., Eliasson, P., and Yan, H. (2021a). “Combined geophysical and rock physics workflow for quantitative CO2 monitoring”. In: *International Journal of Greenhouse Gas Control* 106, p. 103217.

Dupuy, B., Romdhane, A., Nordmann, P.-L., Eliasson, P., and Park, J. (2021b). “Bayesian rock physics inversion: application to CO2 storage monitoring”. In: *Geophysics* 86.4, pp. 1–73.

Dvorkin, J. P. and Mavko, G. (2006). "Modeling attenuation in reservoir and nonreservoir rock". In: *The Leading Edge* 25.2, pp. 194–197.

Ehsan, M. I., Khalid, P., Ahmed, N., You, J., Liu, X., and Azeem, T. (2016). "Seismic attenuation and velocity dispersion to discriminate gas hydrates and free gas zone, Makran offshore, Pakistan". In: *International Journal of Geosciences* 7.8, pp. 1020–1028.

Emerick, A. A. (2014). "Estimation of pressure and saturation fields from time-lapse impedance data using the ensemble smoother". In: *Journal of Geophysics and Engineering* 11.3, p. 035007.

Epelle, E. I. and Gerogiorgis, D. I. (2020). "Adjoint-based well placement optimisation for Enhanced Oil Recovery (EOR) under geological uncertainty: From seismic to production". In: *Journal of Petroleum Science and Engineering* 190, p. 107091.

Evensen, G. et al. (2009). *Data assimilation: the ensemble Kalman filter*. Vol. 2. Springer.

Fabien-Ouellet, G., Gloaguen, E., and Giroux, B. (2017). "Time domain viscoelastic full waveform inversion". In: *Geophysical Journal International* 209.3, pp. 1718–1734.

Fatti, J. L., Smith, G. C., Vail, P. J., Strauss, P. J., and Levitt, P. R. (1994). "Detection of gas in sandstone reservoirs using AVO analysis: A 3-D seismic case history using the Geostack technique". In: *Geophysics* 59.9, pp. 1362–1376.

Faucher, F., Alessandrini, G., Barucq, H., Hoop, M. V. de, Gaburro, R., and Sincich, E. (2019). "Full reciprocity-gap waveform inversion in the frequency domain, enabling sparse-source acquisition". In: *arXiv preprint arXiv:1907.09163*.

Feng-Qi, Z., Fu-Ji, W., Yan-Chun, W., Wei-Jun, W., and Yan, L. (2013). "Generalized linear AVO inversion with the priori constraint of trivariate cauchy distribution based on Zoeppritz equation". In: *CHINESE JOURNAL OF GEOPHYSICS-CHINESE EDITION* 56.6, pp. 2098–2115.

Figueiredo, L. P. de, Grana, D., Roisenberg, M., and Rodrigues, B. B. (2019). "Gaussian mixture Markov chain Monte Carlo method for linear seismic inversion". In: *Geophysics* 84.3, R463–R476.

Fletcher, R. (1970). "A new approach to variable metric algorithms". In: *The computer journal* 13.3, pp. 317–322.

Floricich, M., Jenkins, G., and McCormick, D. (2012). "Probabilistic inversion of multiple 4D seismic as applied on Schiehallion field". In: *74th EAGE Conference and Exhibition incorporating EUROPEC 2012*. EAGE Publications BV, cp–293.

Forberg, O. B., Grana, D., and Omre, H. (2021). "Bayesian inversion of time-lapse seismic AVO data for multimodal reservoir properties". In: *IEEE Transactions on Geoscience and Remote Sensing* 59.11, pp. 9104–9119.

Gardner, G., Gardner, L., and Gregory, A. (1974). "Formation velocity and density—The diagnostic basics for stratigraphic traps". In: *Geophysics* 39.6, pp. 770–780.

Gassmann, F. (1951). "Elastic waves through a packing of spheres". In: *Geophysics* 16.4, pp. 673–685.

Ghosh, S. K. (2000). "Limitations on impedance inversion of band-limited reflection data". In: *Geophysics* 65.3, pp. 951–957.

Goldfarb, D. (1970). "A family of variable-metric methods derived by variational means". In: *Mathematics of computation* 24.109, pp. 23–26.

Golub, G. H. and Van Loan, C. F. (2013). *Matrix computations. Johns Hopkins studies in the mathematical sciences*.

Gouveia, W. P. and Scales, J. A. (1997). "Resolution of seismic waveform inversion: Bayes versus Occam". In: *Inverse problems* 13.2, p. 323.

Grana, D. (2016). "Pressure–velocity relations in reservoir rocks: Modified MacBeth's equation". In: *Journal of Applied Geophysics* 132, pp. 234–241.

— (2020). "Bayesian petroelastic inversion with multiple prior models". In: *Geophysics* 85.5, pp. M57–M71.

Grana, D., Figueiredo, L. de, and Mosegaard, K. (2022). "Markov chain Monte Carlo for petrophysical inversion". In: *Geophysics* 87.1, pp. M13–M24.

Grana, D. and Mukerji, T. (2015). "Bayesian inversion of time-lapse seismic data for the estimation of static reservoir properties and dynamic property changes". In: *Geophysical Prospecting* 63.3, pp. 637–655.

Grana, D., Mukerji, T., and Doyen, P. (2021). *Seismic reservoir modeling: Theory, examples, and algorithms*. John Wiley & Sons.

Grude, S., Landrø, M., and Osdal, B. (2013). "Time-lapse pressure–saturation discrimination for CO2 storage at the Snøhvit field". In: *International Journal of Greenhouse Gas Control* 19, pp. 369–378.

Guo, G., Lan, H., Zhou, X., Liu, Y., Bin Waheed, U., and Chen, J. (2022). "Topography-dependent eikonal tomography based on the fast-sweeping scheme and the adjoint-state technique". In: *Geophysics* 87.2, U29–U41.

Gurevich, B. (2004). "A simple derivation of the effective stress coefficient for seismic velocities in porous rocks". In: *Geophysics* 69.2, pp. 393–397.

Gurevich, B. and Carcione, J. M. (2022). *Attenuation and Dispersion of Elastic Waves in Porous Rocks: Mechanisms and models*.

Hedlin, K., Mewhort, L., and Margrave, G. (2001). "Delineation of steam flood using seismic attenuation". In: *SEG Technical Program Expanded Abstracts 2001*. Society of Exploration Geophysicists, pp. 1572–1575.

Hill, R. (1963). "Elastic properties of reinforced solids: some theoretical principles". In: *Journal of the Mechanics and Physics of Solids* 11.5, pp. 357–372.

Hilterman, F. (1990). "Is AVO the seismic signature of lithology? A case history of Ship Shoal-South Addition". In: *The Leading Edge* 9.6, pp. 15–22.

Holt, R. M., Nes, O.-M., and Fjaer, E. (2005). "In-situ stress dependence of wave velocities in reservoir and overburden rocks". In: *The Leading Edge* 24.12, pp. 1268–1274.

Hu, G.-Q., Liu, Y., Wei, X.-C., and Chen, T.-S. (2011). "Joint PP and PS AVO inversion based on Bayes theorem". In: *Applied Geophysics* 8.4, pp. 293–302.

Hu, J., Qian, J., Cao, J., Wang, X., Wang, H., and Leung, S. (2021). "Ray illumination compensation for adjoint-state first-arrival traveltime tomography". In: *Geophysics* 86.5, pp. 1–43.

Hussain, M. and Ahmed, N. (2018). "Reservoir geomechanics parameters estimation using well logs and seismic reflection data: insight from Sinjhoro Field, Lower Indus Basin, Pakistan". In: *Arabian Journal for Science and Engineering* 43.7, pp. 3699–3715.

Innanen, K. A. (2011). "Inversion of the seismic AVF/AVA signatures of highly attenuative targets". In: *Geophysics* 76.1, R1–R14.

JafarGandomi, A. and Takenaka, H. (2013). "FDTD3C—A FORTRAN program to model multi-component seismic waves for vertically heterogeneous attenuative media". In: *Computers & Geosciences* 51, pp. 314–323.

Jänicke, R., Quintal, B., Larsson, F., and Runesson, K. (2019). "Viscoelastic substitute models for seismic attenuation caused by squirt flow and fracture leak off". In: *Geophysics* 84.4, WA183–WA189.

Jänicke, R., Quintal, B., and Steeb, H. (2015). "Numerical homogenization of mesoscopic loss in poroelastic media". In: *European Journal of Mechanics-A/Solids* 49, pp. 382–395.

Jin, S. and Madariaga, R. (1994). "Nonlinear velocity inversion by a two-step Monte Carlo method." In: *Geophysics* 59.4, pp. 577–590.

Jin, Z., Chapman, M., Wu, X., and Papageorgiou, G. (2017). "Estimating gas saturation in a thin layer by using frequency-dependent amplitude versus offset modelling". In: *Geophysical Prospecting* 65.3, pp. 747–765.

Johnston, D. H. (2013). *Practical applications of time-lapse seismic data*. Society of Exploration Geophysicists.

Johnston, D. H., Toksöz, M., and Timur, A. (1979). "Attenuation of seismic waves in dry and saturated rocks: II. Mechanisms". In: *Geophysics* 44.4, pp. 691–711.

Kamei, R. and Pratt, R. (2013). "Inversion strategies for visco-acoustic waveform inversion". In: *Geophysical Journal International* 194.2, pp. 859–884.

Keating, S. and Innanen, K. A. (2020). "Parameter crosstalk and leakage between spatially separated unknowns in viscoelastic full-waveform inversionCrosstalk analysis in viscoelastic FWI". In: *Geophysics* 85.4, R397–R408.

Khalid, P. and Ahmed, N. (2016). "Modulus defect, velocity dispersion and attenuation in partially-saturated reservoirs of Jurassic sandstone, Indus Basin, Pakistan". In: *Studia Geophysica et Geodaetica* 60.1, pp. 112–129.

Kneib, G. and Shapiro, S. A. (1995). "Viscoacoustic wave propagation in 2-D random media and separation of absorption and scattering attenuation". In: *Geophysics* 60.2, pp. 459–467.

Kolbjørnsen, O., Buland, A., Hauge, R., Røe, P., Ndingwan, A. O., and Aker, E. (2020). "Bayesian seismic inversion for stratigraphic horizon, lithology, and fluid prediction". In: *Geophysics* 85.3, R207–R221.

Kumar, D., Zhao, Z., Foster, D. J., Dralus, D., and Sen, M. K. (2020). "Frequency-dependent AVO analysis using the scattering response of a layered reservoir". In: *Geophysics* 85.2, N1–N16.

Kurt, H. (2007). "Joint inversion of AVA data for elastic parameters by bootstrapping". In: *Computers & Geosciences* 33.3, pp. 367–382.

Kvam, Ø. and Landrø, M. (2005). "Pore-pressure detection sensitivities tested with time-lapse seismic data". In: *Geophysics* 70.6, O39–O50.

Landa, J., Meadows, M., Thacher, C., Waddle, R., and Williams, N. (2015). "Map-based estimation of reservoir pressure and saturation from 4D seismic with a data-driven procedure". In: *SPE Annual Technical Conference and Exhibition*. OnePetro.

Landrø, M. (2001). "Discrimination between pressure and fluid saturation changes from time-lapse seismic data". In: *Geophysics* 66.3, pp. 836–844.

Landrø, M., Veire, H. H., Duffaut, K., and Najjar, N. (2003). "Discrimination between pressure and fluid saturation changes from marine multicomponent time-lapse seismic data". In: *Geophysics* 68.5, pp. 1592–1599.

Lang, X. and Grana, D. (2017). "Bayesian petrophysics inversion of seismic data based on linearized seismic and rock physics modeling". In: *2017 SEG International Exposition and Annual Meeting*. OnePetro.

— (2019). "Rock physics modelling and inversion for saturation-pressure changes in time-lapse seismic studies". In: *Geophysical Prospecting* 67.7, pp. 1912–1928.

Le, H., Clapp, R. G., Levin, S. A., and Biondi, B. (2020). "A pipeline approach for three dimensional time-domain finite-difference multi-parameter waveform inversion on GPUs". In: *Computers & Geosciences* 140, p. 104503.

Levenberg, K. (1944). "A method for the solution of certain non-linear problems in least squares". In: *Quarterly of applied mathematics* 2.2, pp. 164–168.

Li, C. and Liu, X. (2019). "Amplitude variation with incident angle inversion for Q-factors in viscoelastic media: A case study". In: *Geophysics* 84.6, B419–B435.

LI, J.-Y., CHEN, X.-H., HAO, Z.-J., and RUI, Z.-H. (2005). "A study on multiple time-lapse seismic AVO inversion". In: *Chinese Journal of Geophysics* 48.4, pp. 974–981.

Li, J., Liner, C., and Stewart, R. (2014). "Time-lapse seismic modeling for CO 2 sequestration at the Dickman oilfield, Kansas". In: *Geophysics* 79.2, B81–B95.

Li, Q.-Z. (2017). *High-resolution seismic exploration*. Society of Exploration Geophysicists.

Li, Y., Li, J., Chen, X., Zhang, J., and Bo, X. (2021). "Prestack waveform inversion based on analytical solution of the viscoelastic wave equationPrestack waveform inversion". In: *Geophysics* 86.1, R45–R61.

Liu, D. C. and Nocedal, J. (1989). "On the limited memory BFGS method for large scale optimization". In: *Mathematical programming* 45.1, pp. 503–528.

Liu, H., Li, J., Chen, X., Hou, B., and Chen, L. (2016). "Amplitude variation with offset inversion using the reflectivity method". In: *Geophysics* 81.4, R185–R195.

Liu, L., Cao, S., and Wang, L. (2011). "Poroelastic analysis of frequency-dependent amplitude-versus-offset variations". In: *Geophysics* 76.3, pp. C31–C40.

Liu, X., Chen, J., Zeng, J., Liu, F., Huang, H., Zhao, Z., and Luo, Y. (2021). "An Adaptive Stratified Joint PP and PS AVA Inversion Using Accurate Jacobian Matrix". In: *Geophysics* 86.4, pp. 1–145.

Liu, X., Greenhalgh, S., Kumar, M., Li, H., Liu, B., Liao, Q., and Huang, X. (2022). "Reflection and transmission coefficients of spherical waves at an interface separating two dissimilar viscoelastic solids". In: *Geophysical Journal International* 230.1, pp. 252–271.

Luo, C., Ba, J., Carcione, J. M., Huang, G., and Guo, Q. (2020a). "Joint PP and PS pre-stack AVA inversion for VTI medium based on the exact Graebner equation". In: *Journal of Petroleum Science and Engineering* 194, p. 107416.

— (2020b). "Joint PP and PS pre-stack seismic inversion for stratified models based on the propagator matrix forward engine". In: *Surveys in Geophysics* 41.5, pp. 987–1028.

Luo, C., Li, X., and Huang, G. (2019). "Pre-stack AVA inversion by using propagator matrix forward modeling". In: *Pure and Applied Geophysics* 176.10, pp. 4445–4476.

Luo, X., Bhakta, T., Jakobsen, M., and Nævdal, G. (2017). "An ensemble 4D-seismic history-matching framework with sparse representation based on wavelet multiresolution analysis". In: *SPE Journal* 22.03, pp. 985–1010.

Luo, X., Stordal, A. S., Lorentzen, R. J., and Nævdal, G. (2015). "Iterative ensemble smoother as an approximate solution to a regularized minimum-average-cost problem: theory and applications". In: *SPE Journal* 20.05, pp. 962–982.

Ma, X.-Q. (2001). "Global joint inversion for the estimation of acoustic and shear impedances from AVO derived P-and S-wave reflectivity data". In: *first break* 19.10.

MacBeth, C. (2004). "A classification for the pressure-sensitivity properties of a sandstone rock frame". In: *Geophysics* 69.2, pp. 497–510.

MacBeth, C., Floricich, M., and Soldo, J. (2006). "Going quantitative with 4D seismic analysis". In: *Geophysical Prospecting* 54.3, pp. 303–317.

Maharramov, M., Biondi, B. L., and Meadows, M. A. (2016). "Time-lapse inverse theory with applicationsTime-lapse inverse theory". In: *Geophysics* 81.6, R485–R501.

Mallick, S. (1995). "Model-based inversion of amplitude-variations-with-offset data using a genetic algorithm". In: *Geophysics* 60.4, pp. 939–954.

— (2007). "Amplitude-variation-with-offset, elastic-impedence, and wave-equation synthetics—A modeling study". In: *Geophysics* 72.1, pp. C1–C7.

Marquardt, D. W. (1963). "An algorithm for least-squares estimation of nonlinear parameters". In: *Journal of the society for Industrial and Applied Mathematics* 11.2, pp. 431–441.

Maurya, S., Singh, K., Kumar, A., and Singh, N. (2018). "Reservoir characterization using post-stack seismic inversion techniques based on real coded genetic algorithm". In: *Jour. of Geophysics* 39.2.

Mavko, G., Dvorkin, J., and Walls, J. (2005). "A theoretical estimate of S-wave attenuation in sediment". In: *SEG Technical Program Expanded Abstracts 2005*. Society of Exploration Geophysicists, pp. 1469–1472.

Mavko, G., Mukerji, T., and Dvorkin, J. (2020). *The rock physics handbook*. Cambridge university press.

Meadows, M. A. (2001). "Enhancements to Landro's method for separating time-lapse pressure and saturation changes". In: *2001 SEG Annual Meeting*. OnePetro.

Meadows, M. A. and Cole, S. P. (2013). "4D seismic modeling and CO2 pressure-saturation inversion at the Weyburn Field, Saskatchewan". In: *International Journal of Greenhouse Gas Control* 16, S103–S117.

Mindlin, R. D. (1949). "Compliance of elastic bodies in contact". In: *Journal Applied Mechanics* 16.3, pp. 259–268.

Morgan, E. C., Vanneste, M., Lecomte, I., Baise, L. G., Longva, O., and McAdoo, B. (2012). "Estimation of free gas saturation from seismic reflection surveys by the genetic algorithm inversion of a P-wave attenuation model". In: *Geophysics* 77.4, R175–R187.

Morozov, I. B. and Ma, J. (2009). "Accurate poststack acoustic-impedance inversion by well-log calibration". In: *Geophysics* 74.5, R59–R67.

Mosegaard, K. and Tarantola, A. (1995). "Monte Carlo sampling of solutions to inverse problems". In: *Journal of Geophysical Research: Solid Earth* 100.B7, pp. 12431–12447.

Müller, T. M., Gurevich, B., and Lebedev, M. (2010). "Seismic wave attenuation and dispersion resulting from wave-induced flow in porous rocks—A review". In: *Geophysics* 75.5, 75A147–75A164.

Mulrooney, M. J., Osmond, J. L., Skurtveit, E., Faleide, J. I., and Braathen, A. (2020). "Structural analysis of the Smeaheia fault block, a potential CO2 storage site, northern Horda Platform, North Sea". In: *Marine and Petroleum Geology* 121, p. 104598.

Murphy III, W. F. (1982). "Effects of partial water saturation on attenuation in Massilon sandstone and Vycor porous glass". In: *The Journal of the Acoustical Society of America* 71.6, pp. 1458–1468.

Musgrave, A. W. (1967). *Seismic refraction prospecting*. Society of Exploration Geophysicists.

Nibe, T. and Matsushima, J. (2021). "Monitoring of seismic attenuation change associated with vapor-liquid phase transition using time-lapse reflection seismic data in Kakkonda geothermal field, Japan". In: *Geothermics* 91, p. 102034.

Nocedal, J. (1980). "Updating quasi-Newton matrices with limited storage". In: *Mathematics of computation* 35.151, pp. 773–782.

Nocedal, J. and Wright, S. (2006). *Numerical optimization*. Springer Science & Business Media.

Operto, S., Gholami, Y., Prieux, V., Ribodetti, A., Brossier, R., Metivier, L., and Virieux, J. (2013). "A guided tour of multiparameter full-waveform inversion with multicomponent data: From theory to practice". In: *The leading edge* 32.9, pp. 1040–1054.

Ostrander, W. (1984). "Plane-wave reflection coefficients for gas sands at nonnormal angles of incidence". In: *Geophysics* 49.10, pp. 1637–1648.

Paap, B., Bhakta, T., Vandeweijer, V., and Mannseth, T. (2022). "Modeling Approach for Evaluating Time-Lapse Effects of CO2 Storage on Particle Velocity and Strain Rate Data". In: *EAGE GeoTech 2022 Third EAGE Workshop on Distributed Fibre Optic Sensing*. Vol. 2022. European Association of Geoscientists & Engineers, pp. 1–5.

Pan, W., Innanen, K. A., and Wang, Y. (2020). "SeisElastic2D: An open-source package for multiparameter full-waveform inversion in isotropic-, anisotropic-and viscoelastic media". In: *Computers & Geosciences* 145, p. 104586.

Pan, W. and Wang, Y. (2020). "On the influence of different misfit functions for attenuation estimation in viscoelastic full-waveform inversion: Synthetic study". In: *Geophysical Journal International* 221.2, pp. 1292–1319.

Pang, S. and Stovas, A. (2020). "Frequency-dependent PP and PS reflection coefficients in fractured media". In: *Geophysical Prospecting* 68.3, pp. 926–940.

Peters, L., Anandakrishnan, S., Alley, R., and Voigt, D. (2012). "Seismic attenuation in glacial ice: A proxy for englacial temperature". In: *Journal of Geophysical Research: Earth Surface* 117.F2.

Plessix, R.-E. (2006). "A review of the adjoint-state method for computing the gradient of a functional with geophysical applications". In: *Geophysical Journal International* 167.2, pp. 495–503.

Pride, S. R. (2005). "Relationships between seismic and hydrological properties". In: *Hydrogeophysics*. Springer, pp. 253–290.

Pride, S. R. and Berryman, J. G. (2003a). “Linear dynamics of double-porosity dual-permeability materials. I. Governing equations and acoustic attenuation”. In: *Physical Review E* 68.3, p. 036603.

— (2003b). “Linear dynamics of double-porosity dual-permeability materials. II. Fluid transport equations”. In: *Physical Review E* 68.3, p. 036604.

Pride, S. R., Berryman, J. G., and Harris, J. M. (2004). “Seismic attenuation due to wave-induced flow”. In: *Journal of Geophysical Research: Solid Earth* 109.B1.

Qi, Q., Müller, T. M., and Gurevich, B. (2016). “Saturation scale effect on time-lapse seismic signatures”. In: *Geophysical Prospecting* 64.4-Advances in Rock Physics, pp. 1001–1015.

Quintal, B., Schmalholz, S. M., and Podladchikov, Y. Y. (2009). “Low-frequency reflections from a thin layer with high attenuation caused by interlayer flow”. In: *Geophysics* 74.1, N15–N23.

Quintal, B., Steeb, H., Frehner, M., and Schmalholz, S. M. (2011). “Quasi-static finite element modeling of seismic attenuation and dispersion due to wave-induced fluid flow in poroelastic media”. In: *Journal of Geophysical Research: Solid Earth* 116.B1.

Rabben, T. E. and Ursin, B. (2011). “AVA inversion of the top Utsira Sand reflection at the Sleipner field”. In: *Geophysics* 76.3, pp. C53–C63.

Ravasi, M. and Vasconcelos, I. (2021). “An open-source framework for the implementation of large-scale integral operators with flexible, modern high-performance computing solutions: Enabling 3D Marchenko imaging by least-squares inversion”. In: *Geophysics* 86.5, WC177–WC194.

Ren, H., Goloshubin, G., and Hilterman, F. J. (2009). “Poroelastic analysis of amplitude-versus-frequency variations”. In: *Geophysics* 74.6, N41–N48.

Ribeiro, C. and MacBeth, C. (2006). “Time-lapse seismic inversion for pressure and saturation in Foinaven field, west of Shetland”. In: *first break* 24.10.

Ricker, N. (1953). “Wavelet contraction, wavelet expansion, and the control of seismic resolution”. In: *Geophysics* 18.4, pp. 769–792.

Rimstad, K., Avseth, P., and Omre, H. (2012). “Hierarchical Bayesian lithology/fluid prediction: A North Sea case study”. In: *Geophysics* 77.2, B69–B85.

Romero, J., Luiken, N., and Ravasi, M. (2023). “Seeing through the CO2 plume: joint inversion-segmentation of the Sleipner 4D Seismic Dataset”. In: *arXiv preprint arXiv:2303.11662*.

Sen, M. K. and Stoffa, P. L. (1996). “Bayesian inference, Gibbs’ sampler and uncertainty estimation in geophysical inversion1”. In: *Geophysical Prospecting* 44.2, pp. 313–350.

— (2013). *Global optimization methods in geophysical inversion*. Cambridge University Press.

Sengupta, M., Zhang, H., Zhao, Y., Jervis, M., Grana, and Dario (2021). “Direct depth-domain Bayesian amplitude-variation-with-offset inversion”. In: *Geophysics* 86.5, pp. M167–M176.

Shanno, D. F. (1970). “Conditioning of quasi-Newton methods for function minimization”. In: *Mathematics of computation* 24.111, pp. 647–656.

Shapiro, S. A. and Kaselow, A. (2005). “Porosity and elastic anisotropy of rocks under tectonic stress and pore-pressure changes”. In: *Geophysics* 70.5, N27–N38.

Shaw, R. and Srivastava, S. (2007). "Particle swarm optimization: A new tool to invert geophysical data". In: *Geophysics* 72.2, F75–F83.

Sheehan, A. F., Torre, T. L. de la, Monsalve, G., Abers, G. A., and Hacker, B. R. (2014). "Physical state of Himalayan crust and uppermost mantle: Constraints from seismic attenuation and velocity tomography". In: *Journal of Geophysical Research: Solid Earth* 119.1, pp. 567–580.

Shuey, R. (1985). "A simplification of the Zoeppritz equations". In: *Geophysics* 50.4, pp. 609–614.

Skopintseva, L., Ayzenberg, M., Landrø, M., Nefedkina, T., and Aizenberg, A. M. (2011). "Long-offset AVO inversion of PP reflections from plane interfaces using effective reflection coefficients". In: *Geophysics* 76.6, pp. C65–C79.

Sun, C., Fortin, J., Borgomano, J. V., Wang, S., Tang, G., Bultreys, T., and Cnudde, V. (2022). "Influence of fluid distribution on seismic dispersion and attenuation in partially saturated limestone". In: *Journal of Geophysical Research: Solid Earth* 127.5, e2021JB023867.

Tang, W., Li, J., Zhang, W., Zhang, J., Geng, W., and Li, Y. (2021). "Time-lapse difference inversion based on the modified reflectivity method with differentiable hyper-Laplacian blocky constraint". In: *Geophysics* 86.6, R865–R878.

Tarantola, A. (1987). "Inverse Problem Theory Elsevier". In: *New York*.

Tarantola, A. (2005). *Inverse problem theory and methods for model parameter estimation*. SIAM.

Teng, L., Wang, S., and Cheng, J. (2012). "Probabilistic petrophysical properties estimation integrating viscoelastic AVA inversion with statistical rock physics". In: *2012 SEG Annual Meeting*. OnePetro.

Tisato, N. and Quintal, B. (2013). "Measurements of seismic attenuation and transient fluid pressure in partially saturated Berea sandstone: evidence of fluid flow on the mesoscopic scale". In: *Geophysical Journal International* 195.1, pp. 342–351.

Toms, J., Müller, T., Ciz, R., and Gurevich, B. (2006). "Comparative review of theoretical models for elastic wave attenuation and dispersion in partially saturated rocks". In: *Soil Dynamics and Earthquake Engineering* 26.6-7, pp. 548–565.

Tong, P. (2021). "Adjoint-state traveltime tomography: Eikonal equation-based methods and application to the Anza area in southern California". In: *Journal of Geophysical Research: Solid Earth* 126.5, e2021JB021818.

Trani, M., Arts, R., Leeuwenburgh, O., and Brouwer, J. (2011). "Estimation of changes in saturation and pressure from 4D seismic AVO and time-shift analysis". In: *Geophysics* 76.2, pp. C1–C17.

Tsuneyama, F. and Mavko, G. (2007). "Quantitative detection of fluid distribution using time-lapse seismic". In: *Geophysical prospecting* 55.2, pp. 169–184.

Ursin, B. (1990). "Offset-dependent geometrical spreading in a layered medium". In: *Geophysics* 55.4, pp. 492–496.

Vega, S., Berteussen, K., Sun, Y. F., and Sultan, A. A. (2007). "Is Gassmann the best model for fluid substitution in heterogeneous carbonates?" In: *SEG Technical Program Expanded Abstracts 2007*. Society of Exploration Geophysicists, pp. 1575–1578.

Veire, H. H., Borgos, H. G., and Landrø, M. (2006). "Stochastic inversion of pressure and saturation changes from time-lapse AVO data". In: *Geophysics* 71.5, pp. C81–C92.

Virieux, J. (1986). "P-SV wave propagation in heterogeneous media: Velocity-stress finite-difference method". In: *Geophysics* 51.4, pp. 889–901.

Wandler, A., Evans, B., and Link, C. (2007). "AVO as a fluid indicator: A physical modeling study". In: *Geophysics* 72.1, pp. C9–C17.

Wang, T., Cheng, J., and Geng, J. (2021a). "Reflection Full Waveform Inversion With Second-Order Optimization Using the Adjoint-State Method". In: *Journal of Geophysical Research: Solid Earth* 126.8, e2021JB022135.

Wang, W., McMechan, G. A., and Ma, J. (2021b). "Elastic isotropic and anisotropic full-waveform inversions using automatic differentiation for gradient calculations in a framework of recurrent neural networks". In: *Geophysics* 86.6, R795–R810.

Wang, Y. (2019). "A constant-Q model for general viscoelastic media". In: *Geophysical Journal International* 219.3, pp. 1562–1567.

Waters, K. H. and Waters, K. H. (1981). *Reflection seismology: A tool for energy resource exploration*. Wiley New York.

Weinzierl, W. and Wiese, B. (2021). "Deep learning a poroelastic rock-physics model for pressure and saturation discriminationDeep learning a rock-physics model". In: *Geophysics* 86.1, MR53–MR66.

White, J. E., Mihailova, N., and Lyakhovitsky, F. (1975). "Low-frequency seismic waves in fluid-saturated layered rocks". In: *The Journal of the Acoustical Society of America* 57.S1, S30–S30.

White, J. (1975). "Computed seismic speeds and attenuation in rocks with partial gas saturation". In: *Geophysics* 40.2, pp. 224–232.

Winkler, K. W. (1985). "Dispersion analysis of velocity and attenuation in Berea sandstone". In: *Journal of Geophysical Research: Solid Earth* 90.B8, pp. 6793–6800.

Wollner, U. and Dvorkin, J. (2018). "Effective bulk modulus of the pore fluid at patchy saturation". In: *Geophysical Prospecting* 66.7, pp. 1372–1383.

Wong, M. Y., JafarGandomi, A., MacBeth, C., Bertrand, A., and Hoeber, H. (2015). "Pressure and saturation change inversion using 4D seismic: Application to a chalk reservoir in North Sea". In: *2015 SEG Annual Meeting*. OnePetro.

Xiao, S., Ba, J., Guo, Q., Carcione, J., Zhang, L., and Luo, C. (2020). "Seismic pre-stack AVA inversion scheme based on lithology constraints". In: *Journal of Geophysics and Engineering* 17.3, pp. 411–428.

Yam, H. and Schmitt, D. R. (2011). "CO2 rock physics: a laboratory study". In: *Insite Magazine* 30, pp. 13–16.

Yang, J., Geng, J., and Zhao, L. (2020). "A frequency-decomposed nonstationary convolutional model for amplitude-versus-angle-and-frequency forward waveform modeling in attenuative media". In: *Geophysics* 85.6, T301–T314.

Yong, P., Brossier, R., and Métivier, L. (2022). "Parsimonious truncated Newton method for time-domain full-waveform inversion based on the Fourier-domain full-scattered-field approximation". In: *Geophysics* 87.1, R123–R146.

Zhao, H., Gao, J., and Liu, F. (2014a). "Frequency-dependent reflection coefficients in diffusive-viscous media". In: *Geophysics* 79.3, T143–T155.

Zhao, L., Geng, J., Cheng, J., Han, D.-h., and Guo, T. (2014b). "Probabilistic lithofacies prediction from prestack seismic data in a heterogeneous carbonate reservoirProbabilistic lithofacies prediction". In: *Geophysics* 79.5, pp. M25–M34.

Zhao, L., Yao, Q., Han, D.-h., Zhou, R., Geng, J., and Li, H. (2017). "Frequency-and angle-dependent poroelastic seismic analysis for highly attenuating reservoirs". In: *Geophysical Prospecting* 65.6, pp. 1630–1648.

Zheglova, P. and Malcolm, A. (2019). "Vector acoustic full waveform inversion: taking advantage of de-aliasing and receiver ghosts". In: *arXiv preprint arXiv:1910.05427*.

Zhou, T., Meng, L., Xie, Y., and Han, J. (2019). "An adjoint-state full-waveform tsunami source inversion method and its application to the 2014 Chile-Iquique tsunami event". In: *Journal of Geophysical Research: Solid Earth* 124.7, pp. 6737–6750.

Zhu, W., Xu, K., Darve, E., and Beroza, G. C. (2021). "A general approach to seismic inversion with automatic differentiation". In: *Computers & Geosciences* 151, p. 104751.

Zoback, M. D. (2010). *Reservoir geomechanics*. Cambridge university press.

Zoeppritz, K. (1919). "VIIb. Über Reflexion und Durchgang seismischer Wellen durch Unstetigkeitsfl". In: *Göttinger Nachrichten* I, pp. 66–84.

Zong, Z., Yin, X., and Wu, G. (2015). "Complex seismic amplitude inversion for P-wave and S-wave quality factors". In: *Geophysical Journal International* 202.1, pp. 564–577.

Appendix A

A.1 Gradient computation and efficiency tests

Seismic AVO inverse theory to predict the elastic and viscoelastic medium properties and reservoir dynamic changes is based on the gradient descent method which iteratively computes the subsequent point using first-order gradient at the current location, multiplies it by step length and subtracts from the current location value. Therefore, in gradient-based optimizations, it is significantly important to calculate the accurate gradient of the objective function with respect to the model variables of our interest. In addition, the computation cost of the inversion technique is greatly dependent on the method's efficiency in computing the gradient. To derive the gradients of the differentiable objective function with respect to unknown model properties, we implement the adjoint-state method (provides analytical gradient solution), and to verify the accuracy of the adjoint-based gradients (AS), the adjoint gradients are cross-checked by comparing with the gradients calculated using the finite difference (FD) approximation. The computation cost of both methods is also compared. The equation for finite difference approximations (central difference) e.g., the partial derivative of a function f at a point x is given below:

$$\frac{\partial f}{\partial x} = \frac{f(x+\Delta x) - f(x-\Delta x)}{2\Delta x} \tag{A.1}$$

Figure A.1 shows the gradient plots of the objective function (J) (defined in Chapter 2) with respect to P and S wave velocities and density. These gradients are computed by using both the adjoint-state and the finite difference methods. The gradient equations for V_P, V_S, and ρ in the elastic media are described in Chapter 2 (equations 2.6 - 2.8). The data used for the gradient comparison is the same as given in Chapter 2 - example 1. The cross-check of the adjoint-state-based gradient with the finite difference method describes that the gradient solution is accurate. Figure A.2 shows the gradients of the objective function with respect to model variables in an-elastic media. The gradients of seismic velocities, density, and P and S wave quality factors computed by the adjoint method are in close agreement with the finite difference method. The gradient equations for V_P, V_S, ρ, Q_P and Q_S in viscoelastic medium are described in Chapter 4 (equations 4.28 - 4.32). The data used in this illustration (Figure A.2) is taken from example 1 of Chapter 4.

Similarly, in Figure A.3 and A.4, the accuracy of gradients of the objective function (J) (defined in Chapters 3 and 5) with respect to water saturation and effective pressure (calculated from the rock physics models for elastic and viscoelastic mediums respectively) by using the adjoint method are tested by making a comparison with the finite difference method. The data described in example 1 of Chapter 3 is used to derive and calculate these gradients. The saturation-pressure gradients used in the inversion methods match very well with FD approximations. The saturation and pressure gradient equations in the elastic case are described in Chapter 3 (equations 3.21 - 3.22) while for the viscoelastic case, the gradient equations are given in Chapter 5 (equations 5.18 - 5.19).

In the next, a computational cost comparison between both the adjoint-state solution and the finite difference approximation has been made in Figure A.5. Figure A.5 (panel a) shows the time (sec.) taken by both AS and FD methods to compute the gradients

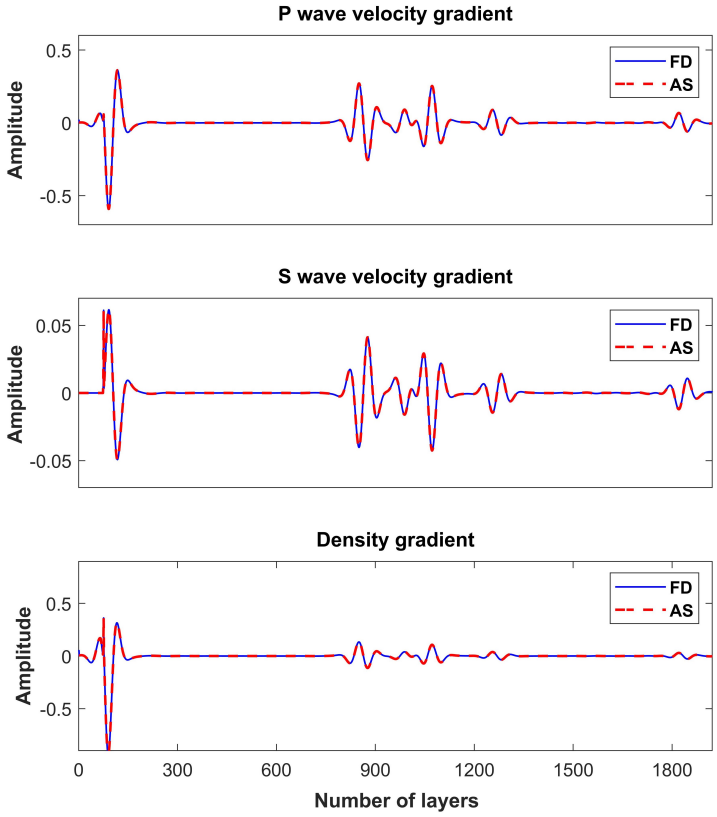

Figure A.1: The comparison between gradients of P and S wave velocities and density computed by using analytical gradient solution (AS) and the finite difference (FD) approximation. These adjoint-state gradients are used for the inversion of seismic velocities and density in chapter 2.

of P and S wave velocities and density for 1922 layers (given in Figure A.1). It can easily be inferred that the computation cost in the case of the adjoint-state method is far less (0.04 sec.) as compared to the finite difference method which is around 439.4 sec. Figure A.5 (panel b) compares the cost of the gradients (described in Figure A.2) of seismic velocities, Q-factors, and density in the viscoelastic case. FD method requires 4556 sec. to calculate the gradients of five model properties each having 260 layers in comparison to AS which only needs 1.62 sec. Figure A.5 (panels c and d) illustrates the gradient computing time of both the analytical and the finite difference approximation for 115 layers of each water saturation and effective pressure variables (given by Figure A.3 and A.4). Again the computation costs of the adjoint-state method to calculate the gradient of S_w and P_e are very small as compared to the FD method. This discussion shows the effectiveness of the adjoint-state method to compute the gradients of the objective function with respect to model properties over the other method e.g., the finite

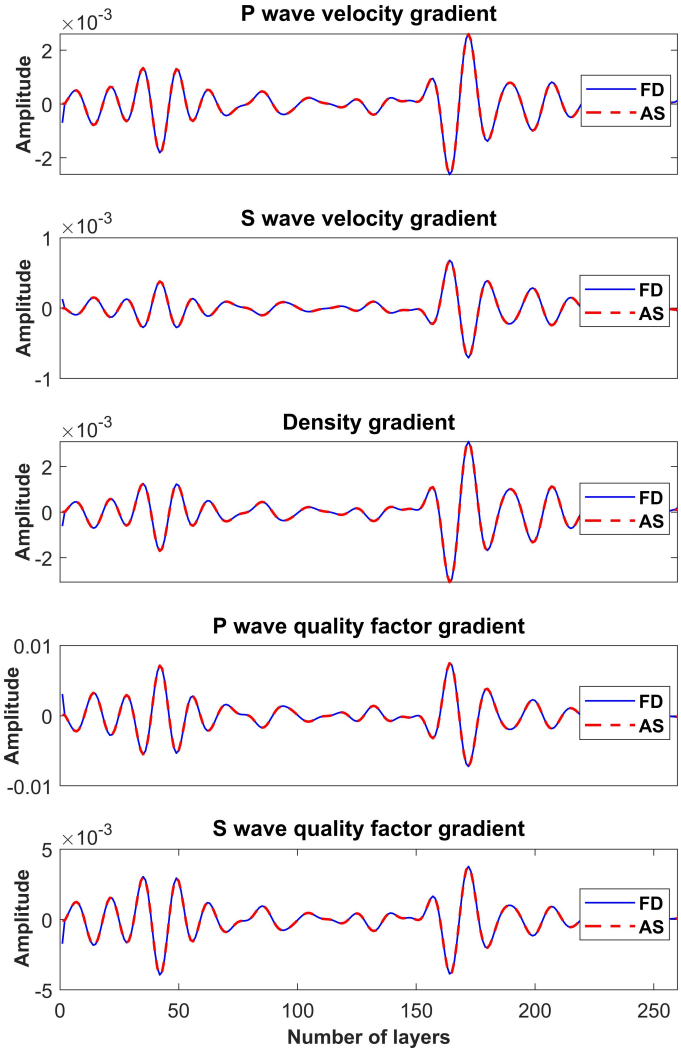

Figure A.2: The comparison between the gradients of P and S wave velocities, density, and seismic quality factors computed by using the analytical gradient solution (AS) and the finite difference (FD) approximation. The adjoint-state gradients are used for the inversion of seismic velocities, density, and quality factors in chapter 4.

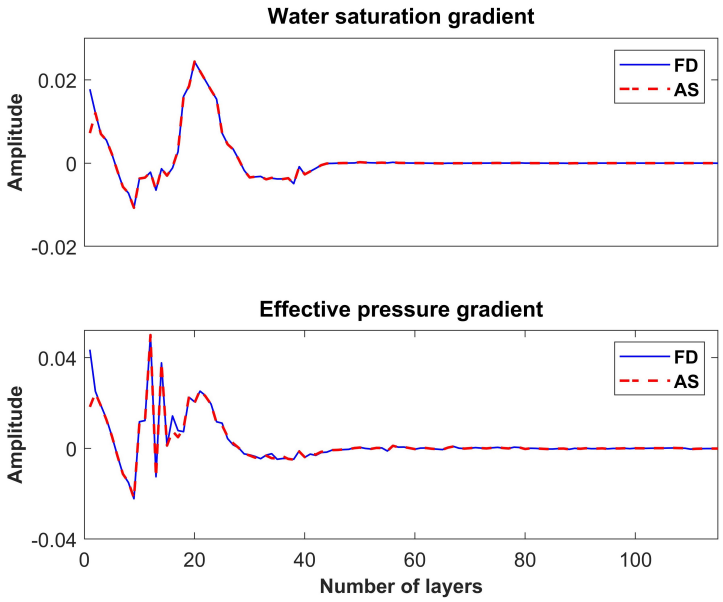

Figure A.3: The comparison between gradients of water saturation and effective pressure computed by using the analytical gradient solution (AS) and the finite difference (FD) approximation.

difference approximation. It not only reduces the computational cost of the inversion method but also provides a more accurate gradient solution. The small differences in the AS and FD gradients plotted here (from Figure A.1 - A.4) can be observed at a smaller scale by zooming in on the figures.

A.2 Convergence rates for the gradient-descent method

In this section, the convergence of the objective function to the minima for the gradient-descent method is described by plotting the error function against the number of iterations. This is applied to all the objective functions used in this dissertation to retrieve the seismic and reservoir dynamic properties in the elastic and frequency-dependent inversion methods. The convergence tests show that the optimization method provides a very good convergence for almost all the model variables when the signal-to-noise ratio is ∞. However, it is noted that the error function is strongly affected by the signal-to-noise ratio and many other factors like scaling, regularization weights, background models, etc. which are very commonly applied in seismic inversion methods. The convergence to minima tests demonstrates that the values of the error function increase with the increase in signal-to-ratio.

In Figure A.6, the error function for the objective function (defined in Chapter 2) to predict the elastic properties (V_P, V_S, and ρ) is plotted for both with and without noise cases. The error function is reduced up to 0 for the noise-free case and also close to zero

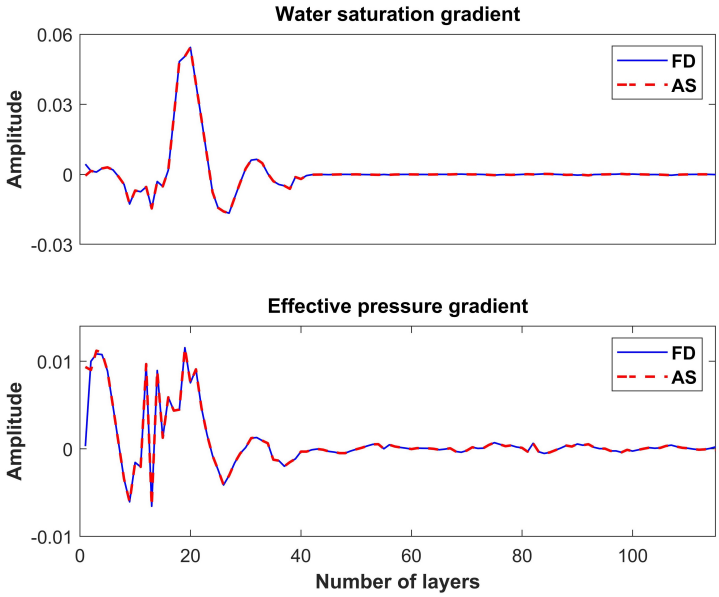

Figure A.4: The comparison between gradients of water saturation and effective pressure computed by using the analytical gradient solution (AS) and the finite difference (FD) approximation.

when the S/N ratio is 50. The convergence of the objective function is very good in the case of elastic properties. Figure A.7 shows the convergence of the objective function by using FAVO inversion to predict (panel a) V_P, V_S and ρ and (panel b) both quality factors (Q_P and Q_S) for the noisy and noise-free data. The convergence in the case of noisy data is affected by the regularization weights and scaling applied to the model variables. Despite a very high error function (lower convergence), the optimization method predicts very good estimation of V_P, V_S, and ρ even when S/N = 50 as shown in Figure 6 (Chapter 4). However, the seismic noise affects the sensitivity of Q-factors to the seismic data therefore it becomes hard to get good convergence for the seismic quality factors. This issue is well described in Chapter 4. Figure A.8 illustrates the error functions to obtain the optimal solution for the water saturation and the effective pressure by using the elastic AVO inversion (panel a) and the FAVO inversion (panel b). The convergence rate is very good in the case of S/N = ∞ while in the case of a high signal-to-noise ratio (e.g., S/N = 5 and S/N = 15), the error function is reduced slightly but enough to get very good results of the inverted models of the water saturation and the effective pressure as described in Chapter 3 and Chapter 5. In the noise-free case, the objective function is minimized up to 90 % and 80 % for the elastic AVO and viscoelastic FAVO inversion methods respectively.

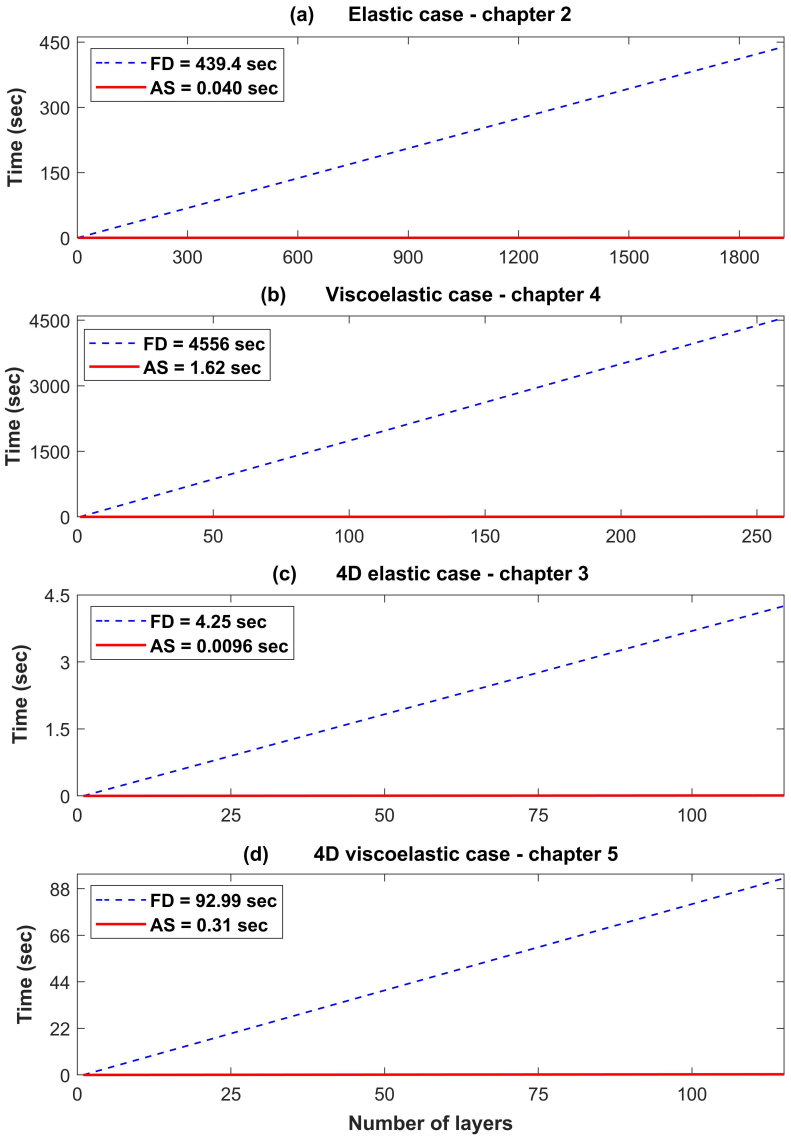

Figure A.5: The computational cost comparison between gradients of the model variables derived by the analytical gradient solution (AS) and the finite difference (FD) approximation. Panel (a) describes the computational cost for P and S wave velocities and density in the elastic medium, and panel (b) shows the time taken by FD and AS methods to compute the gradients of the objective function with respect to seismic velocities and corresponding Q-factors and density in the viscoelastic medium, panels (c and d) represent the calculation time for the water saturation and pressure gradients in the elastic and an-elastic cases respectively.

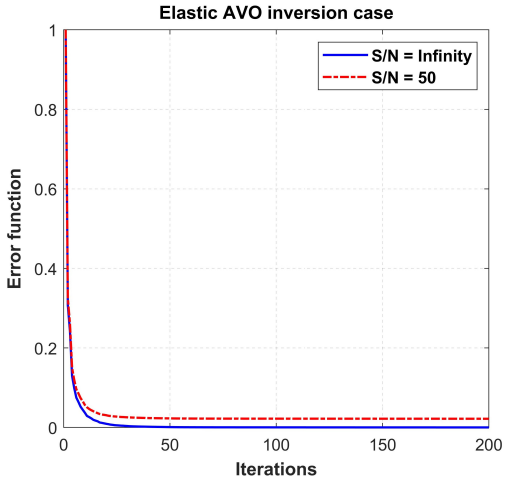

Figure A.6: The error function versus the number of iterations taken by the optimization method to minimize the objective function.

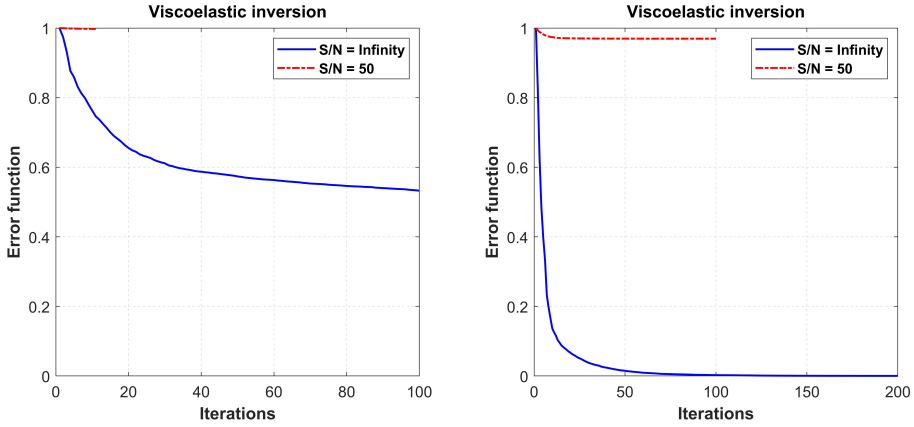

Figure A.7: The error function versus the number of iterations taken by the optimization method to minimize the objective function defined for the FAVO inversion. Panel (a) shows the error function for V_P, V_S and ρ while panel (b) is for Q_P and Q_S.

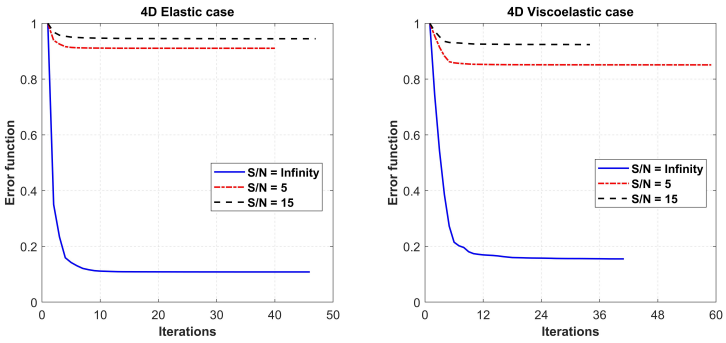

Figure A.8: The error function versus the number of iterations used to minimize the objective function defined to obtain the optimal solution for water saturation and effective pressure in (a) elastic and (b) viscoelastic media.